ISSN: 2220-9506 (Print)
ISSN: 2414-0473 (Online)

ПРИБОРЫ И МЕТОДЫ ИЗМЕРЕНИЙ

DEVICES AND METHODS OF MEASUREMENTS

Том 13 № 1 Vol. 13

2022

ПРИБОРЫ И МЕТОДЫ ИЗМЕРЕНИЙ

Научно-технический журнал
Основан в 2010 г.
Учредитель
Белорусский национальный технический университет
Выходит 4 раза в год
Журнал включен в базы данных:
Web of Science Core Collection (ESCI),
EBSCO, DOAJ, WorldCat, OpenAIRE, Google Scholar, РИНЦ,
ЭБС «Лань», НЭБ «КиберЛенинка», Соционет

Том 13 **№ 1** **2022**

ГЛАВНЫЙ РЕДАКТОР

Гусев О.К., *д.т.н., профессор, проректор Белорусского национального технического университета (г. Минск, Беларусь)*

ЗАМЕСТИТЕЛЬ ГЛАВНОГО РЕДАКТОРА

Маляревич А.М., *член-корреспондент НАН Беларуси, д.ф.-м.н., профессор, проректор Белорусского национального технического университета (г. Минск, Беларусь)*

РЕДАКЦИОННАЯ КОЛЛЕГИЯ

Алексеев В.А., *д.т.н., профессор, профессор кафедры «Физика и оптотехника» Ижевского государственного технического университета имени М.Т. Калашникова (г. Ижевск, Россия)*

Анищик В.М., *д.ф.-м.н., профессор, профессор кафедры физики твёрдого тела Белорусского государственного университета (г. Минск, Беларусь)*

Бубулис А., *д.т.н., профессор, главный научный сотрудник Научного центра мехатроники Каунасского технологического университета (г. Каунас, Литва)*

Вайн А.А., *д.т.н., профессор Тартуского университета (г. Тарту, Эстония)*

Виба Я., *д.т.н., профессор, директор Института механики Рижского технического университета (г. Рига, Латвия)*

Гуттен М., *д.т.н., заведующий кафедрой метрологии и прикладной электротехники Жилинского университета (г. Жилина, Словакия)*

Дмитриев С.М., *д.т.н., профессор, ректор Нижегородского государственного технического университета имени Р.Е. Алексеева (г. Нижний Новгород, Россия)*

Дэнилак С., *профессор Производственно-исследовательского центра Технологического института штата Джорджия (г. Атланта, США)*

Жарин А.Л., *д.т.н., профессор, профессор кафедры «Информационно-измерительная техника и технологии» Белорусского национального технического университета (г. Минск, Беларусь)*

Жуковский П., *д.т.н., профессор, заведующий кафедрой электрических аппаратов и техники высоких напряжений Люблинского технического университета (г. Люблин, Польша)*

Колтунович Т.Н., *д.т.н., профессор, Люблинский технический университет (г. Люблин, Польша)*

Комаров Ф.Ф., *академик НАН Беларуси, д.ф.-м.н., профессор, заведующий лабораторией элионики Института прикладных физических проблем имени А.Н. Севченко Белорусского государственного университета (г. Минск, Беларусь)*

Кулешов Н.В., *член-корреспондент НАН Беларуси, д.ф.-м.н., профессор, заведующий кафедрой «Лазерная техника и технология» Белорусского национального технического университета (г. Минск, Беларусь)*

Кучинский П.В., *д.ф.-м.н., доцент, директор Института прикладных физических проблем имени А.Н. Севченко Белорусского государственного университета (г. Минск, Беларусь)*

Кэмп А., *профессор Института фотоники Страсклайдского университета (г. Глазго, Великобритания)*

Матеос Х., *к.ф.-м.н., доцент, университет Ровира и Вирхилий (г. Таррагона, Испания)*

Пилипенко В.А., *член-корреспондент НАН Беларуси, д.т.н., профессор, заместитель директора ГЦ «Белмикроанализ» ОАО «ИНТЕГРАЛ» – управляющая компания холдинга «ИНТЕГРАЛ» (г. Минск, Беларусь)*

Плескачевский Ю.М., *член-корреспондент НАН Беларуси, д.т.н., профессор (г. Минск, Беларусь)*

Погребняк А.Д., *д.ф.-м.н., профессор, заведующий кафедрой наноэлектроники Сумского государственного университета (г. Сумы, Украина)*

Распопов В.Я., *д.т.н., профессор, заведующий кафедрой «Приборы управления» Тульского государственного университета (г. Тула, Россия)*

Тимчик Г.С., *д.т.н., профессор, декан приборостроительного факультета, Национальный технический университет Украины «Киевский политехнический институт имени Игоря Сикорского» (г. Киев, Украина)*

Це Ли, *заместитель директора Северо-Восточного НИИ техники датчиков (г. Харбин, КНР)*

Чижик С.А., *академик НАН Беларуси, д.т.н., профессор, Первый заместитель Председателя Президиума НАН Беларуси, заведующий кафедрой «Микро- и нанотехника» Белорусского национального технического университета (г. Минск, Беларусь)*

Шкадаревич А.П., *академик НАН Беларуси, д.ф.-м.н., профессор, директор НТЦ «ЛЭМТ» Белорусского оптико-механического объединения (г. Минск, Беларусь)*

Юмашев К.В., *д.ф.-м.н., профессор, заведующий кафедрой «Экспериментальная и теоретическая физика» Белорусского национального технического университета (г. Минск, Беларусь) юб*

Издание зарегистрировано в Министерстве информации Республики Беларусь 25 июня 2010 г.
Регистрационный номер 1372
В соответствии с решением ВАК от 8 июля 2011 г. №13/1 журнал включен в Перечень научных изданий для опубликования результатов диссертационных исследований; научное направление: «Средства и методы измерений, контроля, диагностики и оценки качества объектов и процессов» (технические и физико-математические науки)
ISSN 2220-9506

Подписка осуществляется через почтовые отделения связи по «Каталогу газет и журналов Республики Беларусь».
Подписные индексы – 74835; 748352.

Ответственный секретарь редакции: Шахлевич Л.Н.
Редактор: Чабарова О.Л.
Набор и верстка выполнены в редакции журнала «Приборы и методы измерений».
Подписано в печать 28.03.2022. Формат бумаги 60×84 1/8. Бумага мелованная.
Гарнитура Times New Roman. Печать цифровая. Усл. печ. л. 8,84. Уч.-изд. л. 3,45. Тираж 100 экз.
Дата выхода в свет 06.04.2022. Заказ № 189.
Отпечатано в Белорусском национальном техническом университете. ЛП № 02330/74 от 03.03.2014. Пр-т Независимости, 65, 220013, г. Минск

АДРЕС РЕДАКЦИИ:
Белорусский национальный технический университет
пр-т Независимости, 65, 220013, г. Минск, Республика Беларусь,
тел.: +375 (17) 293 96 67, факс: +375 (17) 292 67 94
e-mail: pimi@bntu.by
http://pimi.bntu.by

© «Приборы и методы измерений», 2022

DEVICES AND METHODS OF MEASUREMENTS

Scientific and Engineering Journal

Founded in 2010

Founder
Belarusian National Technical University

Issued four times a year

The Journal is included in the following databases:
Web of Science Core Collection (ESCI),
EBSCO, DOAJ, WorldCat, OpenAIRE, Google Scholar,
RISC, Lan, CyberLeninka, Socionet

Volume 13 **№ 1** **2022**

EDITOR-IN-CHIEF

Oleg K. Gusev, *Doctor of Science (Engineering), Professor, Vice-Rector of Belarusian National Technical University (Minsk, Belarus)*

DEPUTY EDITOR-IN-CHIEF

Aliaksandr M. Malyarevich, *Corresponding Member of the National Academy of Sciences of Belarus, Doctor of Science (Physics and Mathematics), Professor, Vice-Rector of Belarusian National Technical University (Minsk, Belarus)*

EDITORIAL BOARD

Vladimir A. Alekseev, *Doctor of Science (Engineering), Professor, Department of Physics and Optical Engineering, Kalashnikov Izhevsk State Technical University (Izhevsk, Russia)*

Victor M. Anishchik, *Doctor of Science (Physics and Mathematics), Professor, Department of Solid State Physics, Belarusian State University (Minsk, Belarus)*

Algimantas Bubulis, *Doctor of Science (Engineering), Professor, Kaunas University of Technology (Kaunas, Lithuania)*

Arvid A. Vain, *Doctor of Science (Engineering), Professor, University of Tartu (Tartu, Estonia)*

Janis Viba, *Doctor of Science (Engineering), Professor, Director of Institute of Mechanics, Riga Technical University (Riga, Latvia)*

Miroslav Gutten, *Doctor of Science (Engineering), Head of Department of Metrology and Applied Electrical Engineering, University of Žilina (Žilina, Slovakia)*

Sergei M. Dmitriev, *Doctor of Science (Engineering), Professor, Rector of R.E. Alekseev Nizhny Novgorod State Technical University (Nizhny Novgorod, Russia)*

Steven Danyluk, *PhD, Professor, Production and Research Center, Georgia Institute of Technology (Atlanta, USA)*

Anatoly L. Zharin, *Doctor of Science (Engineering), Professor, Information and Measuring Technologies Department, Belarusian National Technical University (Minsk, Belarus)*

Pawel Żukowski, *Doctor of Science (Engineering), Professor, Head of Department of Electrical Devices and High Voltages Technology, Lublin University of Technology (Lublin, Poland)*

Tomasz N. Koltunowicz, *Doctor of Science (Engineering), Professor, Lublin University of Technology (Lublin, Poland)*

Fadey F. Komarov, *Academician of the National Academy of Sciences of Belarus, Doctor of Science (Physics and Mathematics), Professor, Head of the Elionics Laboratory, A.N. Sevchenko Institute of Applied Physical Problems, Belarusian State University (Minsk, Belarus)*

Nikolay V. Kuleshov, *Corresponding Member of the National Academy of Sciences of Belarus, Doctor of Science (Physics and Mathematics), Professor, Head of Laser Equipment and Technology Department, Belarusian National Technical University (Minsk, Belarus)*

Petr V. Kuchynski, *Doctor of Science (Physics and Mathematics), Director of A.N. Sevchenko Institute of Applied Physical Problems, Belarusian State University (Minsk, Belarus)*

Alan Kemp, *PhD, Professor, Institute of Photonics, University of Strathclyde (Glasgow, United Kingdom)*

Xavier Mateos, *PhD, Associate Professor, Rovira i Virgili University (Tarragona, Spain)*

Vladimir A. Pilipenko, *Corresponding Member of the National Academy of Sciences of Belarus, Doctor of Science (Engineering), Professor, Deputy Director of the State Center “Belmicroanalysis” of JSC “INTEGRAL” – “INTEGRAL” Holding Managing Company (Minsk, Belarus)*

Yuriy M. Pleskachevsky, *Corresponding Member of the National Academy of Sciences of Belarus, Doctor of Science (Engineering), Professor (Minsk, Belarus)*

Alexander D. Pogrebnjak, *Doctor of Science (Physics and Mathematics), Professor, Head of Department of Nanoelectronic, Sumy State University (Sumy, Ukraine)*

Vladimir Ya. Raspopov, *Doctor of Science (Engineering), Professor, Head of Control Devices Department, Tula State University (Tula, Russia)*

Gryhoriy S. Tymchyk, *Doctor of Science (Engineering), Professor, Dean of the Faculty of Instrumentation Engineering, National Technical University of Ukraine “Igor Sikorsky Kyiv Polytechnic Institute” (Kyiv, Ukraine)*

Tse Li, *Deputy Director of Northeast Scientific Research Institute of Sensor Technology (Harbin, China)*

Sergei A. Chizhik, *Academician of the National Academy of Sciences of Belarus, Professor, Doctor of Science (Engineering), the First Vice Chairman of the Presidium of the National Academy of Sciences of Belarus, Head of Micro- and Nanotechnics Department, Belarusian National Technical University (Minsk, Belarus)*

Alexey P. Shkadarevich, *Academician of the National Academy of Sciences of Belarus, Doctor of Science (Physics and Mathematics), Professor, Director of the Scientific and Technical Center “LEMT” of the BelOMO (Minsk, Belarus)*

Konstantin V. Yumashev, *Doctor of Science (Physics and Mathematics), Professor, Head of Experimental and Theoretical Physics Department, Belarusian National Technical University (Minsk, Belarus)*

ADDRESS:
Belarusian National Technical University
Nezavisimosty Ave., 65, Minsk 220013, Belarus
Tel.: +375 (17) 293 96 67, fax: +375 (17) 292 67 94
e-mail: pimi@bntu.by
http://pimi.bntu.by

© «Devices and Methods of Measurements», 2022

СОДЕРЖАНИЕ

Средства измерений

Методы измерений, контроля, диагностики

CONTENTS

Measuring Instruments

Methods of Measurements, Monitoring, Diagnostics

Devices and Methods for Measuring of the Ambient Air Dust. Short Review

N.I. Mukhurov[1], A.A. Khodin[1], Y.-J. Kim[2]

[1]*State Research and Production Association*
“*Optics, Optoelectronics and Laser Technology*”,
Nezavisimosty Ave., 68, Minsk 220072, Republic of Belarus

[2]*Yonsei University, School of Mechanical Engineering, Seoul 03722, Republic of Korea*

Received 28.01.2022
Accepted for publication 10.03.2022

Abstract

The main characteristics of airborne micro/nanoparticles, their impact on human health and air quality standards are presented. International standards classify microparticles by size (PM10, PM2.5, PM1, UFP), establish maximum allowable concentrations and control methods. Particular attention is paid to carbon- and virus-containing microparticles control. To monitor the air environment in enclosed spaces and in transport, the portable sensors of micro-, nanoparticles are required with the ability to classify them by size and electrophysical characteristics.

Detection of microparticles includes the sorting of particles entering the sensor by size and material type, subsequent actual detection of particles of the same kind, with subsequent classification by size, electrical and morphological characteristics. Separation of nano- and microparticles by size before detection improves the sensitivity and selectivity of the detector both in size and material. The virtual impactor and dielectrophoresis method are considered for integration in a Lab-on-Chip type sensor. Detection of microparticles is performed by separating the dispersed phase from the aerosol followed by the analysis, or directly in the air flow. The classification of detection methods according to speed and functionality is given. Among the methods allowing detection of micrometer and submicrometer size particles, the most suitable for miniaturization and serial production of Lab-on-Chip sensors are the multi-wavelength photoelectric, MEMS, and capacitor elements.

The microelectromechanics, microfluidics and microoptics technologies make it possible to create portable sensor systems of the Lab-on-Chip type to detect particulates matter of micrometer and submicrometer size. A micro-, nanoparticles detector prototype based on alumina technology using MEMS elements for a compact Lab-on-Chip type sensor is presented. The proposed design for multifunctional portable detector of airborne micro/nanoparticles is prospective for industry, transport, medicine, public and residential buildings applications.

Keywords: microparticles, detector, Lab-on-Chip, alumina technology, prototype.

DOI: 10.21122/2220-9506-2022-13-1-7-16

Адрес для переписки:
Ходин А.А.
ГНПО «Оптика, оптоэлектроника и лазерная техника»,
пр-т Независимости, 68,
г. Минск 220072, Беларусь,
e-mail: aahodin@gmail.com

Address for correspondence:
Khodin A.A.
State Scientific and Production Association
“*Optics, Optoelectronics and Laser Technology*”,
Nezavisimosty Ave., 68, Minsk 220072, Belarus
e-mail: aahodin@gmail.com

Для цитирования:
N.I. Mukhurov, A.A. Khodin, Y.-J. Kim.
Devices and Methods for Measuring of the Ambient Air Dust.
Short Review.
Приборы и методы измерений.
2022. – Т. 13, № 1. – С. 7–16.
DOI: 10.21122/2220-9506-2022-13-1-7-16

For citation:
N.I. Mukhurov, A.A. Khodin, Y.-J. Kim.
Devices and Methods for Measuring of the Ambient Air Dust.
Short Review.
Devices and Methods of Measurements.
2022, vol. 13, no. 1, pp. 7–16.
DOI: 10.21122/2220-9506-2022-13-1-7-16

Приборы и методы измерений запылённости окружающей воздушной среды. Краткий обзор

Н.И. Мухуров[1], **А.А. Ходин**[1], **Ёнг Чжун Ким**[2]

[1]ГНПО «Оптика, оптоэлектроника и лазерная техника»,
пр-т Независимости, 68, г. Минск 220072, Беларусь
[2]Университет Ёнсе, Колледж инженерии, Сеул 03722, Республика Корея

Поступила 28.01.2022
Принята к печати 10.03.2022

Представлены основные характеристики переносимых воздухом микро/наночастиц, их влияние на здоровье человека и нормативы качества воздушной среды. Международные стандарты классифицируют микрочастицы по размеру (PM10, PM2,5, PM1, UFP), определяют предельно допустимые концентрации и методики их контроля. Особое внимание уделяется контролю углерод- и вирус-содержащих микрочастиц. Для мониторинга воздушной среды в закрытых помещениях, в транспорте требуются портативные датчики микро-, наночастиц с возможностями их классификации по размеру и электрофизическим характеристикам.

Детектирование микрочастиц включает сортировку попадающих в детектор микро/наночастиц по размеру и типу материала и собственно детектирование однотипных частиц с последующей классификацией по размеру, электрофизическим и морфологическим характеристикам. Разделение нано- и микрочастиц по размеру перед детектированием повышает чувствительность и селективность детектора как по размерам, так и по материалу. Для интеграции в сенсоре *Lab-on-Chip* типа рассмотрены методы виртуального импактора и диэлектрофореза. Детектирование микрочастиц осуществляется с выделением дисперсной фазы из аэрозоля с последующим анализом либо непосредственно в воздушном потоке. Приведена классификация методов детектирования по быстродействию и функциональным возможностям. Среди методов детектирования частиц микронных и субмикронных размеров наиболее пригодны для миниатюризации и серийного изготовления Lab-on-Chip сенсоров мультиволновые фотоэлектрические, МЭМС, конденсаторные элементы.

Технологии микроэлектромеханики, микрофлюидики и микрооптики позволяют создавать портативные сенсорные системы типа *Lab-on-Chip* для детектирования твёрдых частиц микронного и субмикронного размера. Представлен прототип детектора микро-, наночастиц на основе алюмооксидной технологии с использованием МЭМС элементов для компактного сенсора *Lab-on-Chip* типа. Предлагаемая конструкция многофункционального портативного детектора микро/наночастиц воздушной (газовой) среды перспективна для применения в промышленности, транспорте, медицине, общественных и жилых помещениях.

Ключевые слова: микрочастицы, детектор, лаборатория на чипе, алюмооксидная технология, прототип.

DOI: 10.21122/2220-9506-2022-13-1-7-16

Адрес для переписки:
Ходин А.А.
ГНПО «Оптика, оптоэлектроника и лазерная техника»,
пр-т Независимости, 68,
г. Минск 220072, Беларусь,
e-mail: aahodin@gmail.com

Address for correspondence:
Khodin A.A.
State Scientific and Production Association
“Optics, Optoelectronics and Laser Technology”,
Nezavisimosty Ave., 68, Minsk 220072, Belarus
e-mail: aahodin@gmail.com

Для цитирования:
N.I. Mukhurov, A.A. Khodin, Y.-J. Kim.
Devices and Methods for Measuring of the Ambient Air Dust.
Short Review.
Приборы и методы измерений.
2022. – Т. 13, № 1. – С. 7–16.
DOI: 10.21122/2220-9506-2022-13-1-7-16

For citation:
N.I. Mukhurov, A.A. Khodin, Y.-J. Kim.
Devices and Methods for Measuring of the Ambient Air Dust.
Short Review.
Devices and Methods of Measurements.
2022, vol. 13, no. 1, pp. 7–16.
DOI: 10.21122/2220-9506-2022-13-1-7-16

Introduction

The improvement of technologies and methods to control harmful emissions into the atmosphere has not yet led to a global reduction in the total mass of emissions of the substances, primarily aerosols – the air-dispersed systems of microparticles in the form of dust, smoke, fog. The most common hazards are industrial dust of various nature and natural sources – dust storms, volcanic eruptions, etc. Microparticles in air environment disrupt functioning of equipment, deteriorate products quality, cause occupational acute and chronic diseases of respiratory system, circulatory system, eyes, and skin [1]. When penetrating deep into the lungs, they can deliver toxins, bacteria and viruses into the body.

Airborne particulate matter (PM) varies greatly in chemical composition, morphology and size. A number of international rules and standards for PM control have been developed that define the maximum allowable concentration of solid PM and methods to control them. The International Organization for Standardization ISO distinguishes several fractions of PM by size – PM10, PM2.5, PM1, Ultrafine particles [2]. In particular, PM10 is defined as "solid particles passing through an inlet of a specified size with an efficiency of 50 % at an aero-dynamic diameter of 10 μm" [3]. Ultrafine particles smaller than 0.1 μm are referred to as PM0.1.

Permissible levels of airborne microparticles of the PM10, PM2.5 classes are standardized by the World Health Organization [4], European Union [5], US Environmental Protection Agency [6], Ministry of Environmental Protection of the PRC [7] and sanitary regulations of the Russian Federation[1]. Special attention is paid to airborne micro-, nanoparticles of carbon in the form of black carbon [8], brown carbon [9] and soot (carbon black), the aggregates of which do not break down in the lungs into smaller or primary particles of ~ 10 nm size [10].

It is also important to control specifically the airborne viruses and bacteria of 20–500 nm size [11, 12]. Pathogenic viruses are viable in air, forming complexes with other microparticles [13] and drifting for a long time at a low sedimentation rate – from 3.1×10^{-3} m·s^{-1} for particles 10 μm in size to 3.5×10^{-5} m·s^{-1} for ~ 1 μm size particles [14]. In particular, it has been established that SARS-CoV-2 viruses remain suspended in enclosed spaces for a long time [15].

Thus, the control of atmospheric air dust content is an urgent production, hygiene and engineering problem. In particular, for everyday monitoring of the air environment in enclosed spaces, in transport, where PM concentration is increased [16], the portable individual sensors of micro-, nanoparticles being able to classify them by size and material are required.

The task of creating microparticle detectors includes two aspects:

– sorting of micro/nanoparticles entering the detector by size and material,

– proper detection of particles of the same type and their classification by size, etc.

Technologies and methods of microelectromechanics, microfluidics, and microoptics make it possible to create portable Lab-on-Chip type sensor systems to detect PM dust particles. This is the subject of the present brief review. Particular attention is paid to the features of detecting of nanometer size PM0.1 and Ultrafine particles. The aim of the study was to develop a multifunctional portable detector of airborne micro/nanoparticles based on microelectromechanical systems (MEMS) and alumina technology for industry, transport, medicine, public and residential buildings.

Micro/nanoparticles detection

General classification

Gas analyzers are used to control environmental pollution with gas and vaporous harmful substances; dust meters are used to measure concentration of dispersed pollutants. To get reliable data on the air pollution level, it is necessary to possess the reliable analytical techniques. The effectiveness of a technique is evaluated by a number of indicators:

– selectivity and accuracy;

– reproducibility;

– sensitivity;

– detection limits;

– express analysis ability.

The techniques to measure dust content in air could be divided into the two groups:

---

[1] Sanitary Rules and Norms of the Russian Federation 1.2.3685-21. Hygienic Standards and Requirements to Ensure the Safety and (or) Harmlessness of Environmental Factors for Humans. Chief State Sanitary Doctor of the Russian Federation. Decree of January 28, 2021, No. 2.

– with separating the dispersed phase: weight (gravimetric), counting (conimetric), radioisotope, photometric types;

– without separating the dispersed phase: optical, photoelectrical, acoustical, electrical ones.

A number of measurement techniques (see below) have been proposed to monitor compliance with the above standards. The measurement can be direct, as observation of effects arising from direct interaction with particles (for example, photons absorption/scattering), or indirect, as observation of secondary effects allowing conclusions to be drawn about the aerosol concentration (see Table for direct techniques). The collection techniques require the particles to be deposited, for example, on a filter for a sufficient period of time to measure them, while online real-time (or near-real) systems determine concentration of suspended PMs continuously.

The measuring instruments provide data on mass concentration, density, sizes, composition, or other particle properties, for example, their ability to absorb/scatter optical or other radiation. The mass concentration is more relevant to health safety monitoring, while optical absorption is most interesting for climate studies as a decisive factor in global warming. The particle size could be directly obtained from a signal, or using additional techniques, such as initial separation of particles in size at entrance, or their ionizing followed by separation with high electric fields, etc.

Table

Direct techniques to measure air/gasborne particulate matters

Technique	Output	Output delay	Time resolution
	Optical		
Aethalometry	black carbon mass	quasi-real-time	minutes
Deposit imaging	particle count, size	minutes	minutes
Direct imaging	particle count, size	real-time	minutes
Lidar	aerosol optical depth	real-time	minutes
Nephelometry	particle count, size	real-time	seconds
Optical particle counting/spectrometry	particle count, size	real-time	seconds
Photometry of soot particles	mass	real-time	seconds
Photo(opto)acoustic spectrometry	absorption	real-time	seconds
Spectropolarimetry	polarization degree	real-time	minutes
	Electrical		
Capacitance	particle count, size	real-time	seconds
Charge	particle count	real-time	seconds
Inductance	particle count, size	real-time	seconds
	Mechanical/Acoustical		
Film acoustic resonator	mass	real-time	minutes
Oscillatory microbalance	mass	real-time	seconds
Photo(opto)acoustic spectrometry	absorption	real-time	seconds
	Others		
Gravimetry	mass	days to weeks	hours
β-irradiation attenuation	mass	minutes	minutes

The important factor affecting the particle size and overall concentration estimation is the air humidity. Microparticles act as condensation cores which leads to significant increase in effective size readings of up to ≈ 70 % relative humidity [17], for example, under optical measurements. On the other hand, this phenomenon is used to count the smallest-size nanoparticles [18]. Also, when collecting aerosol, the moisture accumulates in the filtering material affecting the measured mass [19], optical and electrical properties.

Consider the basic detection techniques of interest to create a compact Lab-on-Chip type device.

Gravimetry

This direct technique, despite its non-compactness and non-viability for Lab-on-Chip technology, should be mentioned as the established standard for PM measurements [20]. The technique is based on collecting particles by depositing them on a filter for a given time at a certain air flow rate, followed by their weighing and additional analysis. To collect a sufficient mass of microparticles, the sampler should be activated for a long time, so it shows average values and does not allow tracking short-term effects. To measure simultaneously PM10 and PM2.5, multiple samplers should be used with selective inputs for appropriate sizes.

β-irradiation attenuation

The β-irradiation attenuation measurement is based on absorption of beta radiation in solids to measure PM. However, the absorbed radiation is proportional only to the mass of the filtered substance and does not depend on its density, chemical composition, physical or optical properties. Typically, differential measurements are used, where the filter collects particles from the air flow, and the readings of two Geiger counters are compared, one of which is located before and one after the bleed air flow. The advantages of this technique include high accuracy, as well as shorter averaging time interval and delay compared to gravimetric measurements.

Acoustic techniques

In photoacoustic spectrometry [21], particles pass through a modulated laser beam. The illuminated particles heat up, releasing heat energy into the air. The heated air creates a sound wave whose frequency exactly matches the modulation frequency of the laser. The sound wave is recorded by a sensitive microphone, and its amplitude being proportional to the particles' absorptivity.

Noise is also used to estimate indirectly the amount of airborne microparticles, for instance, to monitor the black carbon and PM concentration through traffic noise [22].

Optical techniques

The main technique to detect PM1 – PM10 microparticles uses a simple light emitting diode (LED)/photodetector optical scheme (Figure 1). Variety of compact sensors uses broadband LED 1 or semiconductor laser irradiation. Photons, scattered by microparticles 2, are detected by a semiconductor photodiode 3 and registered as time-dependent patterns 4. Some techniques have been developed to improve the accuracy of measurements by optimizing the operating modes of the irradiation source, receiver, and data processing procedure. A number of companies on the market produce optical compact sensors.

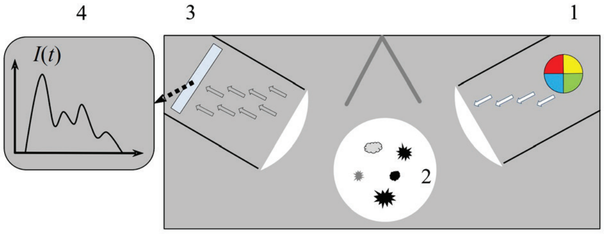

Figure 1 – Multi-wavelength optical sensing of airborne microparticles: 1 – light-emitting diodes; 2 – microparticles flow; 3 – photodetector; 4 – spectral/temporal data [23]

The minimum detected size of PMs cannot be significantly less than the optical beam wavelength. For laser illumination, the 0.4 to 3.3 μm radiation is used. Accordingly, the minimum radius of detected particles cannot be significantly less than ~ 100 nm. To improve the informativity of measurement, in particular, to estimate the size distribution of particles, the multi-wavelength laser systems are considered [24], as well as in the multiwave ethalometry technique [25]. The multiwavelength detector [24] allows the analysis of microparticles by size. Optical feedback could stabilize the laser source measuring [26]. For instance, the optical particle counter of the Cubic Sensor and Instrument Co. [27] based on laser scattering technology could automatically identify and simultaneously output the number of particles in 6 channels including 0.3, 0.5, 1.0, 2.5, 5.0 and 10 μm size particles.

Microelectromechanical system

MEMS elements are used to detect and analyze the airborne micro-, nanoparticles [28, 29]. This approach makes it possible, in principle, to perform serial and batch production of devices using microelectronics technology to miniaturize and reduce the cost of sensors and systems. Most MEMS sensors are based on electric counting of particles. These sensors have no high sensitivity due to small volume and flow of detected air and corresponding small value of detected electric current.

The microbalances are the mechanical systems used to determine PM mass concentration. In an oscillating microbalance, the particles are deposited in a small conical glass tube. The tube' natural frequency is changed by additional mass of deposited particles, thus, the particles mass could be determined. Unfortunately, the microbalance monitoring is sensitive to mechanical noise and temperature fluctuations [30].

The MEMS resonator systems have been proposed, such as cavity film acoustic resonator [31] or surface acoustic wave resonator [32] which use the thermophoresis effects to deposit particles on a sensitive element and measure the resonant frequency change in real time.

Capacitive detectors

Capacitive detection is a rather new technique to detect microparticles where the capacitance change is measured (typically ~ 10 zF = 10^{-20} F) that occurs when a microparticle(s) enters the electric field between two electrodes, or when they deposited on the surface of a CMOS logic gate [33]. The capacitance change amplitude can be used to estimate particle(s) diameter [34]. This technique is under development and could enable detection of particles smaller than 1 μm [35].

Nanoparticles detection

Detection of microparticles of some tens of nanometer has its own features when the above methods are unsuitable in many cases. For the purposes of sensor miniaturization, the following solutions could be considered.

The known condensation type counter sensor use the technique of heterogeneous condensation of water vapors on nanoparticles [36]. The optical detection technique is used to count the formed micrometer-size water drops. The condensation type counter method is capable of detecting single nanoparticles [37] and possesses a high resolution in nanoparticle sizing when using a differential mobility analyzer nanoparticle selector [38]. The system includes a reservoir, a saturator, a condenser and a miniature optical drop detector.

In the electrical technique, the electrically charged nanoparticles in the device are counted by measuring the electric current in the circuit under their capturing (Figure 2).

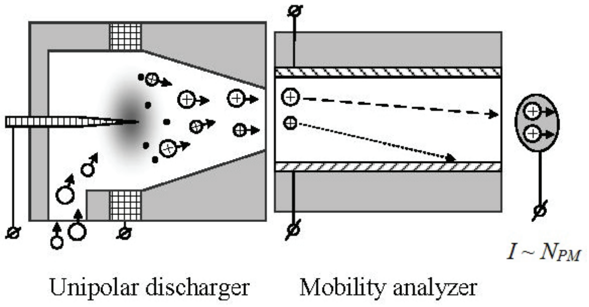

Figure 2 – Electrical discharge/microfluidic detection of nanoparticles [39]

Such devices are distinguished by high accuracy and selectivity. The devices require high-voltage unit to pre-charge the entering nanoparticles.

Sorting

Separation of nano- and microparticles prior to detection makes it possible to increase the sensitivity and selectivity of the detector, both in sizes and material thereof. Among the selection techniques, the two are most suitable for integration in a lab-on-chip device – virtual impactor and dielectrophoresis.

Virtual impactor

The aerial microjet chip classifies microparticles in size using an inertial separator – so-called *virtual impactor* (Figure 3).

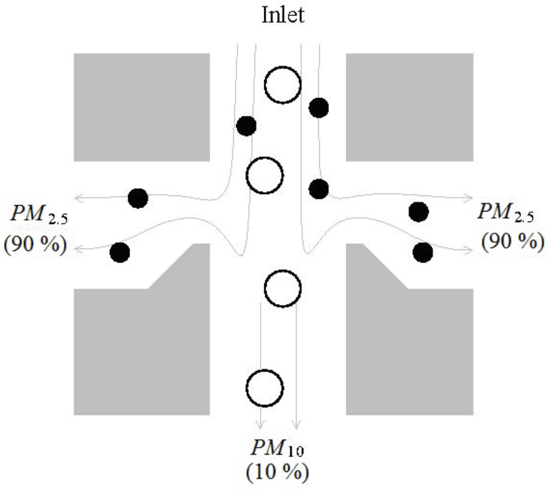

Figure 3 – Virtual impactor to select microparticles

Dielectrophoresis

The electric forces acting to micro-, nanoparticles under electrophoresis and dielectrophoresis (DEF) effects present the effective sensitive method to manipulate the particles when the device size lowers to Lab-on-Chip scale [40].

DEF is a selective electrokinetic effect including displacement of uncharged microparticles in inhomogeneous electric field due to interaction of their electrical dipole (induced or own) with electric field gradient. DEF forces action is defined by both the scale and electric properties of the particles and surrounding medium (gas or liquid). To create an inhomogeneous and non-stationary electric field in the DEF method, both the stationary and alternating electric fields are used, including additional constant bias. In particular, DEF method is successfully used to separate metallic and dielectric microparticles [41].

Lab-on-Chip MEMS detector of airborne nanoparticles

The above approaches are used in the MEMS detector under development where the micromembrane and capacitive measuring elements are used to gain higher sensitivity without pre-charging micro- , nanoparticles and with possibility to implement a complete measuring procedure in a single Lab-on-Chip device (Figure 4) [42].

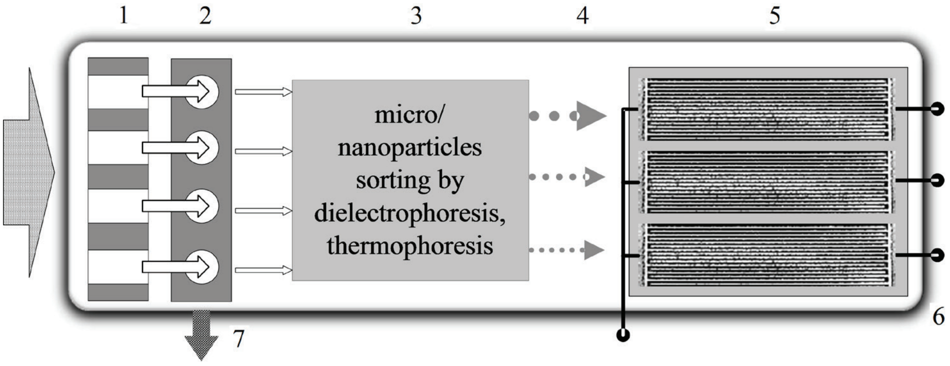

Figure 4 – MEMS nanoparticle detector: 1 – porous membrane; 2 – virtual impactor; 3 – separator; 4 – nanoparticles; 5 – capacitive detector; 6 – output signals; 7 – microparticles outlet (to optical detector)

The detector contains a thin alumina plate with periodic array of micro/nanometer size through holes 1 and virtual impactor 2 for size separation of the particles. The subsequent dielectrophoretic/thermophoretic sorting 3 with gradient electric/thermal fields allows to separate PMs in narrowed nanosize intervals providing their oriented movement 4, as well as to determine their amount using the anodic alumina based interdigitated electrode matrices 5 in every channel for subsequent capacitive measurements 6. The additional detection of microparticles 7 from the impactor 2 could be performed by optical counting technique.

Conclusion

The classification of airborne microparticles by main types and size is presented. The main techniques for separating and detecting airborne solid microparticles of micrometer and submicrometer size using optical, capacitive, microelectromechanical system and other sensing elements are considered. A prototype design of a micro-, nanoparticles detector based on alumina technology using microelectromechanical system elements for a compact Lab-on-Chip type sensor is presented. The prototype design contains mechanical filtering elements, dielectrophoretic/thermophoretic cells, and capacitive detecting elements with separate output signals to estimate the amount and size of nanoparticles, and to detect additionally the microparticles by an optical technique.

References

1. World Health Organization (WHO). 7 million premature deaths annually linked to air pollution,014. Access mode: http://www.who.int/mediacentre/news/releases/2014/air-pollution. Date of access: 11.01.2021.

2. International Standardization Organization. ISO 23210:2009. Stationary source emissions – determination of PM10/PM2.5 mass concentration in flue gas – measurement at low concentrations by use of impactors. Last reviewed and confirmed in 2015. Access mode: https://www.iso.org/standard/53379.html. Date of access: 11.01.2021.

3. Butterfield D.M., Quincey P. Measurement science issues relating to PM10 and PM2.5 airborne particles. National Physical Laboratory (NPL) Report AS 15, 2007, 36 p. ISSN 1754-2928. Teddington, Middlesex, UK.

4. World Health Organization (WHO). Air quality guidelines for particulate matter, ozone, nitrogen dioxide and sulfur dioxide. Global update 2005. Summary of risk assessment. Access mode: http://whqlibdoc.who.int/hq/2006/WHO_SDE_PHE_OEH_06.02_eng.pdf. Date of access: 11.01.2021.

5. European Commission. Directive 2008/50/EC of the European Parliament and of the Council of 21 May 2008 on ambient air quality and cleaner air for Europe. Access mode: http://eur-lex.europa.eu/legal- content/EN/TXT/PDF/?uri=CELEX:32008L0050&from=EN. Date of access: 11.01.2021.

6. U.S. Environmental Protection Agency. National Ambient Air Quality Standards for Particulate Matter. Federal Register 61144, 2006. Access mode: https://www.gpo.gov/fdsys/pkg/FR-2006-10-17/pdf/06-8477.pdf. Date of access: 11.01.2021.

7. China Environmental Science Press. Ambient Air Quality Standards. National Standard of the People's Republic of China GB 3095, 2012. Access mode: http://kjs.mep.gov.cn/hjbhbz/bzwb/dqhjbh/dqhjzlbz/201203/W020120410330232398521.pdf. Date of access: 11.01.2021.

8. Long C.M., Nascarella M.A., Valberg P.A. Carbon black vs. black carbon and other airborne materials containing elemental carbon: physical and chemical distinctions. Review. *Environmental Pollution*, 2013, vol. 181, pp. 271–286.
DOI: 10.1016/j.envpol.2013.06.009

9. Andreae M.O., Gelencsér A. Black carbon or brown carbon? The nature of light-absorbing carbonaceous aerosols. *Atmospheric Chemistry and Physics*, 2006, vol. 6, pp. 3131–3148.
DOI: 10.5194/acp-6-3131-2006

10. Levy L., Chaudhuri I.S., Krueger N., McCunney R.J. Does carbon black disaggregate in lung fluid? A critical assessment. *Chemical Research in Toxicology*, 2012, vol. 25, pp. 2001–2006.
DOI: 10.1021/tx300160z

11. Pan M., Lednicky J.A., Wu C.-Y. Collection, particle sizing and detection of airborne viruses. *Journal of Applied Microbiology*, 2019, vol. 127, pp. 1596–1611.
DOI: 10.1111/jam.14278

12. Cuffari B. The size of SARS-CoV-2 and its implications. News-Medical.net – An AZoNetwork Site. Access mode: www.news-medical.net. Date of access: 02.15.2021.

13. Tang J.W. The effect of environmental parameters on the survival of airborne infectious agents. *Journal of the Royal Society Interface*, 2009, vol. 6 (Suppl. 6), pp. S737–746.
DOI: 10.1098/rsif.2009.0227.focus

14. Hinds W.C. Aerosol Technology: Properties, Behavior, and Measurement of Airborne Particles. 2nd edition. New York, NY: Wiley. 1998. ISBN: 978-0-471-19410-1.

15. Li X., Qi X., Ma J., Pan Y., Tian T., Zhang Y., Li Z., Li W., Sun L., Zhang L., Zhang Z., Wang Q., Yao M. SARS-CoV-2 remained airborne for a prolonged time in a lockdown confined space. *Aerosol and Air Quality Research*, 2022, vol. 22, pap. 210131.
DOI: 10.4209/aaqr.210131

16. Zhao J., Birmili W., Wehner B., Daniels A., Weinhold K., Wang L., Merkel M., Kecorius S., Tuch T., Franck U., Hussein T., Wiedensohler A. Particle mass concentrations and number size distributions in 40 homes in Germany: indoor-to-outdoor relationships, diurnal and seasonal variation. *Aerosol and Air Quality Research*, 2020, vol. 20, pp. 576–589.
DOI: 10.4209/aaqr.2019.09.0444

17. Chow J.C., Watson J.G. Guideline on Speciated Particulate Monitoring. Prepared for N. Frank, J. Homolya, Eds. US Environmental Protection Agency. Draft 3. 1998. Access mode: https://www3.epa.gov/ttnamti1/files/ambient/pm25/spec/drispec.pdf. Date of access: 11.01.2021.

18. Yoo Seong-Jae, Jeon Jae-Wan, Kim Yong-Jun. Lab-on-printed circuit board based water harvesting condensation particle counter for ubiquitous monitoring of airborne ultrafine particles. *Journal of Aerosol Science*, 2022, vol. 160, pap. 105911 (14 p.).
DOI: 10.1016/j.jaerosci.2021.105911

19. Karali D., Loupa G., Rapsomanikis S. Nephelometer sensitivities for the determination of PM2.5 mass concentration in ambient and indoor air. *Aerosol and Air*

Quality Research, 2020, vol. 21, no. 1, pap. 200159 (8 p.). **DOI:** 10.4209/aaqr.2020.04.0159

20. European Standard EN 12341:2014. Ambient air – Standard gravimetric measurement method for the determination of the PM10 or PM2.5 mass concentration of suspended particulate matter. Access mode: https://www.nbn.be/shop/en/standard/nbn-en-12341-2014_38804/. Date of access: 11.01.2021.

21. Foster K., Pokhrel R., Burkhart M., Murphy S. A novel approach to calibrating a photoacoustic absorption spectrometer using polydisperse absorbing aerosol. *Atmospheric Measurement Techniques*, 2019, vol. 12, no. 6, pp. 3351–3363.
DOI: 10.5194/amt-12-3351-2019

22. Dekoninck L., Botteldooren D., Panis L.I., Hankey S., Jain G., Karthik S., Marshall J. Applicability of a noise-based model to estimate in-traffic exposure to black carbon and particle number concentrations in different cultures. *Environment International*, 2015, vol. 74, pp. 89–98. **DOI:** 10.1016/j.envint.2014.10.002

23. Mukhurov M., Khodin A. Multiwavelength sensor of gas/airborne microparticles. 14th International Scientific and Technical Conference “Instrumentation – 2021”, Minsk, November 17–19 2021. Proc. BNTU, Minsk, Belarus, 2021, pp. 436–438 (in Russian).

24. Di Huige, Wang Zhixiang, Hua Dengxin. Precise size distribution measurement of aerosol particles and fog droplets in the open atmosphere. *Optics Express*, 2019, vol. 27, no. 12, pp. A890–A908.
DOI: 10.1364/OE.27.00A890

25. Saturno J., Pöhlker C., Massabò D., Brito J., Carbone S., Cheng Y., Chi X., Ditas F., Hrabě de Angelis I., Morán-Zuloaga D., Pöhlker M.L., Rizzo L.V., Walter D., Wang Q., Artaxo P., Prati P., Andreae M.O. Comparison of different Aethalometer correction schemes and a reference multi-wavelength absorption technique for ambient aerosol data. *Atmospheric Measurement Techniques*, 2017, no. 10, pp. 2837–2850.
DOI: 10.5194/amt-10-2837-2017

26. Rhee C., Yang H., Kim S. A PM1, PM2.5, and PM10 airborne particle detector with laser illumination stabilized by optical feedback. *IEEE Sensors Journal*, 2020, vol. 20, no. 4, pp. 1988–1996.
DOI: 10.1109/JSEN.2019.2949008

27. *Cubic Sensors and Instrument Co., Ltd.* Access mode: https://en.gassensor.com.cn/index.html. Date of access: 01.20.2022.

28. Kim H.-L., Han J.S., Lee S.-M., Kwon H.-B., Hwang J., Kim, Y.-J. Ultrafine particle counter using a MEMS-based particle processing chip. 28th IEEE International Conference on Micro Electro Mechanical Systems (MEMS), Estoril, Portugal, January 18–22, 2015, Proc., pp. 559–562.
DOI: 10.1109/MEMSYS.2015.7051016

29. Wasisto H.S., Merzsch S., Waag A., Uhde E., Salthammer T., Peiner E. Airborne engineered nanoparticle mass sensor based on a silicon resonant cantilever. *Sensors and Actuators B: Chemical*, 2013, no. 180, pp. 77–89.
DOI: 10.1016/j.snb.2012.04.003

30. Gilliam J.H., Hall E.S. Reference and Equivalent Methods Used to Measure National Ambient Air Quality Standards (NAAQS) Criteria Air Pollutants – Vol. I. U.S. Environmental Protection Agency, EPA/600/R-16/139. 2016. Access mode: https://cfpub.epa.gov/si/si_public_record_report.cfm?dirEntryId=321491. Date of access: 11.01.2021.

31. Paprotny I., Doering F., Solomon P.A., White R.M., Gundel L.A. Microfabricated air-microfluidic sensor for personal monitoring of airborne particulate matter: Design, fabrication, and experimental results. *Sensors and Actuators A: Physical*, 2013, vol. 201, pp. 506–516.
DOI: 10.1016/j.sna.2012.12.026

32. Hao W.-C., Liu J.-L., Liu M.-H., He S.-T. Development of a new surface acoustic wave based PM 2.5 monitor. In: 2014 Symposium on Piezoelectricity, Acoustic Waves, and Device Applications (SPAWDA), Proc. IEEE, 2014, pp. 52–55.
DOI: 10.1109/SPAWDA.2014.6998524

33. Ciccarella P., Carminati M., Sampietro M., Ferrari G. 28.7 CMOS monolithic airborne-particulate-matter detector based on 32 capacitive sensors with a resolution of 65zF rms. 2016 IEEE International Solid-State Circuits Conference (ISSCC), 2016, pp. 486–488.
DOI: 10.1109/ISSCC.2016.7418119

34. Carminati M., Ferrari G., Sampietro M. Emerging miniaturized technologies for airborne particulate matter pervasive monitoring. *Measurement*, 2017, vol. 101, pp. 250–256.
DOI: 10.1016/j.measurement.2015.12.028

35. Carminati M., Ciccarella P., Sampietro M., Ferrari G. Single-chip CMOS capacitive sensor for ubiquitous dust detection and granulometry with sub-micrometric resolution. In: Sensors: Proc. of the Third National Conference on Sensors, February 23-25, 2016, Rome, Italy. Ed. by B. Andò, F. Baldini, C. Di Natale, G. Marrazza, P. Siciliano. *Springer International Publishing*, 2016, pp. 8–18.
DOI: 10.1007/978-3-319-55077-0_2

36. Stolzenburg M.R. McMurry P.H. An ultrafine aerosol condensation nucleus counter. Aerosol Science and Technology, 1991, vol. 14, no.1, pp.48–65.
DOI: 10.1080/02786829108959470

37. Kangasluoma J., Kuang C., Wimmer D., Rissanen M.P., Lehtipalo K., Ehn M., Worsnop D.R., Wang J., Kulmala M., Petäjä T. Sub-3 nm particle size and composition dependent response of a nano-CPC

battery. Atmospheric Measurement Techniques, 2014, no. 7, pp. 689–700. **DOI:** 10.5194/amt-7-689-2014

38. Yoo Seong-Jae, Kwon Hong-Beom, Hong Ui-Seon, Kang Dong-Hyun, Lee Sang-Myun, Han Jang-seop, Hwang Jungho, Kim Yong-Jun. Microelectro-mechanical-system-based condensation particle counter for real-time monitoring of airborne ultrafine particles. *Atmospheric Measurement Techniques*, 2019, vol. 12, no. 10, pp. 5335–5345. **DOI:** 10.5194/amt-12-5335-2019

39. Kwon Hong-Beom, Song Woo-Young, Lee Tae Hoon, Lee Seung-Soo, Kim Yong-Jun. Monitoring the effective density of airborne nanoparticles in real time using a microfluidic nanoparticle analysis chip. *ACS Sensors*, 2021, vol. 6, pp. 137−147.
DOI: 10.1021/acssensors.0c01986

40. Voldman J. Electrical forces for microscale cell manipulation. *Annual Review of Biomedical Engineering*, 2006, no. 8, pp. 425–454.
DOI: 10.1146/annurev.bioeng.8.061505.095739

41. Pesch G.R., Du F. A review of dielectrophoretic separation and classification of non-biological particles. *Electrophoresis*, 2020, vol. 42, no. 1–2, pp. 1–19.
DOI: 10.1002/elps.202000137

42. Mukhurov M., Khodin A. Means and methods to control the air ambient dust in residential and public buildings. In: Scientific and Technical Progress in Housing and Communal services. III International Scientific and Practical Conference. Minsk, October 7–8, 2021. Proc. Chapter 2, pp. 151–159 (in Russian).

Кристалл Er^{3+},Yb^{3+}:$YGdSiO_5$ для лазеров спектрального диапазона 1,5–1,6 мкм

К.Н. Горбаченя[1], А.С. Ясюкевич[1], В.Э. Кисель[1], Н.А. Толстик[2], А.А. Тараченко[1], В.И. Гоман[1], Л.К. Павловский[1], В.А. Орлович[3], Е.А. Волкова[4], В.О. Япаскурт[4], Н.В. Кулешов[1]

[1]*НИЦ оптических материалов и технологий,*
Белорусский национальный технический университет,
пр-т Независимости, 65, г. Минск 220013, Беларусь

[2]*Норвежский университет науки и технологий,*
Хогсколеринген N-7491, г. Трондхейм, Норвегия

[3]*Институт физики имени Б.И. Степанова Национальной академии наук Беларуси,*
пр-т Независимости, 68-2, г. Минск 220072, Беларусь

[4]*Московский государственный университет имени М.В. Ломоносова,*
Ленинские горы, ГСП-1, г. Москва 119234, Россия

Поступила 04.02.2022
Принята к печати 23.03.2022

Твердотельные эрбиевые лазеры, излучающие в спектральной области 1,5–1,6 мкм, представляют большой интерес для различных практических применений. Из доступных на сегодня лазерных материалов для получения стимулированного излучения в области 1,5 мкм наибольшее распространение получили фосфатные стёкла, легированные ионами Er^{3+}. Однако максимальные выходные мощности таких лазеров ограничены несколькими сотнями милливатт из-за низких термических характеристик стекла, поэтому поиск подходящей кристаллической матрицы для ионов эрбия является актуальным и в настоящее время.

В работе представлены результаты исследований спектроскопических свойств кристалла иттрий-гадолиниевого силиката, легированного ионами эрбия и иттербия – Er^{3+},Yb^{3+}:$YGdSiO_5$(YGSO). Измерены спектры поглощения и люминесценции в поляризованном свете, определены времена жизни возбуждённых состояний активных ионов. Измерения спектров поглощения из возбуждённого состояния показали, что полоса поглощения из возбуждённого состояния не перекрывается с полосой усиления в спектральной области 1,5–1,6 мкм. Проведена оценка эффективности переноса энергии от ионов иттербия к ионам эрбия. Выполнен расчёт спектров поперечных сечений вынужденного излучения и усиления.

Ключевые слова: эрбий, иттербий, иттрий-гадолиниевый силикат, спектроскопические свойства.

DOI: 10.21122/2220-9506-2022-13-1-17-26

Адрес для переписки:
Горбаченя К.Н.
Центр оптических материалов и технологий,
Белорусский национальный технический университет,
пр-т Независимости, 65, Минск 220013, Беларусь
e-mail: gorby@bntu.by

Address for correspondence:
Gorbachenya K.N.
Center for Optical Materials and Technologies,
Belarusian National Technical University,
Nezavisimosty Ave., 65, Minsk 220013, Belarus
e-mail: gorby@bntu.by

Для цитирования:
К.Н. Горбаченя, А.С. Ясюкевич, В.Э. Кисель, Н.А. Толстик, А.А. Тараченко, В.И. Гоман, Л.К. Павловский, В.А. Орлович, Е.А. Волкова, В.О. Япаскурт, Н.В. Кулешов.
Кристалл Er^{3+},Yb^{3+}:$YGdSiO_5$ для лазеров спектрального диапазона 1,5–1,6 мкм.
Приборы и методы измерений.
2022. – Т. 13, № 1. – С. 17–26.
DOI: 10.21122/2220-9506-2022-13-1-17-26

For citation:
K.N. Gorbachenya, A.S. Yasukevich, N.A. Tolstik, V.E. Kisel, A.A. Tarachenko, V.I. Homan, L.K. Pavlovskiy, V.A. Orlovich, E.A. Volkova, V.O. Yapaskurt, N.V. Kuleshov.
[Er^{3+},Yb^{3+}:$YGdSiO_5$ Crystal as Gain Media for Lasers Emitting in the Spectral Range of 1.5–1.6 μm].
Devices and Methods of Measurements.
2022, vol. 13, no. 1, pp. 17–26 (in Russian).
DOI: 10.21122/2220-9506-2022-13-1-17-26

Er^{3+},Yb^{3+}:$YGdSiO_5$ Crystal as Gain Media for Lasers Emitting in the Spectral Range of 1.5–1.6 µm

K.N. Gorbachenya[1], A.S. Yasukevich[1], N.A. Tolstik[2], V.E. Kisel[1], A.A. Tarachenko[1], V.I. Homan[1], L.K. Pavlovskiy[1], V.A. Orlovich[3], E.A. Volkova[4], V.O. Yapaskurt[4], N.V. Kuleshov[1]

[1]Center for Optical Materials and Technologies,
Belarusian National Technical University,
Nezavisimosty Ave., 65, Minsk 220013, Belarus

[2]Norwegian University of Science and Technology,
Hogskoleringen 5, N-7491, Trondheim, Norway

[3]B.I. Stepanov Institute of Physics of the National Academy of Sciences of Belarus,
Nezavisimosti Ave., 68-2, Minsk 220072, Belarus

[4]Lomonosov Moscow State University,
Leninskie Gory, GSP-1, Moscow 119234, Russia

Received 04.02.2022
Accepted for publication 23.03.2022

Abstract

Solid-state erbium lasers, emitting in the spectral range of 1.5–1.6 µm, are of great interest for several industrial applications. Nowadays the Er:glass is the most widespread laser material for obtaining laser radiation at the wavelength near 1.5 µm. However, the maximal output powers of such lasers are restricted by hundreds of milliwatts because low thermal characteristics of the glass host. By this reason the search for new crystalline hosts doped with erbium ions is the actual task.

In this article the investigation results of spectroscopic properties of Er^{3+},Yb^{3+}:$YGdSiO_5$(YGSO) crystals are reported. Polarized absorption and luminescence spectra were measured. The lifetimes of energy levels were determined. The excited state absorption spectra were measured. It was shown that excited state absorption band does not overlap with gain band in the range 1.5–1.6 µm. The energy transfer efficiency from ytterbium to erbium ions was estimated. The stimulated emission and gain cross-section spectra for Er^{3+} ions in YGSO were calculated.

Keywords: erbium, ytterbium, yttrium-gadolinium silicate crystal, spectroscopic properties.

DOI: 10.21122/2220-9506-2022-13-1-17-26

Адрес для переписки:
Горбаченя К.Н.
Центр оптических материалов и технологий,
Белорусский национальный технический университет,
пр-т Независимости, 65, Минск 220013, Беларусь
e-mail: gorby@bntu.by

Address for correspondence:
Gorbachenya K.N.
Center for Optical Materials and Technologies,
Belarusian National Technical University,
Nezavisimosty Ave., 65, Minsk 220013, Belarus
e-mail: gorby@bntu.by

Для цитирования:
К.Н. Горбаченя, А.С. Ясюкевич, В.Э. Кисель, Н.А. Толстик,
А.А. Тараченко, В.И. Гоман, Л.К. Павловский, В.А. Орлович,
Е.А. Волкова, В.О. Япаскурт, Н.В. Кулешов.
Кристалл Er^{3+},Yb^{3+}:$YGdSiO_5$ для лазеров спектрального
диапазона 1,5–1,6 мкм.
Приборы и методы измерений.
2022. – Т. 13, № 1. – С. 17–26.
DOI: 10.21122/2220-9506-2022-13-1-17-26

For citation:
K.N. Gorbachenya, A.S. Yasukevich, N.A. Tolstik, V.E. Kisel,
A.A. Tarachenko, V.I. Homan, L.K. Pavlovskiy, V.A. Orlovich,
E.A. Volkova, V.O. Yapaskurt, N.V. Kuleshov.
[Er^{3+},Yb^{3+}:$YGdSiO_5$ Crystal as Gain Media for Lasers Emitting
in the Spectral Range of 1.5–1.6 µm].
Devices and Methods of Measurements.
2022, vol. 13, no. 1, pp. 17–26 (in Russian).
DOI: 10.21122/2220-9506-2022-13-1-17-26

Введение

Твердотельные эрбиевые лазеры, излучающие в спектральной области 1,5–1,6 мкм, представляют большой интерес для различных практических применений [1]. Из доступных на сегодня лазерных материалов для получения стимулированного излучения в области 1,5 мкм наибольшее распространение получили фосфатные стёкла, легированные ионами Er^{3+}. Спектроскопические свойства эрбиевых стёкол, такие как малое время жизни энергетического уровня $^4I_{11/2}$, минимизирующее процессы поглощения из возбуждённого состояния и ап-конверсии, и высокий квантовый выход люминесценции в области 1,5 мкм, делают их очень эффективной лазерной средой. Кроме того, преимуществами лазеров на эрбиевых стёклах является их простота, надёжность эксплуатации и относительно низкая себестоимость. Однако максимальные средние выходные мощности таких лазеров ограничены несколькими сотнями милливатт из-за низких термических характеристик стекла, поэтому поиск подходящей кристаллической матрицы для ионов эрбия является актуальным и в настоящее время [2].

Лазерная генерация на ионах Er^{3+} с диодной накачкой была реализована в таких кристаллических матрицах как $Y_3Al_5O_{12}$, $KLu(WO_4)_2$, Lu_2SiO_7, YVO_4, однако достигнутые выходные характеристики были достаточно низкими [3–6]. Хорошо себя зарекомендовали кристаллы оксоборатов, легированные ионами эрбия и иттербия [7–11]. При использовании кристалла $Er,Yb:GdAl_3(BO_3)_4$ несколько лет назад была получена генерация в непрерывном режиме генерации с максимальной выходной мощностью до 1 Вт на длине волны 1550 нм при дифференциальной эффективности по поглощённой мощности накачки 30 % [12]. В режиме пассивной модуляции добротности продемонстрирован высокочастотный импульсный режим генерации при использовании различных насыщающихся поглотителей [13–15].

Кристаллы иттриевого и гадолиниевого силикатов Y_2SiO_5(YSO) и Gd_2SiO_5(GSO), легированные ионами эрбия и иттербия, известны в литературе как перспективные лазерные среды [16–18]. Интересным также представляется исследование кристаллов смешанного иттрий-гадолиниевого силиката $YGdSiO_5$(YGSO), в котором сильное штарковское расщепление уровней, характерное для кристалла гадолиниевого силиката, сочетается с более изотропной структурой иттриевого силиката, при этом, в отличие от кристаллов GSO, не происходит двойникование при росте кристаллов, что значительно облегчает выращивание больших кристаллов высокого оптического качества [19].

В данной работе представлены результаты исследований спектроскопических свойств кристаллов иттрий-гадолиниевого силиката, легированного ионами эрбия и иттербия – $Er^{3+},Yb^{3+}:YGdSiO_5$(YGSO).

Объекты и методики исследования

Кристалл Er,Yb:YGSO является двуосным анизотропным кристаллом и принадлежит к моноклинной сингонии C2/c с параметрами элементарной ячейки a = 1,2547 нм, b = 0,6750 нм, c = 1,0477 нм, β = 102,7933° [19]. Элементный состав монокристалла изучался с помощью энергодисперсионного спектрометра *X-Max*^{n}-50 (*Oxford Instruments Ltd*., *GB*), установленного на базе растрового электронного микроскопа *JSM-IT*500 (*Jeol Ltd*., *Japan*) с вольфрамовым термоэмиссионным катодом[1]. По результатам определено, что массовое содержание ионов Er^{3+} и Yb^{3+} в кристалле составило 0,3 мас.% и 3,5 мас.%, соответственно. Внешний вид выращенного кристалл Er,Yb:YGSO приведён на рисунке 1.

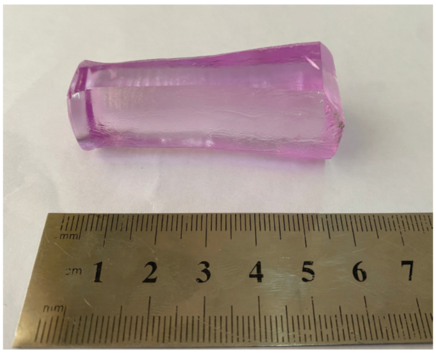

Рисунок 1 – Кристалл Er,Yb:YGSO

Figure 1 – The Er,Yb:YGSO crystal

---

[1] Измерения проводились в лаборатории локальных методов исследования вещества геологического факультета МГУ имени М.В. Ломоносова на оборудовании, приобретенном в рамках «Программы развития МГУ».

Для исследования спектроскопических свойств кристаллов использовались плоскопараллельные пластинки толщиной 2,0 ± 0,1 мм, ориентированные вдоль осей кристалла *a*, *b*, *c*. Измерение абсорбционных свойств производилось при комнатной температуре на двулучевом спектрофотометре *Varian CARY* 5000 в двух спектральных областях: 850–1050 нм, соответствующей энергетическим переходам $^2F_{7/2}\rightarrow{}^2F_{5/2}$ ионов иттербия и $^4I_{15/2}\rightarrow{}^4I_{11/2}$ ионов эрбия, и 1400–1650 нм, соответствующей энергетическому переходу $^4I_{15/2}\rightarrow{}^4I_{13/2}$ ионов эрбия. Для записи спектров в поляризованном свете в оба канала спектрофотометра помещались поляризационные призмы Глана–Тейлора. Спектральное разрешение прибора составляло 0,5 нм.

Измерение спектров люминесценции кристаллов Er,Yb:YGSO проводилось по методу синхронного детектирования при использовании экспериментальной установки, схема которой приведена на рисунке 2.

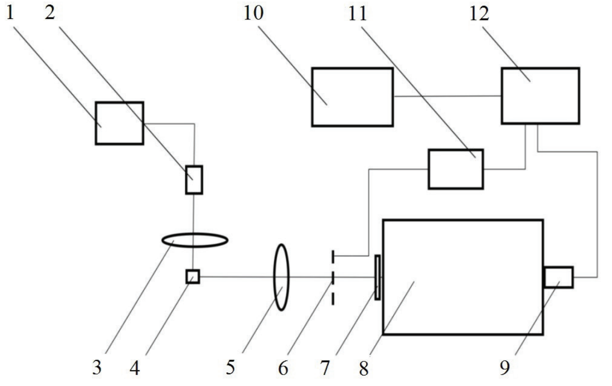

Рисунок 2 – Схема экспериментальной установки для исследования стационарных спектров люминесценции: 1 – блок управления лазерным диодом; 2 – лазерный диод с волоконным выводом; 3, 5 – объективы; 4 – исследуемый образец; 6 – модулятор; 7 – поляризатор; 8 – монохроматор; 9 – фотоприёмник; 10 – компьютер; 11 – блок управления модулятором; 12 – синхронный усилитель

Figure 2 – The setup for measurements of luminescence spectra: 1 – laser diode driver; 2 – fiber coupled laser diode; 3, 5 – lenses; 4 – sample; 6 – chopper; 7 – polarizer; 8 – monochromator; 9 – photodetector; 10 – computer; 11 – modulator driver; 12 – lock-in-amplifier

В качестве источника возбуждения люминесценции использовался InGaAs полупроводниковый лазерный диод 2 с волоконным выводом. Электрическое питание и стабилизация спектрального положения полосы излучения лазерного диода осуществлялись блоком управления лазерным диодом 1. Излучение лазерного диода фокусировалось объективом 3 на исследуемый образец 4. Излучение люминесценции собиралось широкоапертурным объективом 5 на входной щели монохроматора 8. Для записи спектров люминесценции в поляризованном свете перед входной щелью монохроматора помещался тонкоплёночный поляризатор 7. Сигнал с фотоприёмника 9 обрабатывался синхронным усилителем 12, на который также подавался сигнал от модулятора 6. Выходной сигнал с усилителя 12 оцифровывался с помощью аналого-цифрового преобразователя и сохранялся компьютером 10. Регистрация спектров люминесценции выполнялась при комнатной температуре.

Для измерения кинетики затухания люминесценции возбуждённых состояний ионов-активаторов использовалась лабораторная установка, принципиальная схема которой представлена на рисунке 3.

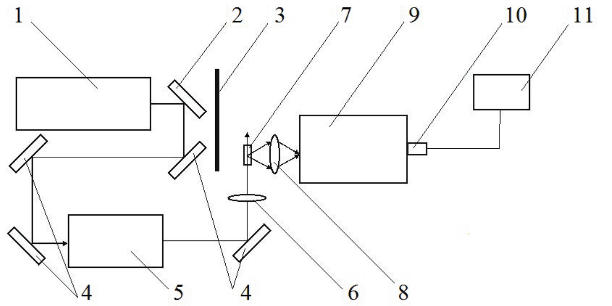

Рисунок 3 – Схема экспериментальной установки для исследования кинетики люминесценции возбуждённых состояний ионов-активаторов: 1 – лазер на кристалле Nd:YAG; 2 – зеркало сепарирующее; 3 – экран; 4 – набор поворотных зеркал; 5 – параметрический генератор света; 6, 8 – объективы; 7 – исследуемый образец; 9 – монохроматор; 10 – фотоприёмник; 11 – осциллограф цифровой

Figure 3 – The setup for investigation of luminescence kinetics: 1 – Nd :YAG laser; 2 – dichroic mirror; 3 – shield; 4 – set of mirrors; 5 – optical parametric oscillator; 6, 8 – lenses; 7 – sample; 9 – monochromator; 10 – photodetector; 11 – oscilloscope

Излучение третьей гармоники импульсного Nd:YAG лазера 1 при помощи сепарирующего зеркала 2 с высоким коэффициентом отражения на длине волны 355 нм и высоким коэффициентом пропускания на длине волны 1064 нм и набора поворотных зеркал 4 с высоким коэффициентом отражения на длине волны 355 нм заводилось в параметрический генератор света 5, который использовался в качестве источника возбуждения люминесценции. Экран 3 использовался для препятствия распространению излучения с длиной волны 1064 нм. Лазерное излучение параметрического генератора света с помощью поворотного зеркала 4 фокусировалось объективом 6 в исследуемый образец 7. Излучение люминесценции собиралось объективом 8 с поверхности исследуемого образца и фокусировалось на входную щель монохроматора 9. Регистрация сигнала люминесценции выполнялась фотоприёмником 10 и цифровым осциллографом. Данные собирались и усреднялись по 512 кинетикам. Для каждого исследуемого образца проводилась серия из трёх измерений.

Измерение спектров поглощения из возбуждённого состояния осуществлялось с помощью лабораторной установки, схема которой приведена на рисунке 4.

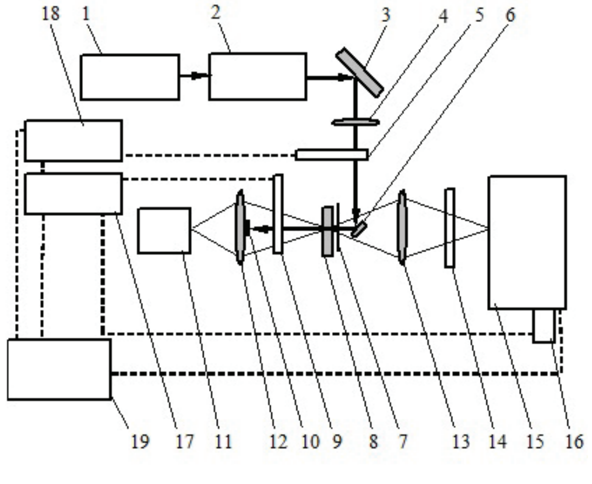

Рисунок 4 – Схема экспериментальной установки для измерения спектров поглощения из возбуждённого состояния: 1 – Nd:YAG лазер; 2 – лазер на сапфире с титаном; 3, 6 – поворотные зеркала; 4, 12, 13 – линзы; 5, 9 – модуляторы; 7 – диафрагма; 8 – исследуемый образец; 10 – экран; 11 – галогенная лампа; 14 – поляризатор; 15 – монохроматор; 16 – фотоприёмник; 17, 18 – синхронные усилители; 19 – компьютер

Figure 4 – The setup for measurement of excited state absorption spectra: 1 – Nd:YAG laser; 2 – Ti:sapphire laser; 3, 6 – mirrors; 4, 12, 13 – lenses; 5, 9 – choppers; 7 – diaphragm; 8 – sample; 10 – shield; 11 – halogen lamp; 14 – polarizer; 15 – monochromator; 16 – photodetector; 17, 18 – lock-in-amplifiers; 19 – computer

Принцип работы установки основан на методике возбуждения-зондирования, когда интенсивный возбуждающий пучок переводит активные ионы исследуемого образца в возбуждённое состояние, а зондирующий пучок малой интенсивности позволяет зарегистрировать изменения коэффициента поглощения этого образца. Возбуждающее излучение генерировалось титан-сапфировым лазером 2, накачиваемым излучением второй гармоники непрерывного Nd:YAG лазера. Промодулированное модулятором 5, излучение возбуждения с помощью поворотных зеркал 3 и 6 и линзы 4 фокусировалось внутри исследуемого образца 8, а непоглотившиеся его остатки «обрезались» экраном 10. Зондирующее излучение генерировалось галогенной лампой 11, обеспечивающей большую расходимость светового пучка. С помощью объектива 12 пучок излучения галогенной лампы собирался на поверхности исследуемого образца. Точечная диафрагма 7, установленная в непосредственной близости от образца, обеспечивала перекрытие возбуждающего и зондирующего пучков. Прошедшее исследуемый образец зондирующее излучение, собиралось объективом 13 на входной щели монохроматора 15, предварительно пройдя через поляризатор 14. За выходной щелью монохроматора был установлен InGaAs фотоприёмник 16, электрический сигнал с которого обрабатывался и усиливался синхронными усилителями 17 и 18, после чего фиксировался компьютером 19. Синхронный усилитель 17 использовал в качестве опорной частоту модулятора 9 и измерял непосредственно интенсивность (I) прошедшего через образец 8 излучения галогенной лампы 11. Синхронный усилитель 18 использовал сигнал усилителя 17 в качестве входного сигнала и частоту модулятора 5 в качестве опорной. Он измерял дифференциальную интенсивность зондирующего излучения, прошедшего через образец, в возбуждённом и невозбуждённом случаях (ΔI). Компьютер 19 производил оцифровку сигналов, деление их друг на друга, сохранение и визуализацию результатов измерений, а также осуществлял управление монохроматором 15.

Значение электрического сигнала, измеряемого установленным в компьютер АЦП, определялось формулой (1):

$$\frac{\Delta I}{I} = n_e LA\,(\sigma_{\text{ПОС}} + \sigma_{\text{ВИ}} - \sigma_{\text{ПВС}}), \qquad (1)$$

где n_e – населённость возбуждённого уровня; L – толщина образца; A – коэффициент усиления синхронного усилителя; $\sigma_{\text{ПОС}}$ – сечение поглощения из основного состояния (ПОС); $\sigma_{\text{ВИ}}$ – сечение вынуждённого излучения (ВИ); $\sigma_{\text{ПВС}}$ – сечение поглощения из возбуждённого состояния (ПВС).

Спектр (1) можно представить в единицах сечений [см^2], если известно значение $n_e LA$. Это можно осуществить при подгонке коротковолнового края спектра (1), где можно пренебречь вкладом $\sigma_{\text{ВИ}}$ и $\sigma_{\text{ПВС}}$, к спектру сечений поглощения из основного состояния ($\sigma_{\text{ПОС}}$).

Результаты исследования спектроскопических свойств

Спектры сечений поглощения кристалла Er,Yb:YGSO в области 1 мкм приведены на рисунке 5. Кристалл характеризуется достаточно широкой полосой поглощения с максимумом около 925 нм для поляризации *E*//*b* и узкой интенсивной полосой на 976 нм с максимальным сечением поглощения 1,65×10^{-20} см^2 для поляризации *E*//*a*. Полуширина полосы с максимумом на 976 нм составляет около 2 нм.

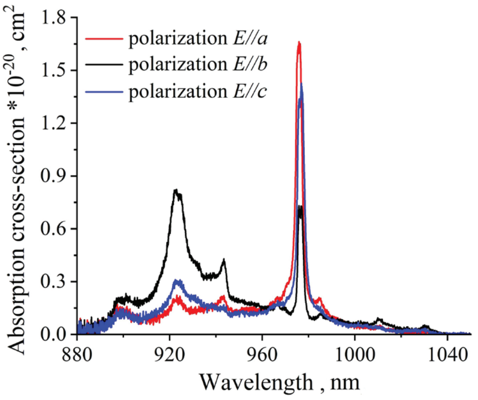

Рисунок 5 – Спектры сечений поглощения кристалла Er,Yb:YGSO в области 1 мкм

Figure 5 – The absorption cross-section spectra of Er,Yb:YGSO crystal near 1 µm

Спектры сечений поглощения в области 1,5 мкм приведены на рисунке 6. Максимальное сечение поглощения достигает 2,5×10^{-20} см^2 на длине волны 1530 нм.

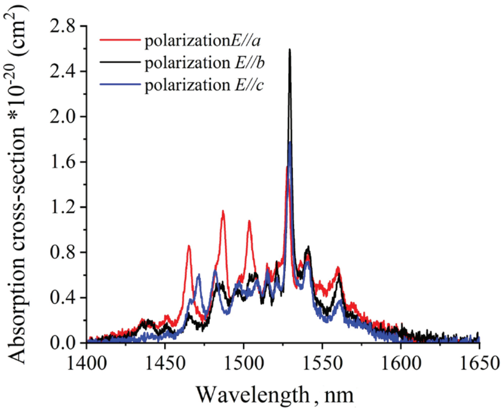

Рисунок 6 – Спектры сечений поглощения кристалла Er,Yb:YGSO в области 1,5 мкм

Figure 6 – The absorption cross-section spectra of Er,Yb:YGSO crystal near 1.5 µm

Целью проведения измерений кинетик люминесценции было определение времени жизни возбуждённых состояний $^4I_{11/2}$ и $^4I_{13/2}$ ионов эрбия и $^2F_{5/2}$ ионов иттербия в кристалле YGSO. Люминесценция возбуждалась импульсным излучением на длине волны 976 нм. Затухание люминесценции с уровня $^4I_{13/2}$ ионов эрбия носило моноэкспоненциальный характер с характерным временем 7,2±0,5 мс. Результаты представлены на рисунке 7. Затухание люминесценции с $^4I_{11/2}$ уровня также имело экспоненциальный характер, и время жизни этого уровня составило 20±1 мкс. Сравнительно короткое время жизни уровня $^4I_{11/2}$ снижает потери, связанные с обратным переносом энергии от ионов эрбия к ионам иттербия и апконверсионными переходами ионов эрбия на вышележащие уровни.

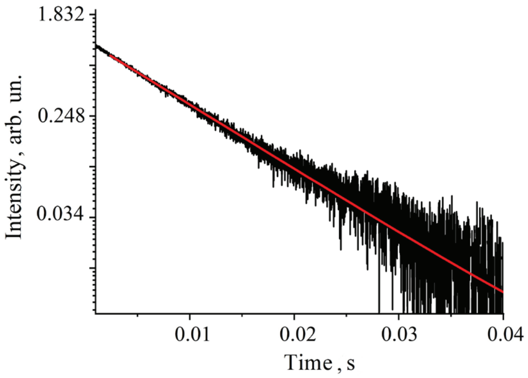

Рисунок 7 – Кинетика затухания люминесценции с уровня $^4I_{13/2}$ ионов эрбия

Figure 7 – The luminescence kinetics from $^4I_{13/2}$ energy level of erbium ions

Эффективность переноса энергии от ионов иттербия к ионам эрбия оценивалась по сокращению времени жизни уровня $^2F_{5/2}$ ионов иттербия в кристалле YGSO, легированном ионами Er и Yb, относительно соответствующего времени жизни в кристалле, легированном только ионами иттербия, используя соотношение [20]:

$$\eta_{Yb\to Er} = 1 - \frac{\tau_{Yb,Er}(^2F_{5/2})}{\tau_{Yb}(^2F_{5/2})}, \qquad (2)$$

где $\eta_{Yb\to Er}$ – эффективность переноса энергии от ионов иттербия к ионам эрбия; $\tau_{Yb,Er}(^2F_{5/2})$ – время жизни ионов иттербия на уровне $^2F_{5/2}$ в кристалле, легированном ионами Er^{3+} и Yb^{3+}; $\tau_{Yb}(^2F_{5/2})$ – время жизни ионов иттербия на уровне $^2F_{5/2}$ в кристалле, легированном только ионами Yb^{3+}.

Время жизни ионов Yb^{3+} на верхнем уровне, измеренное в кристалле Er,Yb:YGSO, составило 180 мкс. В кристалле Yb:YGSO время жизни ионов Yb^{3+} на верхнем уровне составляет 1,92 мс [19]. Таким образом, эффективность переноса энергии Yb→Er в кристалле Er,Yb:YGSO достигает 91 %.

Спектры люминесценции кристалла Er,Yb:YGSO в спектральной области 1400–1700 нм, измеренные при комнатной температуре со спектральным разрешением 0,5 нм, приведены на рисунке 8. Полоса люминесценции в этой области является широкой и структурированной, максимум полосы соответствует длине волны 1530 нм для всех трёх поляризаций. Длинноволновой край полосы люминесценции достигает 1650 нм.

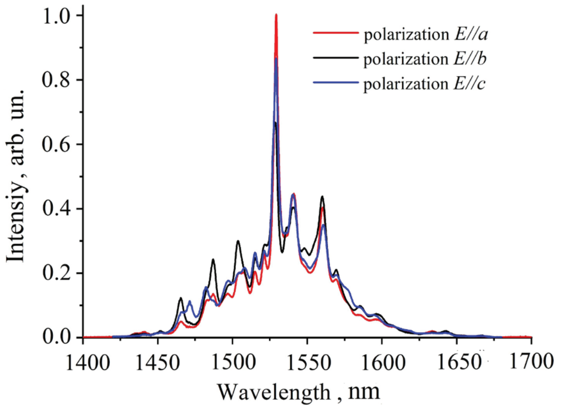

Рисунок 8 – Спектры люминесценции кристалла Er,Yb:YGSO в спектральной области 1400–1700 нм

Figure 8 – The luminescence spectra of Er,Yb:YGSO crystal in the spectral range of 1400–1700 nm

Спектры сечений вынужденного излучения (ВИ) для перехода $^4I_{13/2}\to{}^4I_{15/2}$ ионов эрбия были определены по модифицированному методу соответствия [21]. Для расчёта радиационное время жизни $\tau_{рад}$ уровня $^4I_{13/2}$ ионов эрбия принималось равным измеренному времени жизни уровня $^4I_{13/2}$ [16].

$$\sigma^{\alpha}_{ВИ}(\lambda) = \frac{3\exp(-hc/(kT\lambda))}{8\pi n^2\tau_{рад}c\sum_{\gamma}\int\lambda^{-4}\sigma^{\gamma}_{погл}(\lambda)\exp(-hc/(kT\lambda))d\lambda}\sigma^{\alpha}_{погл}(\lambda), \qquad (3)$$

где $\sigma_{ВИ}(\lambda)$ – поперечное сечение вынужденного излучения на длине волны λ; λ – длина волны света; индексы α и γ обозначают состояние поляризации света; h – постоянная Планка; c – скорость света в вакууме; k – постоянная Больцмана; T – температура среды; n – показатель преломления кристалла; $\sigma_{погл}(\lambda)$ – поперечное сечение поглощения на длине волны λ.

Спектры сечений вынужденного излучения в спектральной области 1400–1650 нм приведены на рисунке 9. Наиболее интенсивный максимум с сечением вынужденного излучения $1{,}2\times10^{-20}$ см^2 наблюдается для поляризации $E//b$ на длине волны 1530 нм.

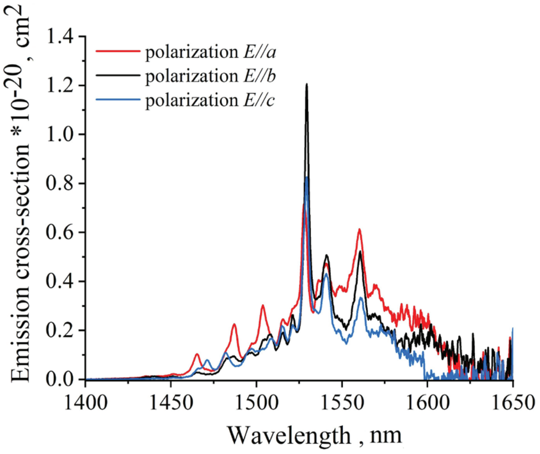

Рисунок 9 – Спектры сечений вынужденного излучения кристалла Er,Yb:YGSO

Figure 9 – The stimulated emission cross-section spectra of Er,Yb:YGSO crystal

На рисунке 10 приведены спектры коэффициента усиления для различных значений относительной населённости β уровня $^4I_{13/2}$ для трёх различных поляризаций:

$$g^{\alpha}(\lambda) = [\beta\sigma^{\alpha}_{ВИ}(\lambda) - (1-\beta)\sigma^{\alpha}_{погл}(\lambda)]N_0, \qquad (4)$$

где $g^{\alpha}(\lambda)$ – коэффициент усиления на длине волны

λ для света с поляризацией α; $\beta = N(^4I_{13/2})/N_{Er}$ – относительная инверсная населённость; $\sigma^{\alpha}_{ви}(\lambda)$ – поперечное сечение вынужденного излучения на длине волны λ; $\sigma^{\alpha}_{погл}(\lambda)$ – поперечное сечение поглощения на длине волны λ; N_0 – полное число ионов эрбия.

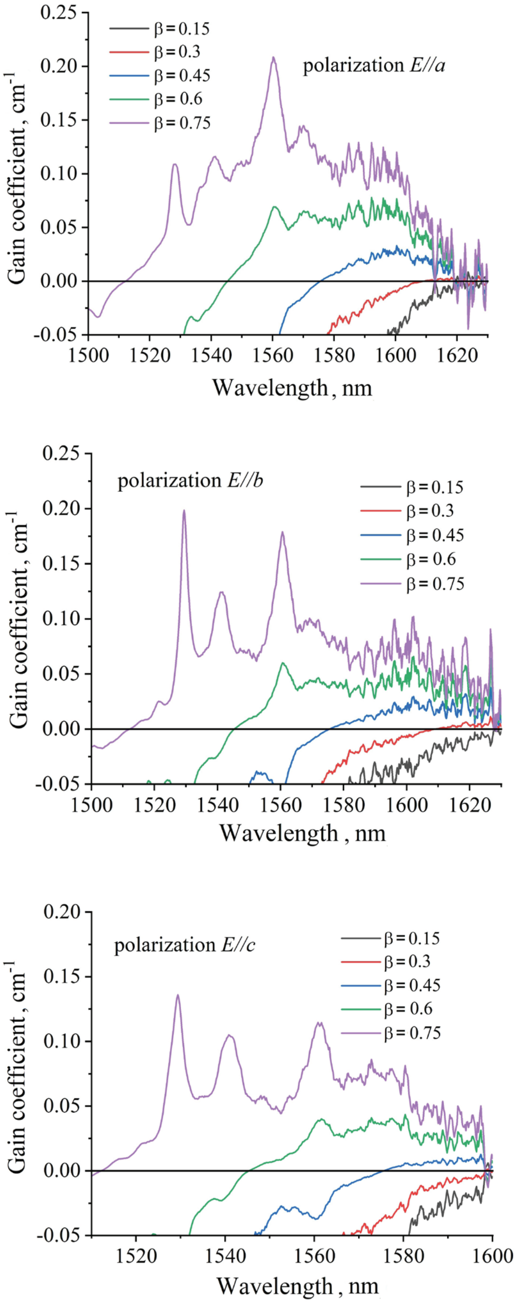

Рисунок 10 – Спектры сечений усиления кристалла Er,Yb:YGSO

Figure 10 – The gain spectra of Er,Yb:YGSO crystal

Поглощение из возбуждённого состояния в области 1,5 мкм (переход $^4I_{13/2} \rightarrow {}^4I_{9/2}$) является одним из самых существенных каналов энергетических потерь в эрбий-содержащих средах. В случае спектрального перекрытия полосы поглощения из возбуждённого состояния с полосой усиления (как, например, в некоторых эрбиевых стёклах [4]) эффективность лазерной генерации в спектральной области 1500–1600 нм может существенно снизиться. Спектр поглощения из возбуждённого состояния кристалла Er,Yb:YGSO приведён на рисунке 11.

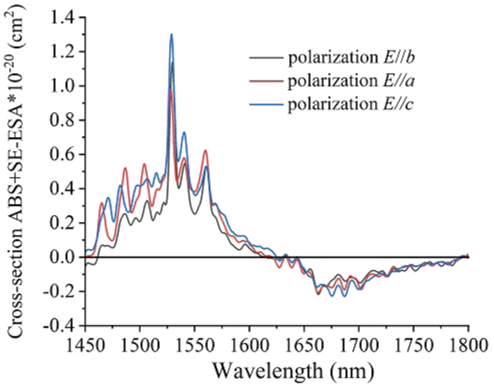

Рисунок 11 – Спектры поглощения из возбуждённого состояния кристалла Er,Yb:YGSO в спектральной области 1450–1800 нм

Figure 11 – The excited state absorption spectra of Er,Yb:YGSO crystal in the spectral range 1450–1800 nm

Спектр показывает, что полосы поглощения из возбуждённого состояния лежат в области 1625–1800 нм (участок отрицательных значений) и практически не перекрываются с полосами усиления в области 1500–1600 нм.

Заключение

Проведены систематические исследования спектроскопических характеристик кристалла Er,Yb:YGSO как лазерной среды на область спектра 1,5–1,6 мкм. Измерены спектры поглощения и люминесценции ионов иттербия и эрбия в поляризованном свете, определены времена жизни возбуждённых состояний этих ионов. Проведена оценка эффективности переноса энергии от ионов иттербия к ионам эрбия. Выполнен расчёт спектров поперечных сечений вынужденного излучения и усиления ионов эрбия. Измерения спектров поглощения из возбуждённого состояния показали, что полоса поглощения из возбуждённого состояния ионов эрбия не перекрывается с полосой усиления в спектральной области 1,5–1,6 мкм. Полученные результаты показали, что кристалл Er,Yb:YGSO является перспективным для использования в качестве активной среды лазеров спектрального диапазона 1,5–1,6 мкм.

References

1. Myers M.J., Myers J.D., Sarracino J.T., Hardy C.R., Guo B., Christian S.M., Myers J.A., Roth F., MyersA.G. LIBS system with compact fiber spectrometer, head mounted spectra display and hand held eye-safe erbium glass laser gun. *Solid State Lasers XIX: Technology and Devices*, 2010, vol. 7578, p. 75782G.
DOI: 10.1117/12.841901

2. Taccheo S., Sorbello G., Laporta P., Karlsson G., Laurell F. 230-mW diode-pumped single-frequency Er:Yb laser at 1.5 µm. *IEEE Photonics Technology Letters*, 2001, no. 13, pp. 19–21. **DOI:** 10.1109/68.903207

3. Huang J., Chen Y., Wang H., Lin Y., Gong X., Luo Z., Huang Y. Efficient 1620 nm continuous-wave laser operation of Czochralski grown Er:Yb:$Lu_2Si_2O_7$ crystal. *Optics Express*, 2017, vol. 25, iss. 20, pp. 24001–24006.
DOI: 10.1364/OE.25.024001

4. Schweizer T., Jensen T., Heumann E., Huber G. Spectroscopic properties and diode-pumped 1.6 µm laser performance in Yb-codoped Er:$Y_3Al_5O_{12}$ and Er:Y_2SiO_5. *Optics communications*, 1995, vol. 118, no. 5–6, pp. 557–561. **DOI:** 10.1016/0030-4018(95)00284-F

5. Tolstik N.A., Troshin A.E., Kurilchik S.V., Kisel V.E., Kuleshov N.V., Matrosov V.N., Matrosova T.A., Kupchenko M.I. Spectroscopy, continuous-wave and Q-switched diode-pumped laser operation of Er^{3+},Yb^{3+}:YVO_4 crystal. *Appl. Phys. B*, 2007, vol. 86, no. 2, pp. 275–278.
DOI: 10.1007/s00340-006-2427-3

6. Bjurshagen S., Brynolfsson P., Pasiskevicius V., Parreu I., Pujol M.C., Peña A., Aguiló M., Díaz F.. Crystal growth, spectroscopic characterization, and eye-safe laser operation of erbium- and ytterbium-codoped $KLu(WO_4)_2$. *Applied optics*, 2008, vol. 47, no. 5, pp. 656–665. **DOI:** 10.1364/AO.47.000656

7. Chen Y., Lin Y., Huang J., Gong X., Luo Z., Huang Y. Spectroscopic and laser properties of Er^{3+},Yb^{3+}:$LuAl_3(BO_3)_4$ crystal at 1.5–1.6 µm. *Optics Express*, 2010, vol. 18, iss. 13, pp. 13700–13707.
DOI: 10.1364/OE.18.013700

8. Huang J., Chen Y., Gong X., Lin Y., Luo Z., Huang Y. Spectral and laser properties of Er:Yb:$Sr_3Lu_2(BO_3)_4$ crystal at 1.5–1.6 µm. *Optics Express*, 2013, vol. 3, iss. 11, pp. 1885–1892.
DOI: 10.1364/OME.3.001885

9. Kisel V., Gorbachenya K., Yasukevich A., Ivashko A., Kuleshov N., Maltsev V., Leonyuk N. Passively Q-switched microchip Er, Yb:$YAl_3(BO_3)_4$ diode-pumped laser. *Optics Lett*., 2012, vol. 37, no. 13, pp. 2745–2747.
DOI: 10.1364/OL.37.002745

10. Gorbachenya K.N., Deineka R.V., Kisel V.E., Yasukevich A.S., Shekhovtsov A.N., Kosmyna M.B., Kuleshov N.V. Er,Yb:$Ca_3RE_2(BO_3)_4$ (RE=Y, Gd) – novel 1.5 µm laser crystals. *Devices and Methods of Measurements*, 2019, vol. 10, no. 1, pp. 14–22.
DOI: 10.21122/2220-9506-2019-10-1-14-22

11. Gorbachenya K.N., Kisel V.E., Deineka R.V., Yasukevich A.S., Kuleshov N.V., Maltsev V.V., Mitina D.D., Volkova E.A., Leonyuk N.I. Continuous-wave Laser on Er,Yb-Codoped Pentaborate Crystal. *Devices and Methods of Measurements*, 2019, vol. 10, no. 4, pp. 271–280.
DOI: 10.21122/2220-9506-2019-10-4-301-307

12. Gorbachenya K.N., Kisel V.E., Yasukevich A.S., Maltsev V.V., Leonyuk N.I., Kuleshov N.V. Eye-safe 1.55 µm passively Q-switched Er,Yb:$GdAl_3(BO_3)_4$ diode-pumped laser. *Optics Lett*., 2016, vol. 41, no. 5, pp. 918–921. **DOI:** 10.1364/OL.41.000918

13. Gorbachenya K.N., Kisel V.E., Yasukevich A.S., Prudnikova M.B., Maltsev V.V., Leonyuk N.I., Choi S.Y., Rotermund F., Kuleshov N.V. Passively Q-switched Er,Yb:$GdAl_3(BO_3)_4$ laser with single-walled carbon nanotube based saturable absorber. *Laser Phys. Lett*., 2017, vol. 14, no. 3, p. 035802.
DOI: 10.1088/1612-202X/aa5c68

14. Gorbachenya K., Kisel V., Yasukevich A., Loiko P., Mateos X., Maltsev V., Leonyuk N., Aguiló M., Díaz F., Griebner U., Petrov V., Kuleshov N. Graphene Q-switched Er,Yb:$GdAl_3(BO_3)_4$ laser at 1550 nm. *Applied Optics*, 2017, vol. 56, no. 16, pp. 4745–4749.
DOI: 10.1364/AO.56.004745

15. Tolstik N., Sorokin E., Karhu E.A., Gorbachenya K., Polyakov S.M., Kisel V.E., Kuleshov N.V., Furtula V., Gibson U.J., Sorokina I.T. Spectral-luminescent properties of vapor deposited Cr:ZnS thin films and their application as saturable absorbers for 1.5-µm erbium lasers. *Opt. Mater. Exp*., 2018, vol. 8, no. 3, pp. 522–531.
DOI: 10.1364/OME.8.000522

16. Li C., Wyon C., Richard Moncorge. Spectroscopic properties and fluorescence dynamics of Er^{3+} and Yb^{3+} in Y_2SiO_5. *IEEE J. Quant. Electr*., 1992, vol. 28, no. 4, pp. 1209–1221. **DOI:** 10.1109/3.135248

17. Zong Y., Zhao G., Yan C., Xu X., Su L., Xu J. Growth and spectral properties of Gd_2SiO_5 crystal codoped with Er and Yb. *Journal of Crystal Growth*, 2006, vol. 294, no. 2, pp. 416–419.
DOI: 10.1016/j.jcrysgro.2006.06.019

18. Thibault F., Pelenc D., Druon F., Zaouter Y., Jaquemet M., Georges P. Efficient diode-pumped Yb^{3+}:Y_2SiO^5 and Yb^{3+}:Lu_2SiO_5 high-power femtosecond laser operation. *Opt. Lett.*, 2006, vol. 31, no. 10, pp. 1555–1557.
DOI: 10.1364/OL.31.001555

19. Du J., Liang X., Xu Y., Li R., Xu Z., Yan C., Zhao G., Su L., Xu J. Tunable and efficient diode-pumped Yb^{3+}:GYSO laser. *Optics Express*, 2006, vol. 14, iss. 8, pp. 3333–3338. **DOI:** 10.1364/OE.14.003333

20. Burns P.A., Dawes J.M., Dekker P., Piper J.A., Jiang H., Wang J. Optimization of Er,Yb:YCOB for CW laser operation. *IEEE J. Quant. Electr.*, 2004, vol. 40, no. 11, pp. 1575–1582. **DOI:** 10.1109/JQE.2004.834935

21. Yasyukevich A.S., Shcherbitskii V.G., Kisel V.E., Mandrik A.V., Kuleshov N.V. Integral method of reciprocity in the spectroscopy of laser crystals with impurity centers. *Journal of Applied Spectroscopy*, 2004, vol. 71, no. 2, pp. 202–208.
DOI: 10.1023/B:JAPS.0000032875.04400.a0

Compact Passively Q-Switched Tm:KY$(WO_4)_2$ Laser

V.E. Kisel

Center for Optical Materials and Technologies,
Belarusian National Technical University,
Nezavisimosty Ave., 65, Minsk 220013, Belarus

Received 28.01.2022
Accepted for publication 02.03.2022

Abstract

Diode-pumped thulium lasers emitting in the spectral range near 2 µm are attractive for applications in different areas: surgery, rangefinding, and environmental atmosphere monitoring. In this article the latest results of Tm:KYW laser performance with a polycrystalline Cr:ZnSe as the most available saturable absorber for 2 µm spectral region are presented.

A maximum continuous-wave output power of ≈ 0.65 W with a slope efficiency of 55 % was obtained at the wavelength of 1940 nm. Laser pulses with energy of 26 µJ and repetiotion rate of 6 kHz coresponding to 156 mW of average output power at 1910 nm were obtained at 2.2 W of incident puwp power for the Cr:ZnSe saturable absorber with initial transmission of 95 %. By using of saturable absorber with lower initial transmission of 90 % laser pulses with energy of 40 µJ and duration as short as 10 ns were realized. The maximal pulse repetition rate was 2.8 kHz at incident pump power of 2.2 W.

Based on the obtained results, it can be concluded that Tm:KYW crystals are promising active media for the compact passively *Q*-switched lasers emitting in the spectral range near 2 µm for the usage in surgery and rangefinding. Also, described laser is planned to be used as a laser source in laser-induced damage threshold measurements setup for investigation of damage threshold of saturable absorbers as well as nonlinear crystals at the wavelength near 2 µm.

Keywords: thulium, potassium-yttrium tungstate crystal, passively *Q*-switching mode, spectral range near 2 µm.

DOI: 10.21122/2220-9506-2022-13-1-27-31

Адрес для переписки:
Кисель В.Э.
Центр оптических материалов и технологий,
Белорусский национальный технический университет,
пр-т Независимости, 65, г. Минск 220013, Беларусь
e-mail:vekisel@bntu.by

Address for correspondence:
Kisel V.E.
Center for Optical Materials and Technologies,
Belarusian National Technical University,
Nezavisimosty Ave., 65, Minsk 220013, Belarus
e-mail: vekisel@bntu.by

Для цитирования:
V.E. Kisel.
Compact Passively Q-Switched Tm:KY$(WO_4)_2$ Laser.
Приборы и методы измерений.
2022. – Т. 13, № 1. – С. 27–31.
DOI: 10.21122/2220-9506-2022-13-1-27-31

For citation:
V.E. Kisel.
Compact Passively Q-Switched Tm:KY$(WO_4)_2$ Laser.
Devices and Methods of Measurements.
2022, vol. 13, no. 1, pp. 27–31.
DOI: 10.21122/2220-9506-2022-13-1-27-31

Компактный лазер на основе кристалла $Tm:KY(WO_4)_2$, работающий в режиме пассивной модуляции добротности

В.Э. Кисель

Центр оптических материалов и технологий,
Белорусский национальный технический университет,
пр-т Независимости, 65, г. Минск 220013, Беларусь

Поступила 28.01.2022
Принята к печати 02.03.2022

Тулиевые лазеры с диодной накачкой, работающие в спектральной области около 2 мкм, находят широкое применение в различных областях, таких как хирургия, дальнометрия и дистанционное зондирование атмосферы. В статье продемонстрирован макет твердотельного Tm:KYW лазера, работающий в режиме пассивной модуляции добротности с насыщающимся поглотителем на основе поликристаллического Cr:ZnSe, синтезированного методом химического газофазного осаждения.

Максимальная выходная мощность лазера в непрерывном режиме генерации достигала ≈ 0,65 Вт на длине волны 1940 нм при дифференциальной эффективности по поглощённой мощности накачки 55 %. В режиме пассивной модуляции добротности при использовании насыщающегося поглотителя Cr:ZnSe с начальным пропусканием 95 % энергия лазерных импульсов составила 26 мкДж, максимальная частота следования импульсов достигала 6 кГц при падающей мощности накачки 2.2 Вт. При использовании насыщающегося поглотителя с начальным пропусканием 90 % энергия лазерных импульсов достигала 40 мкДж, длительность импульсов не превышала 10 нс.

На основе полученных результатов можно сделать вывод, что данные кристаллы являются перспективными активными средами для лазеров, излучающих в спектральном диапазоне около 2 мкм, для применения в составе хирургических систем и систем лазерной дальнометрии. Предполагается использование разработанного макета лазера в составе комплекса по измерению порог оптического разрушения насыщающихся поглотителей и нелинейных кристаллов в области 2 мкм.

Ключевые слова: лазер, тулий, кристалл калий-иттриевого вольфрамата, режим пассивной модуляции добротности, спектральная область около 2 мкм.

DOI: 10.21122/2220-9506-2022-13-1-27-31

Адрес для переписки:
Кисель В.Э.
Центр оптических материалов и технологий,
Белорусский национальный технический университет,
пр-т Независимости, 65, г. Минск 220013, Беларусь
e-mail:vekisel@bntu.by

Address for correspondence:
Kisel V.E.
Center for Optical Materials and Technologies,
Belarusian National Technical University,
Nezavisimosty Ave., 65, Minsk 220013, Belarus
e-mail: vekisel@bntu.by

Для цитирования:
V.E. Kisel.
Compact Passively Q-Switched $Tm:KY(WO_4)_2$ Laser.
Приборы и методы измерений.
2022. – Т. 13, № 1. – С. 27–31.
DOI: 10.21122/2220-9506-2022-13-1-27-31

For citation:
V.E. Kisel.
Compact Passively Q-Switched $Tm:KY(WO_4)_2$ Laser.
Devices and Methods of Measurements.
2022, vol. 13, no. 1, pp. 27–31.
DOI: 10.21122/2220-9506-2022-13-1-27-31

Introduction

Diode-pumped thulium lasers operating in the spectral range near 2 µm are attractive for applications in different areas: surgery, since their radiation is strongly absorbed by water, rangefinding, and environmental atmosphere monitoring due to the presence of absorption lines of a number of chemical compounds (benzol, ethanol, etc.) in the spectral region around 2 µm [1].

Interest in thulium-doped crystals is explained by the availability of powerful AlGaAs diode pump sources emitting at near 800 nm and cross-relaxation process $^3H_6 + ^3H_4 \rightarrow ^3F_4 + ^3F_4$ leading to efficient excitation of $^3F_4$ laser level thus increase the quantum efficiency of the systems. Monoclinic potassium double tungstate crystals activated with thulium ions Tm:KY$(WO_4)_2$ (Tm:KYW) attract attention due to relatively high absorption and emission cross-section, broad emission bands, and the possibility to grow highly activated crystals [2]. The great potential of Tm:KYW laser crystal has been already demonstrated in continuous-wave [3], mode-locking [4] and *Q*-switch [5] regimes of operation.

Up today, many saturable absorbers (SA) based on nanomaterials and crystalline media have been proposed for realization of passive *Q*-switching. Passively *Q*-switched Tm:KYW lasers have been already demonstrated with Cr:ZnS with following characteristics of pulses: 57 ns, 3 µJ, 25 kHz, with Cr:ZnSe: 60 ns, 19 µJ, 5.6 kHz, and with PbS: 8 ns, 30 µJ, 4.2 kHz [5–7].

Here we report on the latest results of Tm:KYW laser performance with a polycrystalline chemical vapor deposited Cr:ZnSe as the most available saturable absorber for 2 µm spectral region.

Experimental laser setup and results

The experimental laser setup is presented in the Figure 1. The near hemispherical laser cavity consisted of a curved output coupler (OC) and a plane high reflector was used. The cavity length was about 24 mm. A laser crystal was N_g-cut Tm(3%):KYW with the thickness of 2.8 mm and antireflection coatings on it's working sides. The temperature of active element (AE) was kept at 14 °C by means of copper slab and thermoelectrical cooling of the elements with a water-cooled heatsink. A 3-W continuous-wave fiber-coupled diode laser (λ = 802 nm, Ø = 100 µm, N.A. = 0.15) was used for a longitudinal pumping of the active element. A pump beam was focused into a 200 µm spot inside the laser crystal. The cavity length was adjusted to get TEM$_{00}$ transversal mode diameter at the active element close to the pump beam waist considering induced thermal lensing effects. A set of output couplers with different transmissions (T_{oc}) was used during continuous-wave laser experiments.

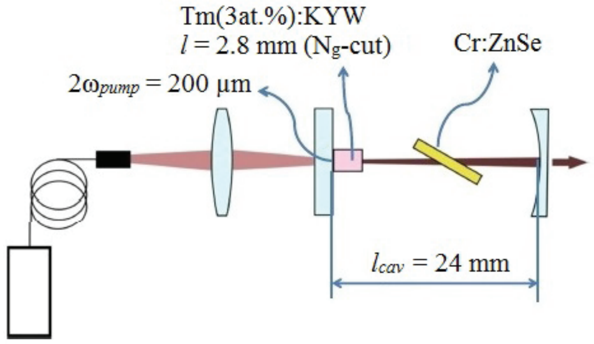

Figure 1 – Experimental laser setup

Initially, laser experiments were carried out in the continuous-wave regime of opeartion. The maximum output power of 645 mW at 1940 nm was measured with an output coupler transmission of 3 %. A slope efficiency (η) of 55 % with respect to the absorbed pump power was obtained. Laser emission was linearly polarized along N_m axis. Input-output diagrams for the CW Tm:KYW laser are shown in the Figure 2.

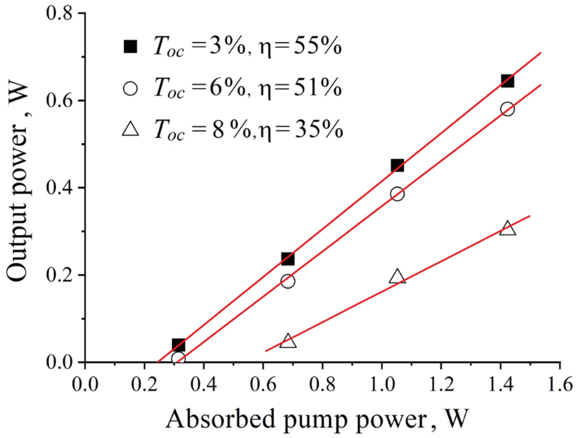

Figure 2 – Input-output diagrams of the continuous-wave Tm:KYW laser

The *Q*-switch laser experiments were performed taking into account comparatively low light induced damage threshold of the Cr^{3+}:ZnSe saturable absorbers (≈ 2.5 J/cm^2). The saturable absorber was inserted into the cavity between active medium and OC at Brewster angle. Two SAs with initial transmissions of 95 % and 90 % were used.

Laser pulses with energy of about 26 μJ and repetiotion rate of 6 kHz coresponding to 156 mW of average output power at 1910 nm were obtained at 2.2 W of incident puwp power for the SA with the initial transmission of 95 % nm and OC with transmission of 6 %. With the increase of incident pump power from the threshold to its maximal value the pulse energy and repetition rate varied from 20 to 26 μJ and 0.2 to 6 kHz, respectively. The dependence of pulse duration and repetition rate on incident pump power is shown in the Figure 3. The increase of pulse enegy with incident pump power can be explained by changing in the TEM_{00} mode size due to thermal effects in the gain medium. The spatial profile of the output beam was TEM_{00} mode with $M^2 < 1.2$ at maximal incident pum power (inset in the Figure 3).

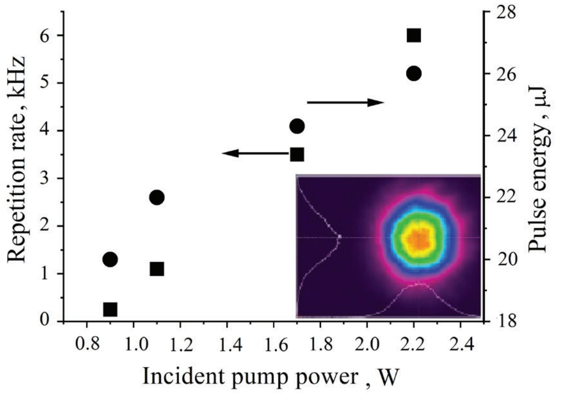

Figure 3 – Dependence of laser pulse characteristics on incident pump power for saturable absorber with initial transmission of 95 %

The shortest laser pulse duration was measured to be 14 ns. The oscilloscope traces of single pulse with the duration of 14 ns and output pulse train with maximal repetition rate of 6 kHz are presented in the Figure 4. It should be mentioned that maximum pulse repetition rate was limited by the laser-induced damage threshold of the SA.

The dependence of laser pulse characteristics on incident pump power for saturable absorber with initial transmission of 90 % is presented in the Figure 5.

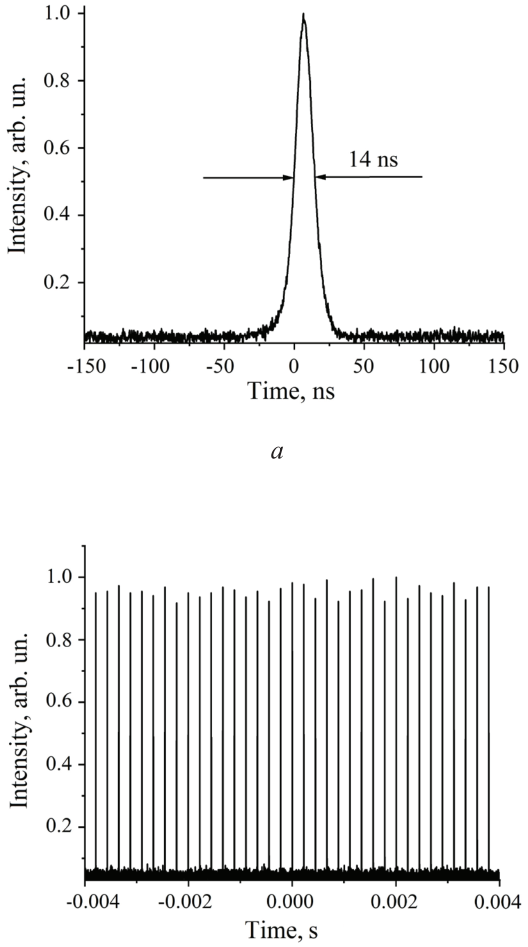

b

Figure 4 – Oscilloscope traces: *a* – single pulse with the duration of 14 ns; *b* – output pulse train maximal repetition rate of 6 kHz

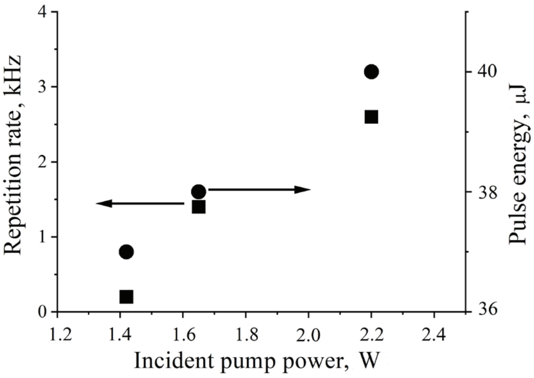

Figure 5 – Dependence of laser pulse characteristics on incident pump power for saturable absorber with initial transmission of 90 %

The laser wavelength shifts to 1940 nm that can be caused by a higher SA losses at shorter wavelength. Laser pulses with energy up to 40 μJ and duration as short as 10 ns were obtained in this case. The maximal repetition rate was 2.8 kHz at incident pump power of 2.2 W.

Conclusion

In conclusion, compact Tm:KY$(WO_4)_2$ laser was demonstrated. A maximum CW output power of about 0.65 W with a slope efficiency of 55 % was obtained at the wavelength of 1940 nm. In a passively *Q*-switched regime of operation laser pulses with energy of 40 μJ and duration of 10 ns were obtained at a repetition rate of 2.8 kHz at the incident pump power of 2.2 W.

Based on the obtained results, it can be concluded that Tm:KYW crystals are promising active media for lasers emitting in the spectral range near 2 μm for the usage in surgery and rangefinding. Also, described laser is planned to be used as a seed pulses source for future amplification and applying in laser induced damage threshold measurements setup for investigation of optical damage threshold of saturable absorbers as well as nonlinear crystals at the wavelength near 2 μm.

Acknowledgments

The author thanks Dr. K.N. Gorbachenya and A.I. Lazartschuk for the help with the carrying out of laser experiments. This research was partially supported by BRFFR F21RM-129.

References

1. Scholle K., Lamrini S., Kookmann P., Fuhrberg P. 2μ laser sources and their possible applications. *Frontiers in Guided Wave Optics and Optoelectronics*. *IntechOpen*, 2010. **DOI:** 10.5772/39538

2. Guretskii S.A., Trukhanova E.L., Kravtsov A.V., Gusakova N.V., Gorbachenya K.N., Kisel V.E., Yasukevich A.S., Lisiecki R., Lukowiak A., Karpinsky D.V., Ozen Y., Ozcelik S. Tm^{3+}:KY$(WO_4)_2$ single crystals: controlled growth and spectroscopic assessment. *Optical Materials*, 2021, vol. 120, p. 111451.

3. Gaponenko M., Kuleshov N., Sudmeyer T. Efficient diode-pumped Tm:KYW 1.9-μm microchip laser with 1 W CW output power. *Opt. Express*, 2014, vol. 22, pp. 11578–11582. **DOI:** 10.1364/OE.22.011578

4. Lagatsky A.A., Calvez S., Gupta J.A., Kisel V.E., Kuleshov N.V., Brown C.T.A., Dawson M.D., Sibbett W., Broadly tunable femtosecond mode-locking in a Tm:KYW laser near 2 μm. *Opt. Express*, 2011, vol. 19, pp. 9995–10000. **DOI:** 10.1364/OE.19.009995

5. Gaponenko M.S., Onushchenko A.A., Kisel V.E., Malyarevich A.M., Yumashev K.V., Kuleshov N.V. Compact passively Q-switched diode-pumped Tm:KY$(WO_4)_2$ laser with 8 ns/30 μJ pulses. *Laser Phys. Lett.*, 2012, vol. 9, pp. 291–294. **DOI:** 10.1002/lapl.201110128

6. Batay L., Kuzmin A., Grabtchikov A., Lisinetskii V., Orlovich V., Demidovich A., Titov A., Badikov V., Sheina S., Panyutin V., Mond M., Kuck S. Efficient diode-pumped passively Q-switched laser operation around 1.9 μm and selffrequency Raman conversion of Tm-doped KY$(WO_4)_2$. *Appl. Phys. Lett.*, 2002, vol. 81, pp. 2926–2936. **DOI:** 10.1063/1.1514393

7. Gaponenko M., Troshin A., Malyarevich A., Kisel V., Kuleshov N., Yumashev K., Onushchehko A., Zhilin A., Levchenk V. Passive Q-switching of diode-pumped Tm:KY$(WO_4)_2$ laser with PbS-doped glass and Cr:ZnSe crystal. International Conference on Lasers, Applications and Technologies 2007: Advanced Lasers and Systems, vol. 6731, 67310T. **DOI:** 10.1117/12.752636

Determination of ^{238}U Content by Gamma Radiation Emitting from ^{234m}Pa Radionuclide

Arkadiy Khruschinski[1], Semen Kutsen[1], Alex Zhukouski[2,3], Naoyuki Sugai[4], Hiroshi Sugai[4], Michinori Mogi[4]

[1]*Institute for Nuclear Problems of Belarusian State University,*
Bobruiskaya str., 11, Minsk 220006, Belarus

[2]*International Sakharov Environmental Institute of Belarusian State University,*
Dolgobrodskaya str., 23/1, Minsk 220070, Belarus

[3]*Scientific and Production Enterprise "ATOMTEX", Gikalo str., 5, Minsk 220005, Belarus*

[4]*Rad Solutions Co., Ltd. 1-2-38, Kashiwagi, Aobaku, Sendai, Miyagi, Japan*

Received 03.02.2022
Accepted for publication 15.03.2022

Abstract

Radionuclide ^{238}U is one of the most important radioactive elements that must be controlled in nuclear power engineering, geological exploration, control of radioactive contamination of soils and raw materials used in construction. The most optimal way to control ^{238}U is to use the ^{234m}Pa radionuclide, the activity of which, due to its short lifetime (≈ 1.2 min), is unambiguously related to the activity of ^{238}U even if the secular equilibrium is disturbed in the sample under study

Possibility of use of the ^{234m}Pa nuclide gamma radiation to determine ^{238}U with a scintillation detector in a medium containing natural radionuclides is investigated and demonstrated using the simplest examples. The proposed algorithm for determining of the ^{238}U content is based on the Monte Carlo simulation of the detector response to the radiation of the ^{234m}Pa radionuclide at its 1001 keV energy line and subsequent processing of the experimental spectrum, including the Wiener filtering of the signal. This method makes it possible to determine the content of ^{238}U in a continuous homogeneous medium while presence of natural radionuclides in it.

The algorithm for determining of ^{238}U content includes several main steps. Filtering based on the Wiener algorithm allows selecting a slowly changing part of the spectrum. Results of Monte Carlo simulations make it possible to determine the detection efficiency in a limited informative region of the spectrum, which includes, along with the 1001 keV peak from the ^{234m}Pa nuclide, which is a decay product of the radionuclide ^{234}Th, and the peak of an interfering radionuclide from the decay chain of ^{232}Th. This part of the spectrum does not contain any other lines of gamma radiation from natural radionuclides – decay products of both thorium and uranium chains. These two peaks in the spectral region under study can be separated from each other in a medium with a typical concentration of ^{234}Th.

Analysis of results of the activity of depleted uranium metal measuring in accordance with the proposed algorithm shows the possibility of determining of ^{238}U content with an uncertainty of 3–5 %.

Keywords: radionuclide ^{234m}Pa, Monte-Carlo simulation, experimental spectrum processing algorithm, depleted metallic uranium.

DOI: 10.21122/2220-9506-2022-13-1-32-39

Адрес для переписки:
Жуковский А.
УП « АТОМТЕХ»,
ул. Гикало, 5, г. Минск 220005, Беларусь
e-mail: alexzhukovski@gmail.com

Address for correspondence:
Zhukouski Alex
SPE "ATOMTEX",
Gikalo str., 5, Minsk 220005, Belarus
e-mail: alexzhukovski@gmail.com

Для цитирования:
Arkadiy Khruschinski, Semen Kutsen, Alex Zhukouski, Naoyuki Sugai, Hiroshi Sugai, Michinori Mogi.
Determination of ^{238}U Content by Gamma Radiation
Emitting from ^{234m}Pa Radionuclide.
Приборы и методы измерений.
2022. – Т. 13, № 1. – С. 32–39.
DOI: 10.21122/2220-9506-2022-13-1-32-39

For citation:
Arkadiy Khruschinski, Semen Kutsen, Alex Zhukouski, Naoyuki Sugai, Hiroshi Sugai, Michinori Mogi.
Determination of ^{238}U Content by Gamma Radiation
Emitting from ^{234m}Pa Radionuclide.
Devices and Methods of Measurements.
2022, vol. 13, no. 1, pp. 32–39.
DOI: 10.21122/2220-9506-2022-13-1-32-39

Определение содержания ^{238}U по гамма-излучению ^{234m}Pa

Аркадий Хрущинский[1], Семен Кутень[1], Александр Жуковский[2, 3], Наоюки Шугай[4], Хироши Шугай[4], Мичинори Моги[4]

[1]Институт ядерных проблем Белорусского государственного университета,
ул. Бобруйская, 11, г. Минск 220006, Беларусь

[2]Международный государственный экологический институт имени А.Д. Сахарова
Белорусского государственного университета,
ул. Долгобродская, 23/1, г. Минск 220070, Беларусь

[3]Научно-производственное унитарное предприятие «АТОМТЕХ»,
ул. Гикало, 5, г. Минск 220005, Беларусь

[4]Rad Solutions Co., Ltd. 1-2-38, Кашиваги, Аобаку, Сендай, Япония

Поступила 03.02.2022
Принята к печати 15.03.2022

В атомной энергетике, в геологоразведке, при контроле радиоактивного загрязнения почв и сырья, используемого при строительстве, одним из важнейших радиоактивных элементов, который необходимо контролировать, является ^{238}U. Наиболее оптимально для контроля ^{238}U использовать радионуклид ^{234m}Pa, активность которого из-за малости времени его жизни (≈ 1,2 мин) однозначно связана с активностью ^{238}U даже при условии нарушения векового равновесия в исследуемом образце.

Исследована и продемонстрирована на простейших примерах возможность использования гамма-излучения нуклида ^{234m}Pa для определения ^{238}U с помощью сцинтилляционного детектора в среде, содержащей естественные радионуклиды. Предложенный алгоритм определения содержания ^{238}U основан на моделировании методом Монте-Карло отклика детектора на излучение радионуклида ^{234m}Pa на его монолинии 1001 кэВ и последующей обработке экспериментального спектра прибора, включающей винеровскую фильтрацию сигнала. Этот способ позволяет определить содержание ^{238}U в сплошной однородной среде при наличии в ней естественных радионуклидов.

Алгоритм определения содержания радионуклида включает в себя несколько основных этапов. Фильтрация на основе алгоритма Винера позволяет выделить медленно меняющуюся часть спектра. Результаты Монте-Карло моделирования дают возможность определить эффективность регистрации в ограниченном информативном участке спектра, включающем наряду с пиком 1001 кэВ от нуклида ^{234m}Pa, являющегося продуктом распада радионуклида ^{234}Th, и ближайший к нему пик мешающего радионуклида из цепочки распада ^{232}Th. Этот участок спектра по определению не содержит никаких других линии гамма-излучения от естественных радионуклидов – продуктов распада как ториевой, так и урановых цепочек. Указанные два пика на исследуемом участке спектра могут быть отделены друг от друга в среде с типичной концентрацией ^{234}Th.

Анализ результатов измерения активности обеднённого металлического урана в соответствии с предложенным алгоритмом показывает возможность определения содержания ^{238}U с погрешностью 3–5 %.

Ключевые слова: радионуклид ^{234m}Pa, моделирование методом Монте-Карло, алгоритм обработки экспериментального спектра, обеднённый металлический уран.

DOI: 10.21122/2220-9506-2022-13-1-32-39

Адрес для переписки:
Жуковский А.
УП « АТОМТЕХ»,
ул. Гикало, 5, г. Минск 220005, Беларусь
e-mail: alexzhukovski@gmail.com

Address for correspondence:
Zhukouski Alex
SPE “ATOMTEX”,
Gikalo str., 5, Minsk 220005, Belarus
e-mail: alexzhukovski@gmail.com

Для цитирования:
Arkadiy Khruschinski, Semen Kutsen, Alex Zhukouski, Naoyuki Sugai, Hiroshi Sugai, Michinori Mogi.
Determination of ^{238}U Content by Gamma Radiation
Emitting from ^{234m}Pa Radionuclide.
Приборы и методы измерений.
2022. – Т. 13, № 1. – С. 32–39.
DOI: 10.21122/2220-9506-2022-13-1-32-39

For citation:
Arkadiy Khruschinski, Semen Kutsen, Alex Zhukouski, Naoyuki Sugai, Hiroshi Sugai, Michinori Mogi.
Determination of ^{238}U Content by Gamma Radiation
Emitting from ^{234m}Pa Radionuclide.
Devices and Methods of Measurements.
2022, vol. 13, no. 1, pp. 32–39.
DOI: 10.21122/2220-9506-2022-13-1-32-39

Introduction

In nuclear power engineering, in geological exploration, in the control of radioactive contamination of soils, one of the most important radioactive elements, the concentration of which has to be determined, is the isotope ^{238}U. A common method for determining of the ^{238}U content in such media is the use of scintillation or germanium detectors which measure the gamma activity of one or several daughter nuclides in selected representative samples [1–3]. The media to be investigated contain radioactive nuclides of various origins. Soils contain not only nuclides that are the decay product of ^{238}U, but also nuclides that have got into this soil area from other areas due to various transfer processes. The fallout of radioactive dust and the subsequent migration of radionuclides will also disrupt any connection between these nuclides and ^{238}U in the soil, although they are decay products in its chain. The same inconsistency can occur in ores and various other materials. Only one nuclide ^{234m}Pa will be uniquely associated with ^{238}U contained in the mentioned media, since its lifetime is ≈ 1.2 min, so the transfer processes can be neglected [2].

The proposed technique can also be used for the case when for the identification of a nuclide and the determination of its content several gamma lines are used. In this case the procedure described below is applied independently for each such line.

Materials and methods

Relationship between ^{238}U and ^{234m}Pa activities

To determine of ^{238}U amount in a medium at ^{234m}Pa, it is first of all necessary to relate the amount of uranium to the amount of ^{234m}Pa. For this, it is necessary to use the uranium decay scheme (Figure 1) [4].

From the diagram a system of equations describing the time evolution of nuclides of interest in this problem can be used:

$$\frac{dN_u}{dt} = -\lambda_u N_u;$$
$$\frac{dN_T}{dt} = \lambda_u N_u - \lambda_T N_T;$$
$$\frac{dN_p}{dt} = \lambda_T N_T - \lambda_p N_p,$$

where N_U, N_T, N_P – the number of uranium, thorium and protactinium nuclei, respectively; λ_U, λ_T, λ_P are decay constants.

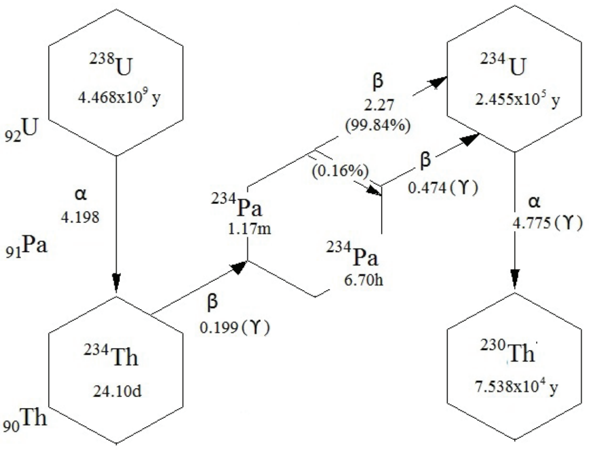

Figure 1 – Part of the ^{238}U decay scheme

These equations are easily integrated by the varying constants method and the solution for the relationship between the number of protactinium and uranium atoms is given by the equation:

$$N_p = \lambda_T \frac{\lambda_u N_0}{\lambda_T - \lambda_u} \left(\frac{e^{(-\lambda_u)t}}{(\lambda_p - \lambda_u)} - \frac{e^{(-\lambda_T)t}}{(\lambda_p - \lambda_T)} \right) =$$

$$= \lambda_T \frac{\lambda_u N_0}{\lambda_T - \lambda_u} \left(\frac{1}{(\lambda_p - \lambda_u)} - \frac{e^{-\lambda_T t}}{(\lambda_p - \lambda_T)} \right).$$

Taking into account that $\lambda_P >> \lambda_T >> \lambda_U$, and the lifetime of uranium is longer than the lifetime of thorium, we have:

$$N_p = \frac{\lambda_u N_0}{\lambda_p}; \quad N_u = \frac{T_u}{T_p} N_p.$$

It can be seen from the above relations that the relationship between the number of atoms of two nuclides does not depend on the time and concentration of other nuclides included in the ^{238}U decay chain, regardless of their origin in the medium.

Before processing the experimental results, it is necessary to simulate the measurement process and determine the main parameter of this method: $S_{0\gamma}$, it is the area under the Full Absorption Peak (FAP) of the gamma-radiation line, normalized to the one played gamma quantum. It should be noted that this parameter does not relate to a specific activity; it characterizes the average response to one played photon. Calculating the same value for the experiment, reduced to a unit of volume (mass) and time, we obtain from their ratio the number of protactinium atoms that underwent decay through a given channel per unit of time and per unit of volume (n). Taking into account other decays, the total number of decayed protactinium atoms per unit volume and per unit time is $N_d = n/\eta$, η is the fraction of gamma decays of protactinium with $E_\gamma = 1.001$ MeV. Further, the reduction of the number of ^{238}U atoms is carried out according to the above formulas of the described decay kinetics.

For the algorithm to work correctly, it is necessary that the same hardware functions that characterize the Analog-to-Digital Converter of the equipment are used in both the simulation and the processing of the experiment. In our case, these are: the channel – energy dependence and the dependence of the line width on the energy of the registered gamma radiation.

Monte Carlo simulation

The purpose of the first stage of the proposed algorithm is to simulate the process of measuring and calculating the amplitude distribution of pulses of each radionuclide using the Monte Carlo method and determining $S_{0\gamma}$ [5].

The developed model of the detecting device (DD) used in the experiment in the measurement geometry of metallic uranium at a distance of 10 cm from the DD surface opposite the geometric center of the scintillation crystal is shown in Figure 2.

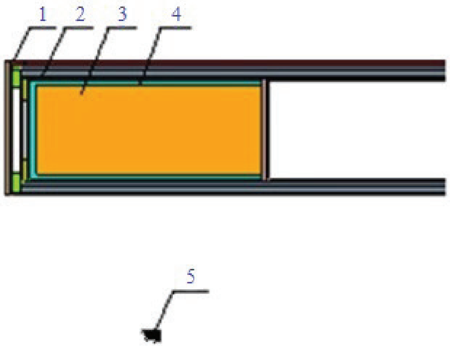

Figure 2 – The detecting device and source (metallic ^{238}U) used in Monte Carlo simulations: 1 – case of the detection device; 2 – probe; 3 – NaI(Tl) scintillation crystal; 4 – MgO reflector; 5 – source – metal ^{238}U (1/4 cylindrical column)

In Monte Carlo simulations, it is possible to take into account the energy dependence of the line width on the energy of the recorded radiation of a real spectrometer. To account for this dependence on energy E, the MCNP program uses a special formula for the energy dependence of the full line width at half maximum (*fwhm*):

$$fwhm_{mcnp}(E) = a + b\sqrt{E + c * E \wedge 2}, \tag{1}$$

where the coefficients a, b, c should be determined from the experimental data for a given detector by approximating them using formula (1). The coefficients $\{a, b, c\} = \{-0.00819936,\ \ 0.0704576,\ \ -0.0154056\}$ obtained as a result of approximating the experimental data for the NaI(Tl) detector with dimensions Ø63×160 mm. This *fwhm* were used to calculate the pulses height spectrum in the MCNP program.

The DD model was verified by comparing the theoretical and experimental spectra from a coin source with ^{137}Cs with known activity, placed at a distance of 10 cm from the lateral surface. The difference in the heights of the FAP line of gamma radiation with an energy of 0.662 MeV did not exceed 3 %.

As indicated earlier, the most representative ^{238}U radionuclide is ^{234m}Pa, and its preferred gamma-emitting line in terms of quantum efficiency is 1.001 MeV. Figure 3 shows the simulated pulses height spectrum of metallic ^{238}U (main picture). The result of Monte Carlo simulation of only ^{234m}Pa gamma radiation with an energy of 1.001 MeV and its *Math-background* (envelope of the slowly changing part of FAPs calculated by second-order polynomials [4]) are shown in small picture.

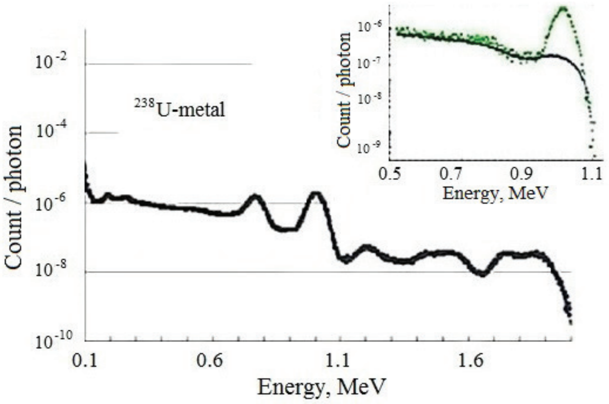

Figure 3 – The simulated pulses height spectra of metallic ^{238}U (main picture) and the result of Monte Carlo simulation of gamma radiation with energy of 1.001 MeV with its *Math-background* (insert)

It is find the difference between the model spectrum smoothed by the Wiener filter [5] and its *Math-background* in the energy region from 0.85 to 1.05 MeV. The resulting value is approximated by a Gaussian distribution and the area under this curve ($S_{0\gamma}$) is found, which in MCNP is automatically normalized to the total number of played stories. For the model of this experiment, $S_{0\gamma i} = 0.00001773$.

The Wiener filter is the optimal filter for the formation of the output signal $z(t)$ from the input signal $x(t)$ with the known form of the useful signal $s(t)$, which is contained in the input signal in the amount of noise. As a criterion for its optimization, the standard deviation of the signal $y(t)$ at the filter output from the given waveform $z(t)$ is used. In this case, such a signal was the sum of a slowly changing background and Gaussian peaks [6, 7].

Algorithm for determining the content of radionuclide in the object of measurement

Experimental spectrum processing primarily includes background spectrum subtraction, Wiener filtering, *Math-background* determination and subtraction. The processing block diagram is shown in Figure 4.

To understand the operation of the algorithm, an experiment was carried out in which a portable scintillation spectrometer was used, the Monte Carlo model of which is presented above.

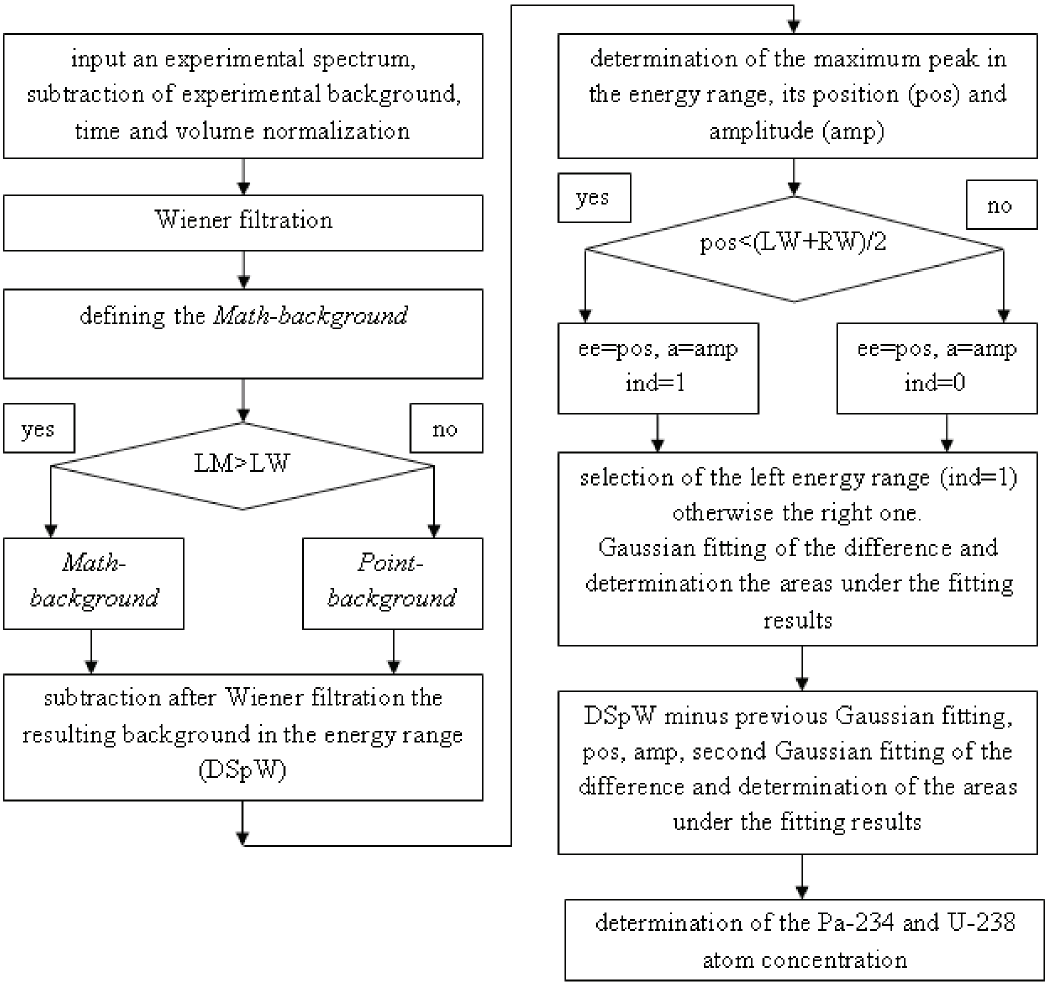

Figure 4 – Block diagram of the algorithm: LM – position of the left minimum of Math-background; LW – left border of the window; RW – right. DSpW is normalized spectrum minus Math-background in the energy range. Point-background is a smooth curve passing through the minima of the spectrum transformed by Wiener filtering

Experimental research

To test the proposed algorithm, an experiment was carried out using a DD based on a NaI(Tl) scintillation crystal with dimensions of Ø63 × 160 mm and a small volumetric cylindrical source of metallic ^{238}U (depleted metallic uranium) located at a distance of 10 cm (Figure 5).

The source with a density of 19.8 g/cm^3 consists of: 0.0023 % of ^{234}U with an activity of 10894 Bq/sample; 0.4054 % of ^{235}U with 667 Bq/sample and 99.5923 % of ^{238}U with 25485 Bq/sample. Figure 6 shows the experimental Gross spectrum measured over a time of 7200 s in the measurement geometry according to Figure 5, the background spectrum BKG and the difference between the experimental and background spectrum – the experimental pulses height spectrum Net.

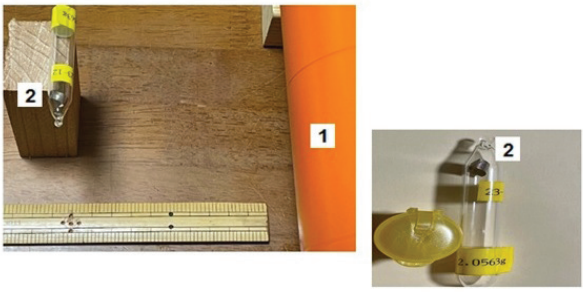

Figure 5 – Geometry of experiment with depleted metallic uranium source: 1 – the detection device; 2 – depleted metallic uranium source

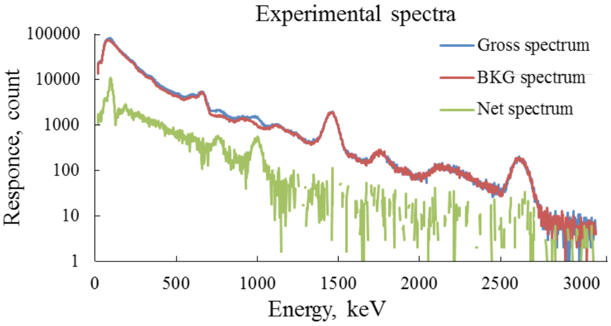

Figure 6 – The experimental spectra

The experimental pulses height spectrum Net was obtained by channel-by-channel subtraction of the background spectrum from the experimental one, measured when the source was located opposite to the annular mark applied to the lateral surface of the DD, which corresponds to the geometric center of the NaI(Tl) crystal.

Approbation of the algorithm on the example of the experimental spectrum of metallic ^{238}U

Approbation of the algorithm is presented using the example of processing the experimental Gross spectrum. The step of subtracting the background spectrum is excluded from the algorithm due to its insignificant contribution to the result of calculating the activity in this case. According to the algorithm, the experimental Gross spectrum was transformed into the pulses height spectrum using filtering according to the Wiener algorithm.

The most important step in this algorithm is the definition and subtraction of *Math-background*. The algorithm provides two variants:

1. Using an algorithm from the Wolfram Mathematica [8]. In the work we use the “EstimatedBackground” function without a parameter from “Mathematics”, which allows to build a smoothly varying function passing through the minimums of the spectrum (see Figure 7).

2. Draw a curve passing through the background minima, determined by the algorithm from the Wolfram Mathematica. Often the minima of this background are located farther in energy than the gamma-radiation line of interest, and then the first option is used.

It is shown in Figure 7 the pulses height spectrum after Wiener filter and *Math-background* according to the algorithm from the Wolfram Mathematica. Since the left minimum of this background lies to the right of the line (1.001 MeV), the first variant is chosen.

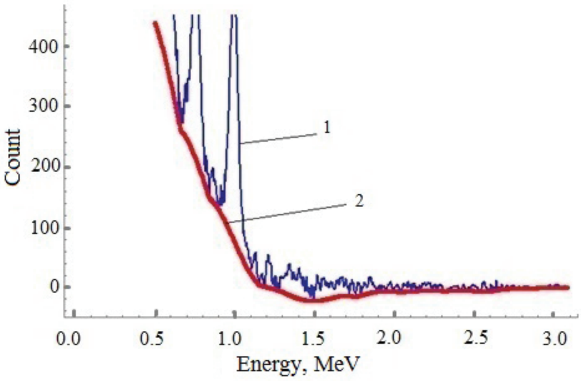

Figure 7 – Transformed pulses height spectrum according to the Wiener algorithm (1) and Math-background (2) (the first variant of the estimation)

Further consideration will be carried out only in the energy region from 0.85 to 1.05 MeV where is situated the protactinium’s FAP with energy $E = 1.001$ MeV. The region is not quite symmetrical about this line (1.001 MeV), the center of the window is shifted to the left. The ^{234m}Pa peak on a spectrum is shifted to the left due to the presence of Compton scattering of gamma quantum from high-energy photons. In the analysis, the initial region is split by the midpoint into two windows, left and right one. If the main maximum of the region is in the left window, it means that the ^{232}Th peak is prevails. The Gaussian approximation of this peak is carried out, the difference between the experimental spectrum and the obtained approximation in the full region is determined. Then the contribution of Pa and its peak and the Gaussian approximation of the latter are found by the points of this difference. This approach allows you to separate these peaks, even if they overlap significantly. If the main maximum in the full window is in the left part of the window, processing is starting from the right part, and then the mentioned nuclides are swapped. Now Gaussian fitting of the protactinium peak is performed, subtraction of the fitting result from the experimental spectrum and approximation of the Gaussian difference for the ^{232}Th peak.

The result of this processing is illustrated in Figure 8. In this case, the main maximum is in the right half of the energy window and corresponds to the contribution of ^{234m}Pa (the Gaussian approximation of this peak is curve 1), in the left half of the window is the thorium peak, curve 2 obtained after approximating the difference between the experimental curve and the curves 1.

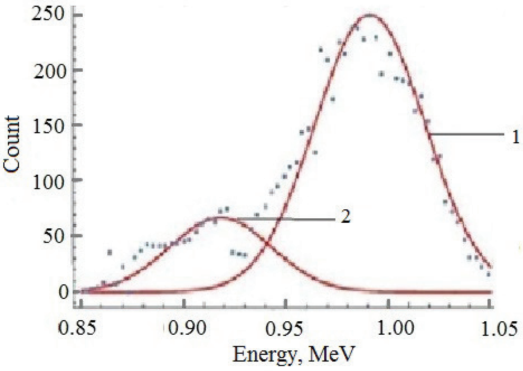

Figure 8 – Counting in the energy window of the useful signal minus background (points), curve 1 is Gaussian approximation of ^{234m}Pa peak, curve 2 is Gaussian approximation of ^{232}Th peak

Next, the area under the Gaussian approximation of ^{234m}Pa with an energy of 1.001 MeV ($S_{1\gamma}$) is determined. Then the ratio $S_{1\gamma}/S_{0\gamma i}$ determines the number of ^{234m}Pa nuclei decayed in a source of volume V during the experiment time t.

Reduced to a unit of time and volume, the number of decayed ^{234m}Pa atoms is given by the equation:

$$n = \frac{S_{1\gamma}}{S_{0\gamma}} \frac{1}{Vt},$$

where V is the volume of the source, cm^3; t is the experiment time, s; n is the number of ^{234m}Pa atoms decaying in one second in one cubic centimeter and emitting a gamma quantum with an energy of 1.001 MeV.

Then we have the following equations for the total decay rate of ^{234m}Pa and the number of protactinium atoms:

$$N_p = n/(\eta_\gamma \lambda_p) = n\,T^{Pa}{}_{1/2}/(\ln 2 * \eta_\gamma),$$

where η_γ = 0.0084 is the probability of the branch of the gamma decay of ^{234m}Pa in the decay of ^{234}Pa; N_P is the number of ^{234}Pa atoms in 1 cm^3.

Knowing this number makes it possible to determine the number of ^{238}U atoms by the formula following from consideration of the kinetics of the decay chain of this nucleus, up to and including the decay of the ^{234}Pa nucleus. With sufficient precision:

$$N_u = \frac{T_{1/2}{}^{\mathrm{U}}}{T_{1/2}{}^{\mathrm{Pa}}} N_p,$$

where N_{U} is the number of U atoms in 1 cm^3; $T^{\mathrm{U}}_{1/2}$, $T^{\mathrm{Pa}}_{1/2}$ are the half-lives of U and Pa, respectively.

Applied to the above experiment, the final processing is as follows.

The number of protactinium gamma quanta emitted from 1 g of uranium per 1 s was determined (t_{ex} = 7200 s, m_{U} = 2.0563 g).

$$n_\gamma^{m\mathrm{Pa}} = \frac{S_{1\gamma}}{S_{0\gamma}} \frac{1}{t_{ex} m_{\mathrm{U}}},$$

where $T^{\mathrm{Pa}}_{1/2}$ = 1.2×60 s (half-life of ^{234m}Pa);

$n_\gamma^{m\mathrm{Pa}}$ = 0.84 % is the fraction of ^{234m}Pa decays along the gamma channel.

Then, as follows from the solution of the equations of kinetics of ^{238}U decay, the number of U atoms in 1 g of metal is equal to:

$$n\mathrm{U}^{238} = n_a{}^{\mathrm{Pa}}/(T_{1/2}{}^{\mathrm{Pa}})\,T_{1/2}{}^{\mathrm{U}}.$$

The metal is practically pure ^{238}U, therefore, to estimate the accuracy, we calculate the number of uranium atoms in 1 g-atom of the metal, for this the value obtained above must be multiplied by 238 (as result we have 5.73×10^{23}) and compared with the Avogadro number (6.022×10^{23}). The accuracy of the match is 4.8 %.

The activity of this uranium sample, reduced to 1 g, is easily estimated by the formula:

$$I = \frac{\mathrm{Log}2}{T_{1/2}{}^{\mathrm{U}}} n\mathrm{U}^{238}.$$

And in this case it was 11924 Bq/g, the deviation of the method in relation to the measured value

(25500 Bq per sample weighing 2.0563 g) was 3.84 %.

Uncertainty of describing method

The accuracy of the method is determined by the error in calculating the ratio $S_{1\gamma}/S_{0\gamma}$. It is clear that the error $S_{0\gamma}$ is determined by the specified statistical error in the Monte Carlo simulation and, accordingly, the relative error in this case is expressed as $1/N_p^{1/2}$, where N_p is the number of events recorded in the FAP region $E = 1.001$ MeV.

The relative error of $S_{1\gamma}$ can be represented as follows $(N^{1/2}_{ex+ph} + N^{1/2}_{ph})/(N_{ex+ph} - N_{ph})$, where N_{ex+ph} is the number of pulses in the FAP region $E = 1.001$ MeV of the experimental spectrum without subtraction of background pulses; N_{ph} is the number of pulses in the same energy range of the background spectrum.

The relative error of the ratio $S_{1\gamma}/S_{0\gamma}$ is then given by the sum of the above errors and is determined by the expression:

$$\frac{\sqrt{N_{ex+ph}} + \sqrt{N_{ph}}}{N_{ex+ph} - N_{ph}} + \frac{\sqrt{N_p}}{N_p}.$$

Further actions with the value $S_{1\gamma}/S_{0\gamma}$ for determining the amount of ^{238}U are associated only with the use of constants, which are known values and, therefore, do not affect the accuracy.

Conclusion

The paper considers a simple and reliable method for determination of ^{238}U which can be applied for the case when uranium is in various media. The method is based on measuring of a scintillation detector response to the ^{234m}Pa (1.001 MeV) gamma line.

An algorithm for processing and the necessary Monte Carlo simulation are proposed which makes it possible to determine the ^{238}U content in a medium or sample from experimental data. The operation of the algorithm is illustrated by the experiment example with a piece of metallic uranium. It is shown that the determination accuracy of the ^{238}U content in this case is 3–5 %.

References

1. Agbalagba E.O., Avwiri G.O., Chad-Umoreh Y.E. γ-Spectroscopy measurement of natural radioactivity and assessment of radiation hazard indices in soil samples from oil fields environment of Delta State, Nigeria. *Journal of environmental radioactivity*, 2012, vol. 109, pp. 64–70. **DOI:** 10.1016/j.jenvrad.2011.10.012

2. Analytical Methodology for the Determination of Radium Isotopes in Environmental Samples. *IAEA Analytical Quality in Nuclear Applications Series*, 2010, no. 19 VIENNA.

3. Seokki Cha, Siu Kim, Geehyun Kim. Development of fast measurements of concentration of NORM U-238 by HPGe. *Journal of Instrumentation*, 2017, vol. 12, P02013. **DOI:** 10.1088/1748-0221/12/02/P02013

4. Passive Nondestructive Assay of Nuclear Materials, Doug Reilly, 7 part, Hastings A. Smith, Jr. The Measurement of Uranium Enrichment, 1991.

5. Briestmeister J.F. Ed. MCNPA general Monte-Carlo N-particle transport code, Version 4A. Report LA12625-M, Los Alamos. NM, Los Alamos National Laboratory, 1994.

6. Wiener N. Extrapolation, interpolation and smoothing of stationary time series with engineering applications, J. Wiley, 1950.

7. BardinV. *Sposob dekonvolyucii spektrometricheskoj informacii i obnaruzheniya spektral'nyh pikov* [WAY Deconvolution spectrometer information and detection of spectral peaks]. *Nauchnoe priborostroenie* [Scientific instrumentation], 2017, vol. 27, no. 2, pp. 75–82 (in Russian). **DOI:** 10.18358/np-27-2-i7582

8. Wolfram Research, Inc., Mathematica, Version 12.1, Champaign, IL, 2020.

Methods for Accuracy Increasing of Solid Brittle Materials Fracture Toughness Determining

V.A. Lapitskaya[1,2], T.A. Kuznetsova[1,2], S.A. Chizhik[1,2], B. Warcholinski[3]

[1] *A.V. Luikov Heat and Mass Transfer Institute of NAS of Belarus,*
P. Brovki str., 15, Minsk 220072, Belarus

[2] *Belarusian National Technical University,*
Nezavisimosty Ave., 65, Minsk 220013, Belarus

[3] *Koszalin University of Technology,*
Sniadeckich str., 2, Koszalin 75-453, Poland

Received 10.11.2021
Accepted for publication 18.01.2022

Abstract

Method for determining of the fracture toughness of brittle materials by indentation is described. The critical stress intensity factor K_{IC} quantifies the fracture toughness. Methods were developed and applied to improve the accuracy of K_{IC} determination due to atomic force microscopy and nanoindentation. It is necessary to accurately determine parameters and dimensions of the indentations and cracks formed around them in order to determine the K_{IC}. Instead of classical optical and scanning electron microscopy an alternative high-resolution method of atomic force microscopy was proposed as an imaging method.

Three methods of visualization were compared. Two types of crack opening were considered: along the width without vertical displacement of the material and along the height without opening along the width. Due to lack of contact with the surface of the samples under study, the methods of optical and scanning electron microscopy do not detect cracks with a height opening of less than 100 nm (for optical) and less than 40–50 nm (for scanning electron microscopy). Cracks with opening in width are determined within their resolution. Optical and scanning electron microscopy cannot provide accurate visualization of the deformation area and emerging cracks when applying small loads (less than 1.0 N). The use of atomic force microscopy leads to an increase in accuracy of determining of the length of the indent diagonal up to 9.0 % and of determining of the crack length up to 100 % compared to optical microscopy and up to 67 % compared to scanning electron microscopy. The method of atomic force microscopy due to spatial three-dimensional visualization and high accuracy (XY ±0.2 nm, Z ±0.03 nm) expands the possibilities of using indentation with low loads.

A method was proposed for accuracy increasing of K_{IC} determination by measuring of microhardness from a nanoindenter. It was established that nanoindentation leads to an increase in the accuracy of K_{IC} determination by 16–23 % and eliminates the formation of microcracks in the indentation.

Keywords: fracture toughness, accuracy, indentation method, atomic force microscopy, nanoindentation.

DOI: 10.21122/2220-9506-2022-13-1-40-49

Адрес для переписки:
Лапицкая В.А.
Институт тепло- и массообмена имени А.В. Лыкова
НАН Беларуси,
ул. П. Бровки, 15, г. Минск 220072, Беларусь
e-mail: vasilinka.92@mail.ru

Address for correspondence:
Lapitskaya V.A.
A.V. Luikov Heat and Mass Transfer Institute of NAS of Belarus,
P. Brovki str., 15, Minsk 220072, Belarus
e-mail: vasilinka.92@mail.ru

Для цитирования:
V.A. Lapitskaya, T.A. Kuznetsova, S.A. Chizhik, B. Warcholinski.
Methods for Accuracy Increasing of Solid Brittle Materials Fracture Toughness Determining.
Приборы и методы измерений.
2022. – Т. 13, № 1. – С. 40–49.
DOI: 10.21122/2220-9506-2022-13-1-40-49

For citation:
V.A. Lapitskaya, T.A. Kuznetsova, S.A. Chizhik, B. Warcholinski.
Methods for Accuracy Increasing of Solid Brittle Materials Fracture Toughness Determining.
Devices and Methods of Measurements.
2022, vol. 13, no. 1, pp. 40–49.
DOI: 10.21122/2220-9506-2022-13-1-40-49

Способы повышения точности определения вязкости разрушения твёрдых хрупких материалов при индентировании

В.А. Лапицкая[1,2], Т.А. Кузнецова[1,2], С.А. Чижик[1,2], Б. Вархолински[3]

[1] *Институт тепло- и массообмена имени А.В. Лыкова НАН Беларуси,*
ул. П. Бровки, 15, г. Минск 220072, Беларусь

[2] *Белорусский национальный технический университет,*
пр-т Независимости, 65, г. Минск 220013, Беларусь

[3] *Кошалинский технологический университет,*
ул. Снядецких, 2, г. Кошалин 75-453, Польша

Поступила 10.11.2021
Принята к печати 18.01.2022

Приведено описание метода определения вязкости разрушения хрупких материалов индентированием. Количественно вязкость разрушения характеризуется критическим коэффициентом интенсивности разрушения K_{IC}. Использование атомно-силовой микроскопии и наноиндентирования позволило разработать и применить способы повышения точности определения K_{IC}. Для определения K_{IC} необходимо точно определять параметры и размеры отпечатков индентирования и образованных вокруг них трещин. В качестве метода визуализации вместо классических оптической и сканирующей электронной микроскопий предложен альтернативный высокоразрешающий метод атомно-силовой микроскопии.

Проведено сравнение трёх методов визуализации. Рассмотрено два типа раскрытия трещин: по ширине без смещения материала по вертикали и по высоте без раскрытия по ширине. Методы оптической и сканирующей электронной микроскопий из-за отсутствия контакта с поверхностью исследуемых образцов не определяют трещины с раскрытием по высоте менее 100 нм (для оптической) и менее 40–50 нм (для сканирующей электронной микроскопии). Трещины с раскрытием по ширине определяют в рамках своей разрешающей способности. Оптическая и сканирующая электронная микроскопии не могут обеспечить точную визуализацию области деформации и формирующихся трещин при применении малых нагрузок (меньше 1,0 Н). Применение атомно-силовой микроскопии приводит к повышению точности определения длины диагонали отпечатка до 9,0 % и определения длины трещины до 100 % по сравнению с оптической микроскопией и до 67 % по сравнению со сканирующей электронной микроскопией. Метод атомно-силовой микроскопии благодаря пространственной трёхмерной визуализации и высокой точности (по XY ±0,2 нм, по Z ±0,03 нм) расширяет возможности применения индентирования с применением низких нагрузок.

Предложен способ повышения точности определения K_{IC} за счёт измерения микротвёрдости с наноиндентора. Установлено, что наноиндентирование приводит к повышению точности определения K_{IC} на 16–23 % и исключает образование микротрещин в отпечатке.

Ключевые слова: вязкость разрушения, точность, метод индентирования, атомно-силовая микроскопия, наноиндентирование.

DOI: 10.21122/2220-9506-2022-13-1-40-49

Адрес для переписки:
Лапицкая В.А.
Институт тепло- и массообмена имени А.В. Лыкова НАН Беларуси,
ул. П. Бровки, 15, г. Минск 220072, Беларусь
e-mail: vasilinka.92@mail.ru

Address for correspondence:
Lapitskaya V.A.
A.V. Luikov Heat and Mass Transfer Institute of NAS of Belarus,
P. Brovki str., 15, Minsk 220072, Belarus
e-mail: vasilinka.92@mail.ru

Для цитирования:
V.A. Lapitskaya, T.A. Kuznetsova, S.A. Chizhik, B. Warcholinski.
Methods for Accuracy Increasing of Solid Brittle Materials Fracture Toughness Determining.
Приборы и методы измерений.
2022. – Т. 13, № 1. – С. 40–49.
DOI: 10.21122/2220-9506-2022-13-1-40-49

For citation:
V.A. Lapitskaya, T.A. Kuznetsova, S.A. Chizhik, B. Warcholinski.
Methods for Accuracy Increasing of Solid Brittle Materials Fracture Toughness Determining.
Devices and Methods of Measurements.
2022, vol. 13, no. 1, pp. 40–49.
DOI: 10.21122/2220-9506-2022-13-1-40-49

Introduction

Reducing of the measurement error of any physical quantity is always an urgent task. Development of new methods, use of other physical techniques allows them to be applied to existing measurement methods to improve accuracy and reduce the error in determining of physical quantities. In this work, we will present a method for measuring the physical and mechanical properties of hard brittle materials, namely, fracture toughness (or crack resistance). This parameter characterizes the limiting state of any solid material and the ability to resist crack development [1–6]. It is extremely important for various types of ceramics (carbide, oxide, nitride) [7, 8] and coatings based on them, which combine special physical-mechanical, thermophysical, bioinert, antioxidant and wear-resistant properties [2, 7]. One of the main tasks of ceramic production technology is to increase their strength, to prevent the likelihood of sudden brittle fracture, appearance of chips on the surface, or even the destruction of the part.

The critical stress intensity factor K_{IC} quantifies the fracture toughness [1, 3–6]. There are many methods to determine this characteristic (bending, torsion, rupture, etc.). However, all of them are of limited use due to the complexity or impossibility of preparing test samples with the required notch geometry and are economically unprofitable. The indentation method [4–6, 9] does not require samples of complex shape. It uses thin sections and consists in the study of the deformation area on the material surface after indentation, followed by the calculation of K_{IC}.

The purpose of the work was to improve the accuracy of determining the critical stress intensity factor K_{IC} by using the methods of atomic force microscopy and nanoindentation, to establish the influence of the visualization method of the deformation area, the calculation model, and microhardness values on the accuracy of determining K_{IC}.

Analysis of the method for determining fracture toughness by indentation

Determination of fracture toughness K_{IC} by indentation is based on the introduction of a diamond indenter in the form of a tetrahedral Vickers pyramid into the surface of the test sample (Figure 1) under a selected load depending on the material and size of the sample [3–6]. Performed at least three indentations at each load. The prints are visualized in an optical microscope (OM) or a scanning electron microscope (SEM) after indentation, the length of the print diagonals d_1 and d_2 is determined, and the print half-diagonal length $a = (d_1 + d_2)/4$ is calculated. Measured the length of the cracks (l is the length of the crack near the indent, c is the length of the crack measured from the center of the indent) near each indent, and then determine the average values of the crack lengths for the sample. Determined the physical and mechanical properties of the material (microhardness H_V and elasticity modulus E). On the ratio c/a determines the type of cracks (Palmquist cracks or median cracks) [6] around the prints after determining the values of a, l, c, H_V and E. A mathematical calculation model is selected depending on the type of cracks and the critical stress intensity factor K_{IC} is determined.

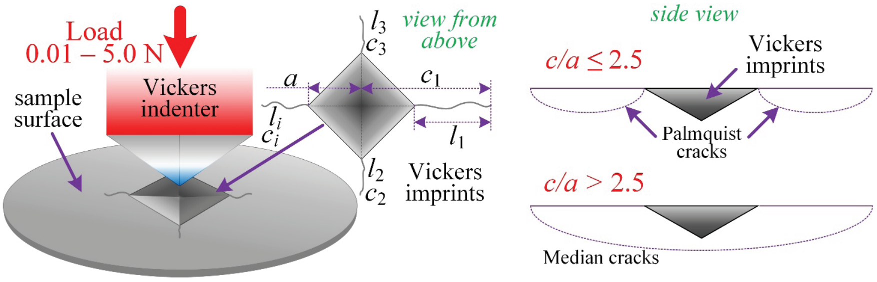

Figure 1 – Method and indentation imprint with defined parameters

Development of methods for reducing the error in determination of fracture toughness by the indentation method

Determination of fracture toughness by indentation is a computational and experimental method. To accurately determine K_{IC}, it is important both to use mathematical calculation models (adequate to the range not only of high loads from 1.0 N and above, but also to low loads of 0.01–0.5 N) and accurate experimental characteristics of the material and the deformation region. There are factors that affect the accuracy of determining the fracture toughness of a material by indentation. These include the following factors: the accuracy of determining the length of the diagonals of the indentation mark and the length of the cracks around it; method for determining the microhardness of a material.

Mathematical Model of Calculation. There are many mathematical models for determining the critical stress intensity factor K_{IC} [10]. In most of the models used earlier in the literature, loads of more than 1 N were used. In cases where small loads (0.25–0.75 N) were used, the values of a, l and c were determined inaccurately, and because of this, at low loads, the difference in a, l and c was not detected. Justification of the choice and determination of the correctness of mathematical models for calculating K_{IC} and their ability to maintain the stability of K_{IC} values in a wide range of loads, primarily at low loads (from 0.01 to 0.5 N), will expand the capabilities of the indentation method.

Visualization of the Deformation Area. OM and SEM are used in the classical approach to visualize indentation prints, determine the length of the diagonals of the indentation print and the length of cracks around it on the surface of the material under study. Each of these methods allows, within its resolution, to determine the linear geometric dimensions of the indentation imprint and the formed cracks.

The resolution of an optical microscope is characterized by the smallest distance between two points that are visible separately in the microscope. This distance is directly proportional to the wavelength of the light radiation incident on the object under study. The minimum dimensions of a distinguishable object are approximately equal to half the wavelength of the incident light. Standard optical microscopes use visible light. Objects around $0.25 \cdot 10^{-6}$ m or 250 nm in size can be seen under a microscope.

The resolution of the SEM is determined by the electron wavelengths and the numerical aperture of the system. The wavelength of electron radiation depends on its energy, which is affected by the accelerating voltage. The electron energy is $E = V \cdot e$, where V – potential difference, traversable by electron; e – electron charge. Thus, objects larger than 1.0–1.2 nm in size can be distinguished in the SEM.

If you change the OM and SEM measurement method to a micromechanical method – atomic force microscopy (AFM) with a vertical resolution of at least 0.03 nm, then due to spatial three-dimensional visualization (which neither OM nor SEM has), it becomes possible to determine the depth of the indentation imprint and cracks, as well as the height of their opening [11]. In AFM the resolution depends on the radius of curvature of the tip of the used probe and the nature of its interaction with the surface of the object (contact or semi-contact) [12]. The AFM resolution in XY is limited by the capabilities of the device and is 0.2–0.5 nm.

Microhardness Definition. To determine the fracture toughness K_{IC}, it is necessary to determine the microhardness and elastic modulus of the material under study. Indentations are carried out at various loads, three to five (minimum number) of indentations at each load to determine K_{IC}. The classical method for determining fracture toughness K_{IC} uses the values of microhardness H_V determined by the Vickers method (GOST 9377–81). Microhardness H_V according to the Vickers method is determined by the formula (1) [13]:

$$H_V = 1.854 \frac{P}{d_{mean}^2}, \tag{1}$$

where d_{mean} is arithmetic mean of the diagonals of the imprint of a tetrahedral Vickers pyramid after indentation, m; P is indenter load, N.

During indentation, all the energy consists of the elastic and plastic components of the deformation and is spent on the formation of an imprint on the surface sample. The presence of cracks around the indentation indicates that part of the energy was spent on their formation in the sample, as well as the inability to reliably determine the microhardness of the sample material. Unreliable values of Vickers microhardness H_V lead to incorrect determination of K_{IC}.

An alternative method for determining microhardness can be the method of nanoindentation (NI). A Berkovich-type diamond indenter and loads of no more than 5 mN are used when measuring microhardness on a nanoindenter (ISO 14577-1:2015). The microhardness H_{Ber} by the NI method is determined by the formula [14]:

$$H_{Ber} = \frac{P_{\max}}{A}, \tag{2}$$

where $P_{\max}$ is maximum indentation force of the Berkovich pyramid, N; A is resulting contact area under this load, m^2.

Contact area A was determined by the formula [14]:

$$A = \frac{\pi}{4}\left(\frac{S}{E_r}\right)^2, \tag{3}$$

where S is unload curve stiffness; E_r is reduced module, GPa.

The use of a high-precision NI method and low loads makes it possible to exclude the formation of cracks in the material. Accordingly, the microhardness values determined by this method are correct and accurate.

Samples and equipment

To compare the visualization methods of the deformation area, diagonals of the length of the indentation print and length cracks, we used: an optical microscope MICRO-200 (JSC Planar, Republic of Belarus) and a lens with a magnification of 400×, SEM – JSM-7001F (JEOL, Japan) with resolution in secondary electrons 1.2 nm (at an accelerating voltage of 30 kV) and AFM – Dimension FastScan (Bruker, USA) with XY resolution ±0.2 nm, Z ±0.03 nm. A section of silicon carbide ceramic was used as a sample [7, 8]. Microhardness imprints on the sample were made using a PMT-3M microhardness tester (LOMO, Russia) with a Vickers tetrahedral diamond pyramid at a constant load of 1.0 and 2.0 N.

Experimental determination of the influence of the mathematical calculation model and the method for determining microhardness on the value of fracture toughness K_{IC} was carried out on several materials – single-crystal silicon wafers Si of three orientations (100), (110) and (111) (JSC "INTEGRAL", Belarus) with a size of Ø100 mm and a thickness of 0.5 mm, AT-cut quartz plates with a diameter of 12 mm and a thickness of 3 mm after chemical-mechanical (CMP) and magnetorheological (MRF) polishing, slide and cover glass. Indentation prints were made using a PMT-3M microhardness tester with a load from 0.01 to 5.0 N

Five indentations were performed for each load. Then visualization was carried out using AFM, the indentation parameters (d_1, d_2) and crack length (l, c) were determined. Microhardness was determined by two methods: by Vickers using formula (1), by the NI method (load 5 mN). Microhardness H_V by the Vickers method was determined on PMT-3M. The NI method was determined using a Hysitron 750 Ubi nanoindenter (Bruker, United States) with a Berkovich-type diamond tip with a curvature radius of 60 nm [14]. Then K_{IC} was determined.

The contribution of the mathematical model of calculation to the accuracy of determining the fracture toughness

With the existing set of models for calculating K_{IC} using the indentation method, it has been established that it is impossible to correctly determine the fracture toughness of the material under study using most models, especially at low indentation loads (0.01–0.5 N). The models used for comparison are given in [15]. K_{IC} for each sample was determined at loads of 0.01–5.5 N using six formulas from [15]. It was found that the mathematical models of calculation (4) and (5) [3, 5, 6, 15] given below show the correctness and stability of the K_{IC} values in the entire range of loads (from 0.01 to 5.5 N). These models are designed and are given in [5, 6]. Unlike others, they include the parameters of the indentation imprint (diagonals length d) and the formed cracks length l and c. Also include parameters characterizing the material (microhardness H and elasticity modulus E):

$$K_{IC} = 0.048\left(\frac{l}{a}\right)^{-\frac{1}{2}} \cdot \left(\frac{H_V}{E\Phi}\right)^{-\frac{2}{5}} \cdot \left(\frac{H_V a^{\frac{1}{2}}}{\Phi}\right); \tag{4}$$

$$K_{IC} = 0.129\left(\frac{c}{a}\right)^{-\frac{3}{2}} \cdot \left(\frac{H_V}{E\Phi}\right)^{-\frac{2}{5}} \cdot \left(\frac{H_V a^{\frac{1}{2}}}{\Phi}\right), \tag{5}$$

where l is crack length near the indent, m; a is half-diagonal length, m; E is elasticity modulus, GPa; Φ is bond reaction index in the crystal lattice ($\Phi \approx 3$); H_V is Vickers hardness, GPa; c is crack length from the center of the indent, m.

In works [5, 6] in addition to models, described the conditions for their selection depending on the type of cracks (Figure 1). The condition is as follows: if $c/a \leq 2.5$, then Palmquist cracks form in the sample (Figure 1) and the calculation is carried out according to model (4), and if $c/a > 2.5$, then median cracks form in the sample (Figure 1) and the calculation is carried out by model (5) [5, 6].

According to the obtained values for each load, the average value was determined using six formulas from [15] (Table 1). The values according to formulas (4) and (5) depending on the c/a ratio were taken as the actual K_{IC} values for the test material with a standard deviation of less than 10 % [15]. Bold type in Table 1 indicates the actual K_{IC} values for each sample.

It has been established that deviations from the actual values of fracture toughness of 12–74 % (Table 2) give mathematical models [15] that depend directly on the load P (Figure 3).

Table 1

Fracture toughness and deviation from the actual value for silicon, quartz and glass

Silicon					
K_{IC}, (MPa·m$^{1/2}$)			Deviation of the K_{IC} value in % from the actual value		
(100)	(110)	(111)	(100)	(110)	(111)
0.59±0.11	1.10±0.55	0.74±0.42	50.9	12.4	37.8
0.74±0.22	1.06±0.54	0.86±0.15	38.0	15.7	27.5
1.20±0.05	**1.26±0.09**	**1.19±0.10**	0.0	0.0	0.0
0.38±0.07	0.55±0.32	0.46±0.33	68.1	56.4	61.5
1.23±0.07	1.24±0.08	1.20±0.08	2.5	1.6	0.8
0.31±0.13	0.45±0.21	0.39±0.22	74.3	64.3	67.2

Quartz			
CMP	MRF	CMP	MRF
1.89±0.89	1.15±0.51	29.8	17.5
1.78±0.77	1.57±0.69	22.0	11.9
1.46±0.12	**1.40±0.17**	0.0	0.0
0.95±0.38	0.88±0.38	34.7	37.3
1.54±0.13	1.33±0.15	5.3	4.7
0.58±0.23	0.46±0.21	60.0	67.2

Glass			
Slide	Cover	Slide	Cover
1.97±0.47	1.67±0.08	37.48	51.49
2.15±0.04	1.88±0.09	50.25	70.76
1.42±0.03	**1.10±0.05**	0.0	0.0
1.06±0.30	0.92±0.04	25.88	16.03
1.39±0.01	1.11±0.05	2.46	0.91
0.60±0.17	0.49±0.02	57.70	55.67

Comparison of visualization methods and the accuracy of determining the diagonals of the imprint of length and cracks

Visualization of the deformation area (or indentation imprint) was carried out on OM, SEM and AFM after applying marks (Figure 2). Comparison of the quality and accuracy of imaging compared on a specific selected imprint. On optical images (Figure 2*a*, *b*), the selected indentations are marked with a red square.

These imprints were then visualized using SEM and AFM (Figure 2). It is very difficult to accurately determine the presence of cracks around the imprint and their length from optical images. The length d_1 and d_2 of the imprints is determined approximately (Table 2). SEM images do not always clearly show the borders of the imprint (Figure 2*a*). Diagonal length cannot be determined exactly. When comparing the determination of the length of the indent diagonals (d_1 and d_2), it was found that AFM allows increasing the accuracy of determining the length of the diagonal up to 9 % compared to OM and up to 2.3 % compared to SEM, if scanning fields of 10×10 μm^2–50×50 μm^2 are used.

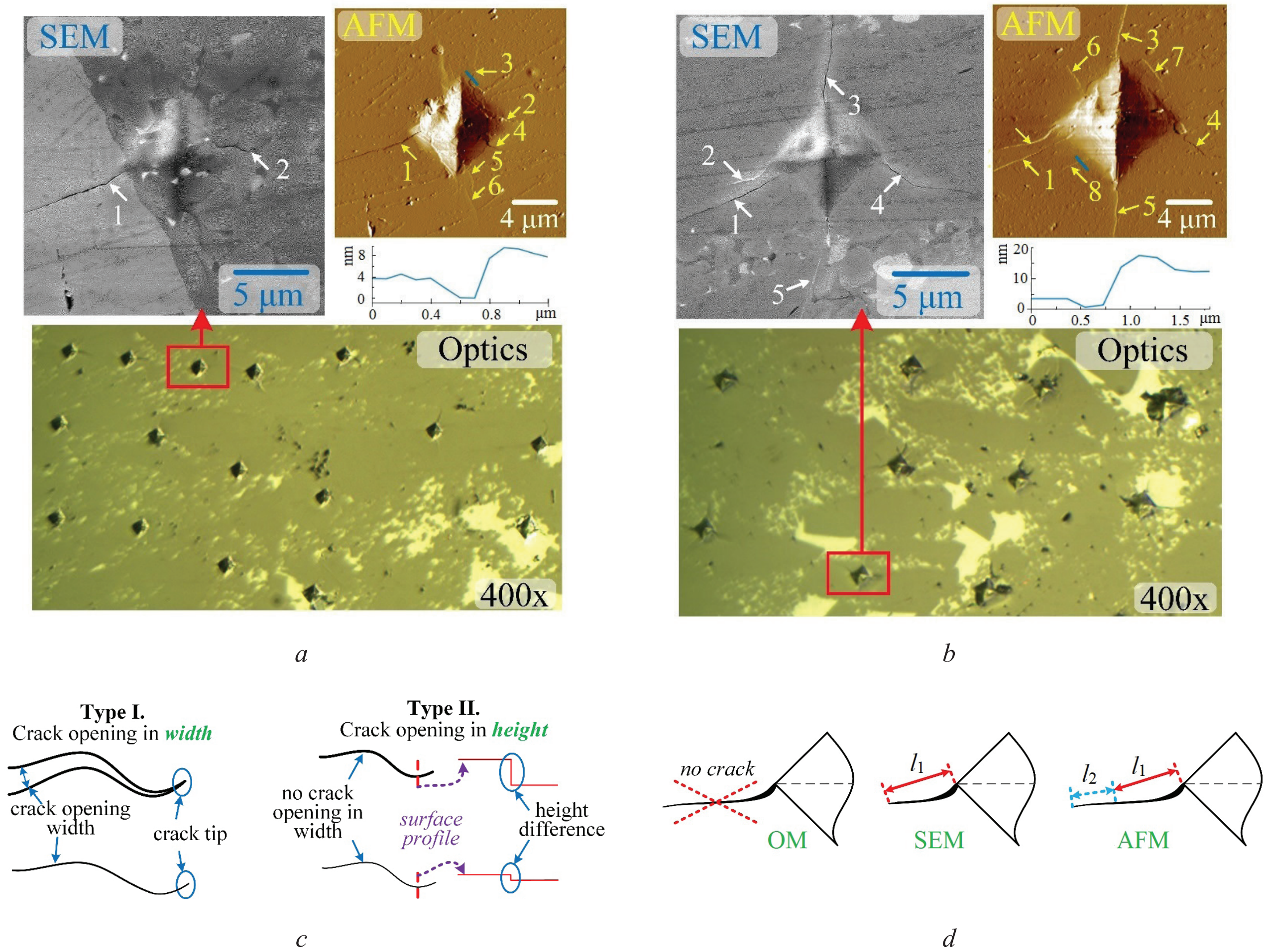

a *b*

c *d*

Figure 2 – Optical (400×), images from scanning electron and atomic force microscopy of imprints (*a*, *b*), features of crack opening (*c*) and influence on the accuracy of determining their length (*d*): *a* – 1.0 N; *b* – 2.0 N; *c* – two types of crack opening; *d* – determination of *l* crack (using the example of crack No. 2 in Figure 2*b*)

Table 2

Indentation diagonal length and percentage difference compared to optical microscopy

	OM		SEM				AFM			
					%				%	
P, N	1.0 N	2.0 N	1.0 N	2.0 N	1.0 N	2.0 N	1.0 N	2.0 N	1.0 N	2.0 N
d_1, μm	9.97	10.61	9.00	11.25	9.7	6.0	9.19	11.52	7.8	8.6
d_2, μm	10.07	11.54	9.20	11.35	8.6	1.6	9.24	11.37	8.2	1.5

During indentation, two types of crack opening are formed: the first type is widthwise opening, the second type is vertical opening (Figure 2*c*). Cracks of the first type open in the *XY* plane without vertical displacement of the material. Cracks of the second type open along the *Z* axis with little or no width opening (Figure 2*c*). OM and SEM detect cracks of the first type (in width) only within their resolution. OM reveals cracks with a width opening of at least 250 nm, SEM – at least 1–1.2 nm. Cracks of the second type (with opening) are either not detected by OM and SEM, or they are determined, but not the entire length: the height difference should be at least 100 nm for OM and at least 40–50 nm for SEM. The study of the deformation area around the indentations using OM showed good visualization of cracks, the opening width of which is greater than its resolution – 250 nm (Figure 2*a*, *b*). After applying a load of 1.0 N, it was not possible to determine the presence of cracks around the indentation imprint using OM (Figure 2*a*). After applying a load of 2.0 N near the studied imprint, it was possible to determine the presence and length of three cracks (Figure 2*b*, Table 3). It was also found that during visualization, the crack is visible with a large opening. Closer to the crack tip, the opening decreases and becomes invisible in an optical microscope. For this reason, the crack length is incorrectly determined.

When examining the same prints in the SEM, from two (Figure 2*a*, marked with white arrows) to five cracks around the imprint (Figure 2*b*, marked with white arrows) were detected. The SEM perfectly visualizes cracks with an opening or a height difference of more than 40–50 nm.

AFM made it possible to identify from six (Figure 2*a*, marked with yellow arrows) to eight cracks around the indentation imprint (Figure 2*b*, marked with yellow arrows). The absence of cracks after a load of 1.0 N when visualized with an optical microscope shows a 100 % error compared to AFM, i. e. OM reveals nothing compared to AFM or SEM. The accuracy of determining the crack tip on AFM is due to the surface profile.

You can see how a crack of the second type with vertical opening is visualized using OM, SEM and AFM using the example of crack No. 2 in Figure 2*b*. Schematically, for comparison, this is shown in Figure 2*d*. On OM this crack could not be determined. The SEM shows only a part of a crack of length l_1 with a large difference (56–73 nm) in height without opening. AFM showed that the crack has a length of l_1+l_2 and is almost twice as large (Table 2) as compared to the SEM value.

Detection of cracks after 2.0 N is due to the larger width of crack opening compared to AFM and makes it possible to detect only 37 % of all cracks. SEM makes it possible to detect from 33 to 75 % of all cracks, depending on the applied load, i. e. the higher the load, the larger the cracks and better visible in the SEM.

Now let's compare the cracks, the length of which was determined by all three methods, as well as the error obtained by incorrect determination of the crack length (Table 3). These cracks correspond to numbers No. 1, 3 and 4 in Table 2 after a load of 2.0 N. As a result, the use of AFM makes it possible to increase the determination accuracy up to 100 % (Table 4).

Table 3

Crack length around indentation imprint and length errors compared to atomic force microscopy

Type		OM				SEM				AFM	
Load, N		1.0	%	2.0	%	1.0	%	2.0	%	1.0	2.0
Crack No, μm	1	no cracks found	100	14.01	30	15.80	3	16.40	18	16.29	20.09
	2			–	100	6.30	9	6.94	39	6.39	11.39
	3			10.53	46	–	100	19.80	1	6.78	19.64
	4			10.08	24	–	100	10.28	23	4.52	13.31
	5			–	100	–	100	16.50	15	5.97	19.41
	6			–	100	–	100	13.04	0	10.06	13.02
	7			–	100	–	–	–	100	–	10.79
	8			–	100	–	–	–	100	–	9.57

Table 4

Resolution and errors of visualization methods

Type	Resolution, nm	Error in determining, %	
		d	c
OM	at least 250	up to 9.0	up to 100
SEM	at least 1.0	up to 2.3	up to 67.0
AFM	at least 0.2 (by XY), at least 0.03 (by Z)	up to 2.0	

Comparison of methods for determining microhardness

The results of determining the microhardness are shown in Table 5. The values of the elasticity modulus E of the samples were measured on the NI.

After determining a, l, c, E and H, one of the formulas (4) and (5) was selected with respect to c/a. Then K_{IC} was calculated. It has been established that the values of microhardness with NI compared with Vickers differ by 1.2–1.6 times or by 25–38 % (Table 5). This leads to an error in determining the K_{IC} of 16–23 % (Table 5).

Table 5

Values of microhardness, fracture toughness and errors of their determination by two methods

Sample	Microhardness H, GPa			K_{IC}, MPa·m$^{1/2}$		
	Vickers	NI	%	Vickers	NI	%
Si (100)	8.6±0.9	13.8±0.6	37.7	0.97±0.05	1.20±0.05	19.2
Si (110)	8.8±0.4	13.6±0.7	35.3	1.00±0.05	1.26±0.09	20.6
Si (111)	8.4±0.3	13.4±0.7	37.6	0.99±0.06	1.19±0.10	16.8
Quartz MRF	10.0±0.7	13.5±0.1	25.9	1.17±0.17	1.40±0.21	16.4
Glass slide	10.1±0.6	6.7±0.1	33.6	1.82±0.04	1.42±0.03	22.0
Cover glass	10.1±0.2	6.4±2.4	36.6	1.45±0.07	1.10±0.05	23.9

Conclusion

Three ways to improve the accuracy of determining of the critical stress intensity factor K_{IC}, which quantitatively characterizes the fracture toughness, were considered: the choice of a mathematical calculation model, the use of atomic force microscopy to visualize the deformation region, and the nanoindentation method to determine the microhardness and elasticity modulus of the material.

It was established that changing the physical principle of the visualization method for cracks and indentation parameters from optical to micromechanical (atomic force microscopy) leads to a decrease of the error in determining of the indent diagonal length by 2.3–9.0 %. This also leads to a decrease of the error in determining of the crack length by 46–100 % compared to optical microscopy and 24–67 % compared to scanning electron microscopy. The method of atomic force microscopy proposed in this work for visualizing of the deformation region due to spatial three-dimensional visualization, atomic forces and high accuracy (XY ±0.2 nm, Z ±0.03 nm) can significantly expand the possibilities of using the indentation method. It becomes possible to determine the fracture toughness of individual phases in a material and individual elements of microelectromechanical systems through the use of small loads.

The use of the nanoindentation method instead of the Vickers method made it possible to increase the accuracy of determining of the material's microhardness up to 38 %, as well as the critical stress intensity factor K_{IC} up to 23 %.

Acknowledgments

This research was supported by the grant of Belarusian Republican Foundation for Fundamental Research BRFFR No. F20M-083 and T21MS-029, as part of the assignment No. 2.3 SPSR "Energy and nuclear processes and technologies".

References

1. Gdoutos E.E. Fracture Mechanics. *Cham: Springer*, 2020, vol. XIX, 477 p.
DOI: 10.1007/1-4020-3153-X

2. Ritchie R., Liu D. Introduction to Fracture Mechanics. 1^{st} Edition. *Elsevier*, 2021, 160 p.
DOI: 10.1016/C2020-0-03038-0

3. Moradkhani A., Baharvandi H., Tajdari M., Latifi H., Martikainen J. Determination of fracture toughness using the area of micro-crack tracks left in brittle materials by Vickers indentation test. *Journal of Advanced Ceramics*, 2013, vol. 2(1), pp. 87–102.
DOI: 10.1007/s40145-013-0047-z

4. Evans A.G. Fracture Toughness Determinations by Indentation. *Journal of the American Ceramic Society*, 1976, vol. 59, pp. 371–372.
DOI: 10.1111/j.1151-2916.1976.tb10991.x

5. Niihara K., Morena R., Hasselman D.P.H. Evaluation of K_{IC} of brittle solids by the indentation method with low crack-to-indent ratios. *Journal of Materials Science Letters*, 1982, vol. 1, pp. 13–16.
DOI: 10.1007/BF00724706

6. Niihara K. A fracture mechanics analysis of indentation-induced Palmqvist crack in ceramics. *Journal of Materials Science Letters*, 1983, vol. 2, pp. 221–223.
DOI: 10.1007/BF00725625

7. Grinchuk P.S., Kiyashko M.V., Abuhimd H.M., Alshahrani M.S., Stepkin M.O., Toropov V.V., Khort A.A., Solovei D.V., Akulich A.V., Shashkov M.D., Liakh M.Yu. Effect of technological parameters on densification of reaction bonded Si/SiC ceramics. *Journal of the European Ceramic Society*, 2018, vol. 38, pp. 4815–4823.
DOI: 10.1016/j.jeurceramsoc.2018.07.014

8. Grinchuk P.S., Kiyashko M.V., Abuhimd H.M., Alshahrani M.S., Solovei D.V., Stepkin M.O., Akulich A.V., Shashkov M.D., Kuznetsova T.A., Danilova-Tretiak S.M., Evseeva L.E., Nikolaeva K.V. Advanced technology for fabrication of reaction-bonded SiC with controlled composition and properties. *Journal of the European Ceramic Society*, 2021, vol. 41, pp. 5813–5824.
DOI: 10.1016/j.jeurceramsoc.2021.05.017

9. Scholz T., Schneider G.A., Muñoz-Saldaña J., Swain M.V. Fracture toughness from submicron derived indentation cracks. *Applied Physics Letters*, 2004, vol. 84, pp. 3055. **DOI:** 10.1063/1.1711164

10. Sergejev F. Comparative study on indentation fracture toughness measurements of cermets and hardmetals. *Estonian Journal of Engineering*, 2006, vol. 12(4), pp. 43–48. **DOI:** 10.3176/eng.2006.4.07

11. Lapitskaya V.A., Kuznetsova T.A., Khabarava A.V., Chizhik S.A., Aizikovich S.M., Sadyrin E.V., Mitrin B.I., Sun Weifu. The use of AFM in assessing the crack resistance of silicon wafers of various orientations. *Engineering Fracture Mechanics*, 2022, vol. 259, pp. 107926.
DOI: 10.1016/j.engfracmech.2021.107926

12. Pogotskaia I.V., Kuznetsova T.A., Chizhik S.A. Elastic Modulus Determination of Nanolayers by the Atomic-Force Microscopy Method. *Mekhanika mashin, mekhanizmov i materialov* [Mechanics of Machines, Mechanisms and Materials], 2011, no. 3(16), pp. 43–48 (in Russian).

13. Oreshko E.I., Utkin D.A., Erasov V.S., Lyakhov A.A. Methods of measurement of hardness of materials (review). *Trudy VIAM* [Proceedings of VIAM], 2020, no. 1(85), pp. 101–117 (in Russian).
DOI: 10.18577/2307-6046-2020-0-1-101-117

14. Oliver W.C., Pharr G.M. An improved technique for determining hardness and elastic modulus using load and displacement sensing indentation experiments. *Journal of Materials Research*, 1992, vol. 7, pp. 1564–1583.
DOI: 10.1557/JMR.1992.1564

15. Lapitskaya V.A., Kuznetsova T.A., Khudoley A.L., Khabarava A.V., Chizhik S.A., Aizikovich S.M., Sadyrin E.V. Influence of polishing technique on crack resistance of quartz plates. *International Journal of Fracture*, 2021, vol. 231, no. 1, pp. 61–77.
DOI: 10.1007/s10704-021-00564-5

Method for Increasing of Lens Gluing Technological Process Efficiency and a Reliable Evaluation of Output Controlled Parameters

R.V. Fiodortsev[1], E.A. Metelskaya[2], V.A. Marchik[2], A.V. Kuznetsov[1,2], A.E. Makarevich[2]

[1]Belarusian National Technical University,
Nezavisimosty Ave., 65, Minsk 220013, Belarus

[2]JSC “Peleng”,
Makayonka str., 2, Minsk 220114, Belarus

Received 04.10.2021
Accepted for publication 08.02.2022

Abstract

The use of glued lens components in optical devices improves the image quality of telescopic and photographic lenses or inverting systems by eliminating a number of aberrations, and also reduces light losses in the optical system of the device. The traditional production process of lenses gluing involves the sequential execution of a set of technological operations and takes a significant period of time. The purpose of the research was to improve the accuracy and productivity of the technological process of lenses gluing by improving the optical system of the control and measuring device and automating the operation of lenses optical axes combining by introducing an electronic reference system and mechanisms for micro-movements of optical parts.

A technique is proposed for centering of two and three-component optical blocks by an autocollimation flare which provides a matching accuracy of less than 0.5 μm. The possibility of constructive modernization of the classic ST-41 autocollimation microscope with parallel separation of the displayed output information in the visual and television channels is shown. An automated system for controlling of the process of convergence of autocollimation points in the device is proposed. Using software methods an electronic grid template is formed on the monitor screen, onto which images of autocollimation points are projected. The decentering value $2\Delta e$ is determined and a corrective control voltage is applied to three stepper motors and pushers for transverse movement of the glued optical part.

Specialized software has been developed for automatically bringing the position of the autocollimating crosshair to the center of the measuring scale of the grid based on a combination of two methods of “least squares” and “successive approximation”. Compliance with a number of technological transitions and the accompanying control of geometric parameters make it possible to achieve greater accuracy in determining the eccentricity of the crosshairs of the aligned optical axes of the glued lenses.

Keywords: decentering, lens, crosshair, optical axis.

DOI: 10.21122/2220-9506-2022-13-1-50-59

Адрес для переписки:
Фёдорцев Р.В.
Белорусский национальный технический университет,
пр-т Независимости, 65, г. Минск 220013, Беларусь
e-mail: feod@tut.by

Address for correspondence:
Fiodortsev R.V.
Belarusian National Technical University,
Nezavisimosty Ave., 65, Minsk 220013, Belarus
e-mail: feod@tut.by

Для цитирования:
R.V. Fiodortsev, E.A. Metelskaya, V.A. Marchik, A.V. Kuznetsov, A.E. Makarevich.
Method for Increasing of Lens Gluing Technological Process Efficiency and a Reliable Evaluation of Output Controlled Parameters.
Приборы и методы измерений.
2022. – Т. 13, № 1. – С. 50–59.
DOI: 10.21122/2220-9506-2022-13-1-50-59

For citation:
R.V. Fiodortsev, E.A. Metelskaya, V.A. Marchik, A.V. Kuznetsov, A.E. Makarevich.
Method for Increasing of Lens Gluing Technological Process Efficiency and a Reliable Evaluation of Output Controlled Parameters.
Devices and Methods of Measurements.
2022, vol. 13, no. 1, pp. 50–59.
DOI: 10.21122/2220-9506-2022-13-1-50-59

Метод повышения эффективности технологического процесса склейки линз и достоверная оценка выходных контролируемых параметров

Р.В. Фёдорцев[1], Е.А. Метельская[2], В.А. Марчик[2], А.В. Кузнецов[1,2], А.Е. Макаревич[2]

[1]Белорусский национальный технический университет
пр-т Независимости, 65, г. Минск 220013, Беларусь

[2]ОАО «Пеленг»,
ул. Макаёнка, 25, г. Минск 220114, Беларусь

Поступила 04.10.2021
Принята к печати 08.02.2022

Применение в оптических приборах склеенных линзовых компонентов позволяет повысить качество изображения телескопических и фотографических объективов или оборачивающих систем за счёт устранения ряда аберраций, а также обеспечивает уменьшение световых потерь в оптической системе прибора. Традиционный производственный процесс склеивания линз предусматривает последовательное выполнение комплекса технологических операций и занимает существенный промежуток времени. Цель исследований заключалась в повышении точности и производительности технологического процесса склейки линз за счёт совершенствования оптической системы контрольно-измерительного прибора и автоматизации операции совмещения оптических осей линз путём введения электронной системы отсчёта и механизмов для микроперемещений оптических деталей.

Предложена методика центрирования двух- и трёхкомпонентных оптических блоков по автоколлимационному блику, обеспечивающая точность совмещения менее 0,5 мкм. Показана возможность конструктивной модернизации классического автоколлимационного микроскопа СТ-41 с параллельным разделением отображаемой выходной информации в визуальном и телевизионном каналах. Предложена автоматизированная система управления процессом сведения автоколлимационных точек в приборе. Программными методами на экране монитора формируется шаблон электронной сетки, на которую проецируются изображения автоколлимационных точек, определяется величина децентричности $2\Delta e$ и подаётся корректирующее управляющее напряжение на три шаговых двигателя и толкатели для поперечной подвижки приклеиваемой оптической детали.

Разработано специализированное программное обеспечение для автоматического сведения положения автоколлимационного перекрестия в центр измерительной шкалы сетки, основанное на сочетании двух методов – «наименьших квадратов» и «последовательного приближения». Соблюдение ряда технологических переходов и сопутствующий контроль геометрических параметров позволяют добиться большей точности при определении величины эксцентриситета перекрестия совмещаемых оптических осей склеиваемых линз.

Ключевые слова: децентрировка, линза, перекрестие, оптическая ось.

DOI: 10.21122/2220-9506-2022-13-1-50-59

Адрес для переписки:
Фёдорцев Р.В.
Белорусский национальный технический университет,
пр-т Независимости, 65, г. Минск 220013, Беларусь
e-mail: feod@tut.by

Address for correspondence:
Fiodortsev R.V.
Belarusian National Technical University,
Nezavisimosty Ave., 65, Minsk 220013, Belarus
e-mail: feod@tut.by

Для цитирования:
R.V. Fiodortsev, E.A. Metelskaya, V.A. Marchik, A.V. Kuznetsov, A.E. Makarevich.
Method for Increasing of Lens Gluing Technological Process Efficiency and a Reliable Evaluation of Output Controlled Parameters.
Приборы и методы измерений.
2022. – Т. 13, № 1. – С. 50–59.
DOI: 10.21122/2220-9506-2022-13-1-50-59

For citation:
R.V. Fiodortsev, E.A. Metelskaya, V.A. Marchik, A.V. Kuznetsov, A.E. Makarevich.
Method for Increasing of Lens Gluing Technological Process Efficiency and a Reliable Evaluation of Output Controlled Parameters.
Devices and Methods of Measurements.
2022, vol. 13, no. 1, pp. 50–59.
DOI: 10.21122/2220-9506-2022-13-1-50-59

Introduction

The use of glued lens components in optical devices can significantly improve the image quality of telescopic and photographic lenses or enveloping systems by eliminating chromatic and spherical aberrations, coma, and also reduces light losses in the optical system of the device by up to 10 % compared to by an independent mechanical method of each part fixing [1, 2].

The traditional production process of lenses from optical glass gluing provides for the sequential execution of a number of technological operations: the assembly of optical parts according to the shape accuracy of mating spherical surfaces within a given tolerance; cleaning the working surfaces of parts from various kinds of contaminants; applying a layer of glue on a concave surface, pressing and maintaining a uniform thickness within 0.005–0.02 mm; mutual centering of glued optical parts (combination of optical and geometric axes) by means of autocollimation instrumentation; if necessary, heating the parts in a thermal chamber to a temperature (70–130 °C) when gluing with a polymerizing optical adhesive; holding the set position and cooling the glued component to room temperature 20–45 °C (polymerization) for 1–4 days, depending on the brand of glue used (GOST 14887).

Thus the technological process of optical parts gluing is determined by a set of parameters: the brand and properties of the adhesive used (GOST 14887-80), the dimensions and material of the original elements, the error of the mating surfaces (no more than $N = 3–5$ interference Newton's rings of a common "pit"), surface cleanliness P, as well as technical requirements for the connection (thermal, mechanical and chemical resistance).

One of the options for reducing the time of this technological operation is the use of two-component adhesives with high adhesion based on epoxy resin or acrylate with fast polymerization under the influence of ultraviolet radiation (for example, FEK1-15, Vitralit 1505 and 1527 Panacol) for 0.2–1 minutes [3, 4]. The third alternative and effective way to connect optical parts is to use the optical contact method (Solaris Optics) or diffuse connection [5]. However there are physical limitations of application, in particular, the difference in the thermal expansion coefficients of the mating optical materials which reduces the resistance of the connection with significant temperature drops, etc.

The purpose of the research was to increase the accuracy and productivity of the technological process of lenses gluing by improving the optical system of the control and measuring device and automating the operation of combining of lenses optical axes by introducing an electronic reference system and mechanisms for micro-movements of optical parts.

Geometric parameters that determine the centering accuracy

In the design drawings of an optical part or a glued block, the centering error is specified (Figures 1 and 2):

– positional tolerance of the center of curvature (C_B, C_M, C_H);

– the difference in thickness over the diameter of the lens (Δ) or a flat surface;

– face runout of a flat surface.

The method of lens centering by autocollimation flare is applicable for optical parts with a diameter of 3 to 150 mm.

According to the design requirements and functional purpose of the optical part, the total outer diameter of the base lens is assigned a tolerance in the range *f*6–*e*9, for the glued one – *d*10–*c*11. It is allowed to make a glued lens with a reduced nominal diameter compared to the base lens by 0.2–0.4 mm per diameter. The tolerance for decentering of the base lens is assigned more stringent than the tolerance for the glued lens. This moment is significant when the refractive index of the material of the glued lens actually coincides with the refractive index of the adhesive. As a result, the thickness of the glue can have a certain effect on the construction of the path of rays and introduce aberrations into the optical system.

The amount of decentering, determined based on the error of alignment of auto-collimation points (O_1, O_2, etc.) (Figure 3) and is calculated by the formula:

$$\Delta e_i = C_{devi} \cdot R_i / [(n_i - 1) \cdot f_i'],$$

where C_{devi} is the displacement of the nodal point from the optical axis, determined by the flare; R_i is the radius of the controlled surface; n_i is the refractive index of the material of the optical part; f_i' is the focal length of the controlled lens.

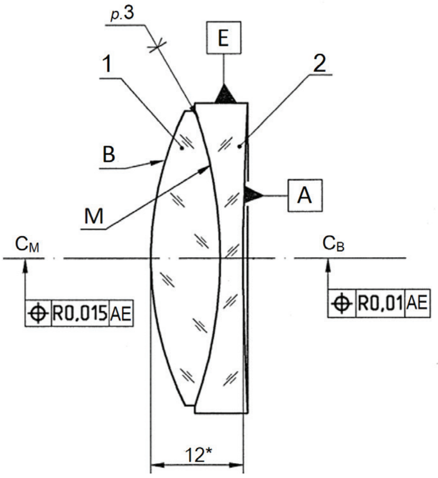

Figure 1 – Glued block of two lenses: 1 – positive meniscus; 2 – negative meniscus; A – basic supporting surface; B, M – working spherical surfaces; E – landing cylindrical surface; C_B, C_M – centers of curvature

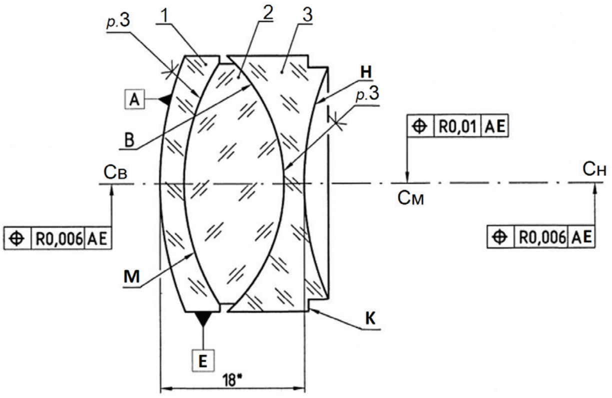

Figure 2 – Glued block of three lenses: 1 – convex-concave lens; 2 – positive meniscus; 3 – negative meniscus; A – basic supporting surface; M, B, H – working spherical surfaces; E – landing cylindrical surface; K – annular support end; C_M, C_B, C_H – centers of curvature

In accordance with ISO 10110-1, there is also a second method for estimating the amount of decentering through the angle of inclination of a separate spherical surface (γ) formed between the normal ($O_3'O_2'$) with the center of curvature O_2' and the reference axis (O_3O_2) [6, 7].

The criterion for assessing the complexity of the mechanical method of lens centering is the ratio of the clamping angle φ and decentering tolerance Δe (Table 1) [8, 9].

Figure 4 shows the sequence of transitions during centering: scheme on the left (*a*) installation of lens 3 along the main base spherical surface A on the support ring 1 and fixation along the auxiliary base cylindrical surface D in the angle 2 at an angle φ – control of decentering parameter Δe; scheme on the right (*b*) installation of lens unit 3 on a flat support surface G with control of the difference in inclination angles $\Delta\gamma$.

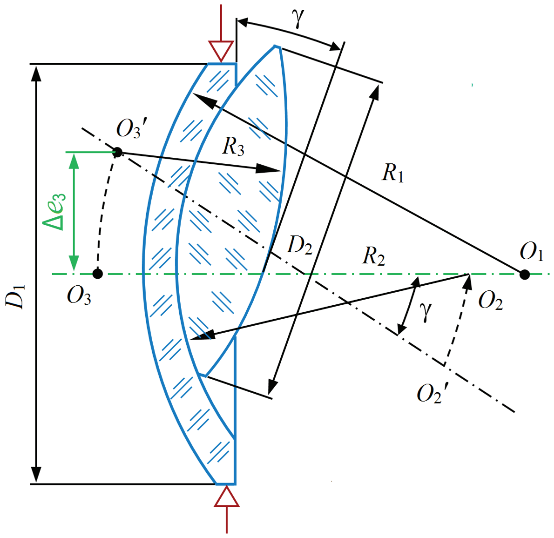

Figure 3 – The main parameters for determining the decentering

Table 1

Permissible decentering values for lenses of various optical instruments

Centering accuracy (complexity category)	Numerical tolerance value Δe	Clamping angle φ, deg.	Scope in optical devices
High (I)	0.002… 0.005 mm	<12	microscopes, photographic and projection, interferometers
Medium (II)	0.005… 0.01 mm	12–18	telescopic systems and wrapping systems
Reduced (III)	0.01… 0.02 mm	18–23	geodetic and goniometric (goniometers, levels, theodolites)
Low (IV)	0.02 and more, mm	>23	spectral, polarization, refractometric

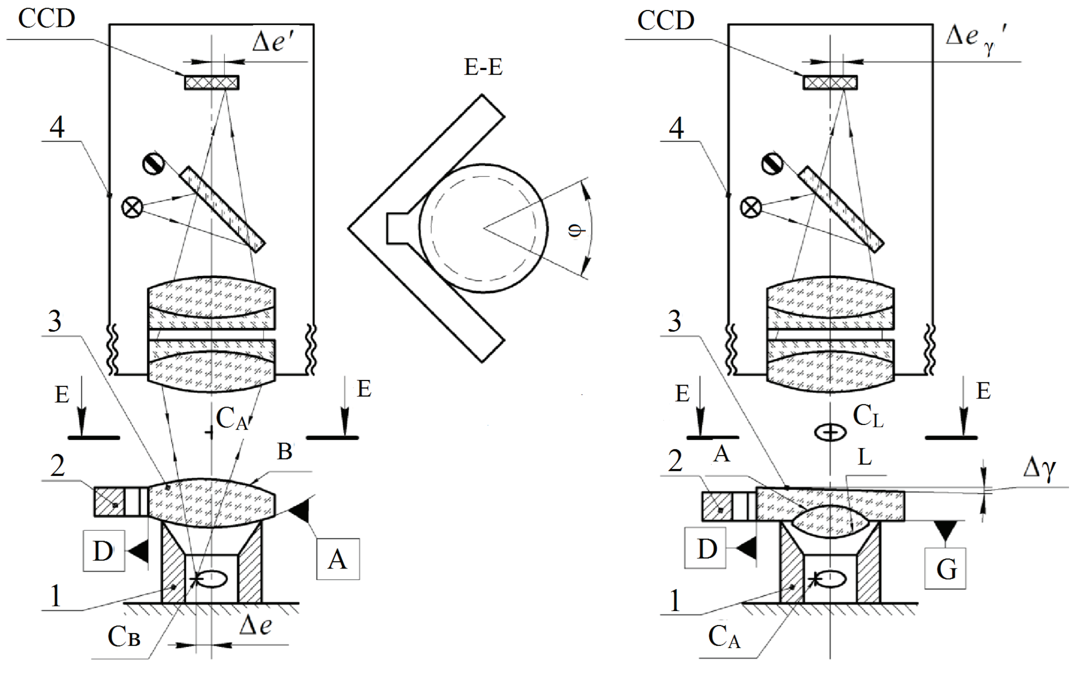

a *b*

Figure 4 – Schemes for decentering control on an optical device: a single lens in a square (*a*) and a glued block of two lenses (*b*): 1 – support ring; 2 – square; 3 – lens or lens gluing; 4 – autocollimation microscope; Δ*e* – decentering on the optical part; Δ*e′* – the amount of decentering on the CCD site; Δγ – the difference in inclination angles; φ – clamping angle; A, D, G – basic surfaces; B, L – working spherical surfaces

Method and technological features of gluing lens blocks

Under production conditions, a control series of experiments was carried out to connect and control the decentering of glued components from two and three lenses (Figures 1 and 2, respectively) with the technical parameters indicated in Table 2.

Table 2

Structural and optical parameters of lenses (mm) for a glued block

Detail	f'	n	R_1	R_2	D_1	D_2
Bonded block of two lenses						
lens 1	38.86	1.65844	43.25	–57.81	38	38
lens 2	–65.5	1.80518	–57.81	682.3	38	40
Bonded block of three lenses						
lens 1	–118.2	1.75513	42.27	27.88	32	30.2
lens 2	24.6	1.53996	27.88	–21.58	30	30
lens 3	–17.1	1.78472	–21.58	36.39	32	29

The technological operation of gluing the lenses is performed in a horizontal position for the convenience of fixing and centering the assembly in the ring fixture. As a base part, as a rule, a negative lens 2 (Figure 1) or 1 (Figure 2) is chosen, since its concave surface M is better suited for the subsequent application of a drop of glue. In addition, for ease of fastening, the base part must have a large thickness along the edge (surface E). A drop of glue, such as Norland 61, is applied to the center of the spherical surface. Next, an attachable positive lens is installed on top, the glue is evenly squeezed out from the center to the edge and preliminarily illuminated with a UV lamp for 1–2 minutes. There is a partial harde-ning of the glue, but with the possibility of a slight transverse movement of the lenses between themselves. Next, the autocollimation points O_1 and O_3' ($\Delta e_3 \rightarrow 0$) are aligned (Figure 3) by visual control on the ST-41 device. The beating diameter of the autocollimation point is equal to the fourfold decentering $D_i = 4\ C_{devi}$. The division value of the rectangular scale of the grid is 3 µm, so the measurement accuracy of the device is 1.5 µm. Figure 5 shows two positions of the light-emitting diode (LED) mark relative to the crosshair of the autocollimator, the initial one – before the alignment process (*a*) decentering $\Delta e = 2$ μm, and the final one – after alignment (*b*) the alignment accuracy $\Delta e \approx 0.5$ μm.

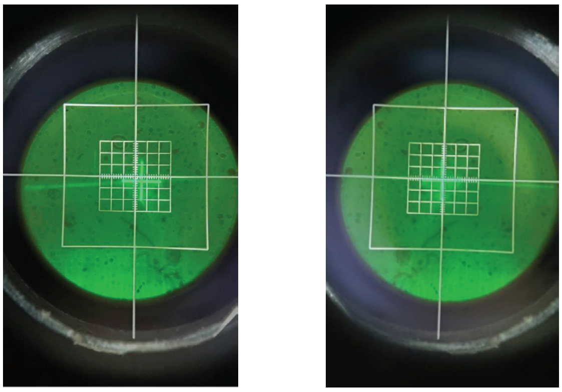
a *b*

Figure 5 – The position of the laser mark relative to the crosshairs of the autocollimator: initial (*a*) and final (*b*)

When gluing a block of three components (Figure 2), at the second stage, a change in technological bases occurs. The surface H of the negative meniscus 3 is used as the base support surface. Glue is applied to the inner spherical surface B, and the ready-made gluing of lenses 1 and 2 is installed on top. Next, the value of the angle γ for the base surface A is recalculated depending on R relative to the support surface H and auxiliary base surface E.

In both cases, after alignment, the final fixation of the lens block is carried out in 3–4 iterations with a UV lamp for 10 min with an interval of 10 min.

After hardening of the glued joint, the total error N of Newton's interference rings on the outer working spherical surfaces of the parts (A and B for two-component gluing or A and H for three-component gluing) may increase due to the drying of the glue and deformation of the edge zones.

Control and measuring equipment

The classic autocollimation microscope ST-41 was built according to the optical scheme of A.A. Zabelin (Figure 6) and allows you to combine the point image of your source with the autocollimation point of a spherical surface, which gives an image of the source placed in it reflected from the surface in the same plane where it is located [10]. The degree of non-coincidence is equal to twice the amount of decentering, and the rotation of the lens allows you to double its value. If a concave surface is controlled, then the autocollimation point coincides with the center of its curvature, for a convex one, it is necessary to calculate its distance from the surface.

The basic optical system of the ST-41 device uses two interchangeable lenses 1 and 2 with focal length $f' = 201.76$ mm and $f' = 400.1$ mm. The illumination source is a low-power incandescent lamp RN8-20. The autocollimating crosshair is formed on an inclined grid 3, which introduces astigmatism. As a result, in the field of view of the symmetrical eyepiece 7 and 8, the image of the crosshair at the edges looks fuzzy.

In order to improve the image quality of the reference elements and the accuracy of decentering measurement, the optical system of the ST-41-01 device was improved (Figure 7). To ensure the versatility of measurements of glued lenses with different focal lengths, a movable 4-component short-focus lens 1 ($f' = 40.56$ mm) is installed with the possibility of linear movement along the optical Z axis and fixation in specified positions graduated scale ($E = 8.42$–53.08 mm). Grid 7 with a crosshair is installed perpendicular to the optical axis, which ensures its uniform illumination over the entire field of view from a three-component 4-lens condenser 8 and a high-power white light LED (type XREWHT-LI-0000-00001) or LUXEON (LXML-PM01-0100). The convergence of the visual and lighting channels is carried out by means of a cube-prism 2.

In order to reduce the decentering measurement error, the new version of the optical system of the device also provides for the separation of the output observation channel into a visual channel through a symmetrical eyepiece 6 and a television channel (image plane on the CCD array area) using a beam-splitting cube prism 4.

An improved version of the design of the ST-41-01 control and measuring device is shown in Figure 8.

A vertical stand 2 and an object table 5 are rigidly fixed on the adjusted horizontal base 1. An angle 6 is installed on the round table 5, which holds the frame with the base optical part or the optical part itself separately. In the process of alignment of autocollimation points, the table has the possibility of circular movement due to the support screws 7, which provide the possibility of exposing the base surface to a horizontal position. Focusing of the autocollimating microscope 4 is carried out due to the smooth vertical and rectilinear movement of the arm 3 along the trapezoidal thread of the stand 2. The arm has a unit with screws for micro-movements 8, which allows the optical axis of the microscope to be aligned with the axis of rotation of the stage with the support ring. As a source for illumination of the crosshairs in an autocollimation microscope, an emitter 9 is used – an LED with the possibility of longitudinal and transverse movement within ±0.5 mm. Observation of the autocol-limation image of the crosshairs on the microscope grid can be carried out by the operator's eye through the eyepiece 10 or broadcast by a high-resolution black-and-white television camera 11 (VBC-751) to a personal computer monitor.

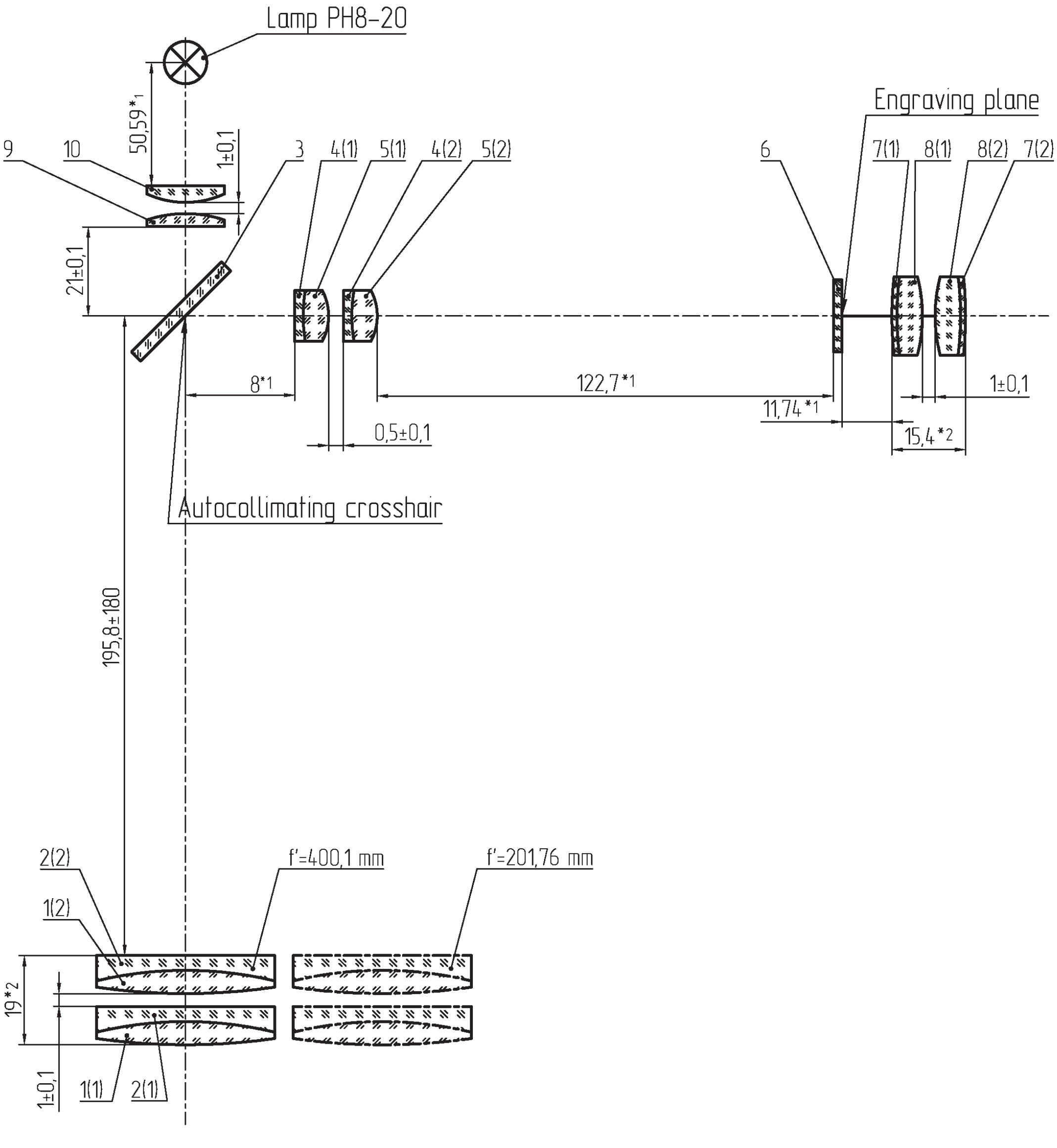

Figure 6 – Schematic optical diagram of the classic device ST-41: 1 and 2 – double lens block of the teleobjective; 3 – grid with crosshairs; 4 and 5 – double lens block of the microobjective; 6 – measuring grid; 7 and 8 – lens blocks of a symmetrical eyepiece; 9 and 10 – condenser lenses

The image receiver in the television camera is a CCD matrix model SONY ICX-409AL, Super-Had, 1/3 inch format with the number of active elements 752 (horizontal)×582 (vertical). The high resolution of the optical system is ensured by the small pixel size of the CCD 6.5×6.25 μm.

The next step in improving the accuracy of connecting optical components and eliminating the influence of the subjective human factor when measuring decentering was the creation of an automated control system for the process of bringing together autocollimation points in the ST-41-M2 device and the gluing process.

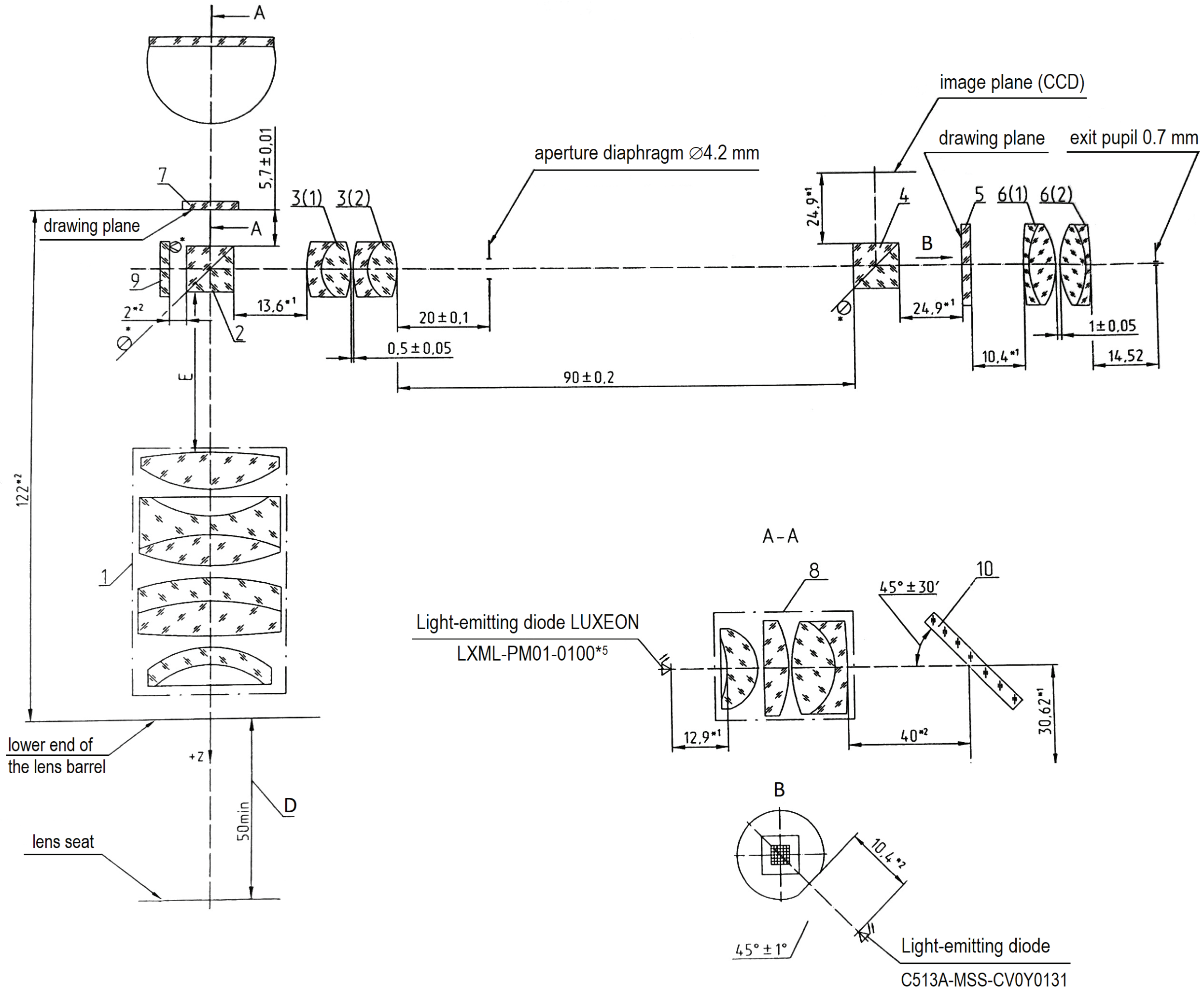

Figure 7 – Schematic optical diagram of a new version of the ST-41-01 device: 1 – 4-component telephoto lens; 2 and 4 – cube-prism beam splitters; 3 – double lens block of the microobjective; 5 – measuring grid; 6 – lens blocks of a symmetrical eyepiece; 7 – grid with a crosshair; 8 – condenser lenses; 9 and 10 – mirrors

Using software methods, an electronic grid template is created, which is also displayed on the monitor screen (Figure 8). The image of autocollimation points is projected onto the area of the CCD matrix. Both images are combined. Next, the coordinates of the points of the circle of maximum rotation of the crosshair along the *X* and *Y* axes are determined. Taking into account the decentering value $2\Delta e$, a corrective control voltage is applied to motorized linear translators (for example, 8MT167-25 Standa), which move the pushers holding the positive lens to be glued until the autocollimation image of the crosshair completely coincides with the center O on the electronic grid (Figure 9).

The mathematical apparatus for solving this problem is based on a combination of two methods of “least squares” and “successive approximation”.

To achieve a given calculated decentering value, it is necessary to ensure the following ratio:

$$C = \frac{2\Delta e}{4\beta_{m.ob.3} \cdot \beta_{ob.1}},$$

where C is the decentering value for the controlled spherical surface, specified in the working drawing, mm (Figure 1); $\beta_{m.ob.3}$ 8× – magnification of the microlens 3 (Figure 7); $\beta_{ob.1}$ is variable magnification of lens 1 (Table 3).

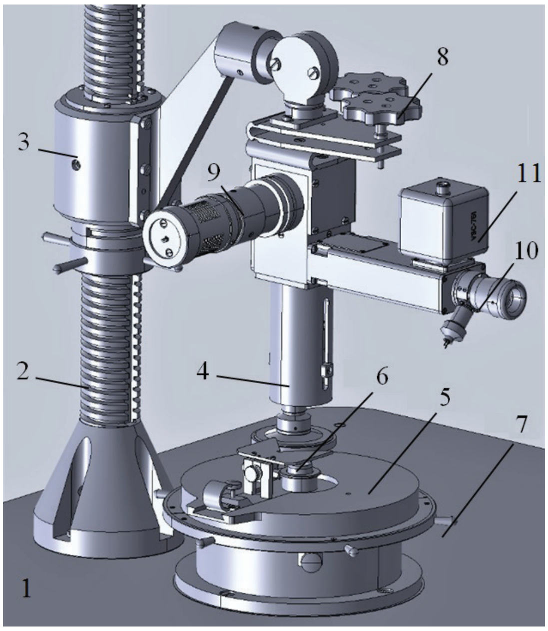

Figure 8 – Device for controlling the gluing of lenses model ST-41-01: 1 – base; 2 – rack; 3 – bracket; 4 – microscope; 5 – table; 6 – square; 7 – support screws; 8 – screws for micro-movements; 9 – light-emitting diode; 10 – eyepiece; 11 – television camera

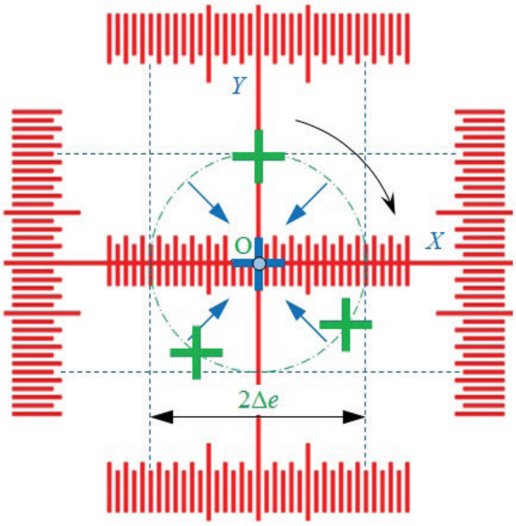

Figure 9 – Drawing of an electronic measuring grid

Specialized software has been developed for automatically bringing the position of the autocol-limation crosshair to the center of the measuring scale of the grid.

During the gluing process, the beating value of the autocollimating crosshair (2Δ*e*) is preliminarily recorded in a video fragment with the FSP option to be adjusted. A previously generated video file can also be uploaded through the "Video options" menu (Figure 10). To determine the extreme points of the circle, the "screenshot" button SCR is provided. The color, as well as the number of vertical (V1, V2) and horizontal (H1, H2) strokes of the electronic grid is configured through the "Lines Operation" menu (Figure 11).

Table 3

Correspondence of the division value of the electronic grid and the scale of the lens 1 at various magnifications β

Division value, µm	*E* ± 0.05 mm	*L*, cm	β_{ob}, multiple
3.5	53.08	5.30	–0.893
5	42.22	6.16	–0.625
6	37.99	7.04	–0.521
8	32.71	9.11	–0.391
10	29.54	11.38	–0.313
12	27.43	13.77	–0.260
15	25.32	17.45	–0.208
20	23.20	23.73	–0.156
50	19.40	62.28	–0.063
15.4"	16.87	–	–
40	13.70	–55.09	0.078
30	12.64	–42.22	0.104
23	11.36	–33.26	0.136
15	8.42	–23.17	0.208

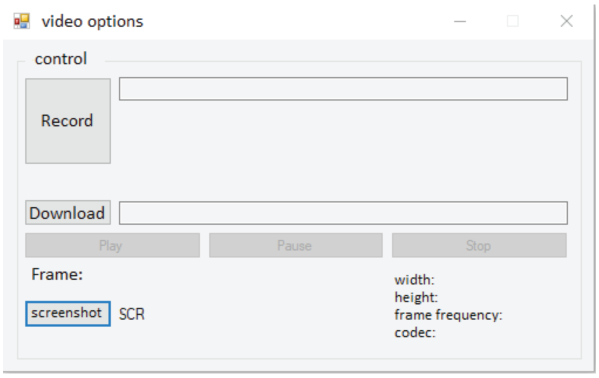

Figure 10 – The working window of the software "Video options"

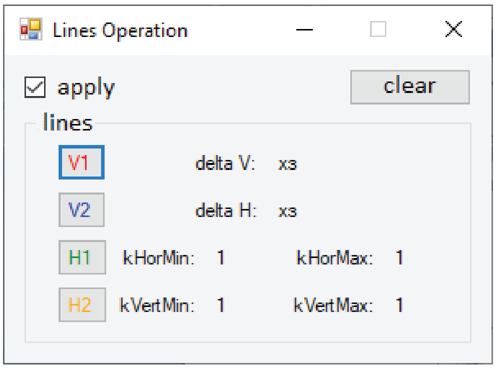

☑ apply

delta V: x3

delta H: x3

kHorMin: 1 kHorMax: 1

kVertMin: 1 kVertMax: 1

Figure 11 – The working window of the software “Lines Operation”

Conclusion

It has been established that, subject to a number of technological transitions and the accompanying control of geometric parameters, it is possible to achieve the eccentricity of the crosshairs of the combined optical axes of the glued lenses at the level of 5 µm (complexity category *I*).

The use of a movable lens with variable magnification expands the functionality of the ST-41-01 device when monitoring the decentering of parts with spherical surfaces in the range of diameters from 3 to 100 mm and curvature radii from 3 to 200 mm.

The introduction of an automated control system for the process of convergence of autocollimation points in the device model ST-41-M2 makes it possible to exclude the subjective influence of the operator when assessing the accuracy of measuring the decentering of glued optical parts and provides a shift value of 0.1 µm.

References

1. Ruggedization of Imaging Lenses. Edmund Optics, Inc. Whitepaper. Section 5.3 of the Imaging Resource Guide – 2017. Access mode: www.edmundoptics.com/know-ledge-center/application-notes/imaging/ruggedization-of-imaging-lenses/

2. Patrik Langehanenberg, Josef Heinisch, Christian Buß, Christian Wilde. High-Precision Mounted Lens Production. WILEY-VCH Verlag GmbH & Co. KGaA, Weinheim, *Optik&Photonik*, 2/2014, pp. 41–45.
DOI: 10.1002/opph.201400045

3. The Bonding of Optical Elements Techniques and Troubleshooting. Summers Optical. A Division of EMS Acquisition, Inc. PO Box 380 – 1560 Industry Road Hatfield, PA 19440.

4. Krithika S. Prabhu, Tony L. Schmitz, Peter G. Ifju, John G. Daly. A Survey of Technical Literature on Adhesive Applications for Optics. *New Developments in Optomechanics*, ed. by Alson E. Hatheway, Proc. SPIE 6665, 2007, 0277-786X/07/$18.
DOI: 10.1117/12.735948

5. Optical bonding techniques – Review. *Solaris Optics*, 20.07.2020. Available at: https://solarisoptics.eu/optical-bonding-techniques-review/

6. Jim H. Burge. Mounting of Optical Components. Mounting of lenses. *Optical Sciences and Astronomy*. The University of Arizona, Tucson, 2011, 46 p.

7. Frederic Lamontagne, Ulrike Fuchs, Martin Trabert, Anna Mohl. Aspheric lens mounting. *Optical Engineering*, 2018, vol. 57, no. 10, p. 101708.
DOI: 10.1117/1.OE.57.10.101708

8. Bui Dinh Bao, Beloyvan P.A., Latiev S.M., Tabachkov A.G. Centering of stacked lenses. *Modern problems of science and education*, 2015, no. 1 (part 1), 20 p. Access mode: science-education.ru/ru/article/view?id=17909

9. Bui Dinh Bao, Latiev S.M., Namesake R. Automation of lens centering when pasting into frames. *Scientific and technical bulletin of information technologies, mechanics and optics*, 2015, vol. 15, no. 6, pp. 1030–1035.
DOI: 10.17586/2226-1494-2015-15-6-1030-1035

10. Patent RU 2560920. Device for locating lenses in cylindrical frames when measuring decentering of their optical surfaces. Appl. 11/18/2013. Published 08/20/2015. Bull. No. 23.

Analysis of Illumination Generated by LED Matrices Distribution

P.S. Bogdan, E.G. Zaytseva, P.O. Baranov, A.I. Stepanenko

Belarusian National Technical University,
Nezavisimosty Ave., 65, Minsk 220013, Belarus

Received 11.02.2022
Accepted for publication 18.03.2022

Abstract

Creation of indoor lighting systems with the possibility of changing its parameters in space and time is a promising direction within the framework of the intellectual environment system. The aim of this work was to create a methodology for calculating the illumination created by LED matrices which does not require the use of specialized software products and is adapted to the possibility of varying the parameters of LEDs and illuminated rooms.

The urgency of creating a room lighting system that simulates the conditions of natural lighting taking into account the need to change its spectral composition in time, in space taking into account the physical and psychological state of a person is substantiated. The possibility of using well-known computer programs to calculate the distribution of illumination in the room is analyzed.

A method has been developed for calculating the distribution of illumination on a plane using both a flat LED matrix and a matrix with an inclined arrangement of the planes of individual LEDs. It is shown that the distribution of illumination is a function of the indicatrix of the light intensity of the LED, its location in space, the number of LEDs in the matrix.

Illumination distribution has been calculated for various light sources consisting of RGB LEDs both for desktop and ceiling lighting was calculated. It is established that when using matrices containing the same LEDs distribution of illumination is very nonuniform. The inclined arrangement of LED planes slightly increases uniformity reducing the maximum illumination. For ceiling lighting the option of uniform distribution of LEDs within the ceiling plane provides more uniform illumination than when the same number of LEDs are arranged in groups of matrices.

Results of LED sources modeling indicate the need to modernize simple orthogonal matrices containing the same type of elements with the same power modes for all elements in order to increase the uniformity of illumination and efficiency. Such modernization can be carried out by changing the geometry of matrices differentiating the power modes of individual LEDs. The developed calculation program can be supplemented with options for introducing the above changes, as well as options for analyzing the spectral distribution of light in space.

Keywords: mathematical modeling, RGB LED, light intensity distribution indicatrix, led matrix, illumination distribution.

DOI: 10.21122/2220-9506-2022-13-1-60-67

Адрес для переписки:
Зайцева Е.Г.
Белорусский национальный технический университет,
пр-т Независимости, 65, г. Минск 220013, Беларусь
e-mail: egzaytseva@bntu.by

Address for correspondence:
Zaytseva E.G.
Belarusian National Technical University,
Nezavisimosty Ave., 65, Minsk 220013, Belarus
e-mail: egzaytseva@bntu.by

Для цитирования:
P.S. Bogdan, E.G. Zaytseva, P.O. Baranov, A.I. Stepanenko.
Analysis of Illumination Generated by LED Matrices Distribution.
Приборы и методы измерений.
2022. – Т. 13, № 1. – С. 60–67.
DOI: 10.21122/2220-9506-2022-13-1-60-67

For citation:
P.S. Bogdan, E.G. Zaytseva, P.O. Baranov, A.I. Stepanenko.
Analysis of Illumination Generated by LED Matrices Distribution.
Devices and Methods of Measurements.
2022, vol. 13, no. 1, pp. 60–67.
DOI: 10.21122/2220-9506-2022-13-1-60-67

Приборы и методы измерений
2022. – Т. 13, № 1. – С. 60–67
P.S. Bogdan et al.

Devices and Methods of Measurements
2022, vol. 13, no. 1, pp. 60–67
P.S. Bogdan et al.

Анализ распределения освещённости, генерируемой светодиодными матрицами

П.С. Богдан, Е.Г. Зайцева, П.О. Баранов, А.И. Степаненко

Белорусский национальный технический университет,
пр-т Независимости, 65, г. Минск 220013, Беларусь

Поступила 11.02.2022
Принята к печати 18.03.2022

Создание систем освещения помещений с возможностью изменения его параметров в пространстве и во времени является перспективным направлением в рамках системы «интеллектуальная окружающая среда». Целью данной работы было создание методики расчёта освещённости, создаваемой светодиодными матрицами, которая не требует применения специализированных программных продуктов и адаптирована к возможности варьирования параметров светодиодов и освещаемых помещений.

Обоснована актуальность создания системы освещения помещений, имитирующей условия естественного освещения с учётом необходимости его изменения по спектральному составу во времени, в пространстве с учётом физического и психологического состояния человека. Проанализирована возможность использования известных компьютерных программ для расчёта распределения освещённости в помещении.

Разработана методика расчёта распределения освещённости на плоскости при использовании как плоской светодиодной матрицы, так и матрицы с наклонным расположением плоскостей отдельных светодиодов. Показано, что распределение освещённости является функцией индикатрисы силы света светодиода, расположения его в пространстве, количества светодиодов в матрице.

Произведён расчёт распределения освещённости для различных источников света, состоящих из RGB светодиодов, как для настольного, так и для потолочного освещения. Установлено, что при использовании матриц, содержащих одинаковые светодиоды, велика неравномерность распределения освещённости. Наклонное расположение плоскостей светодиодов незначительно увеличивает равномерность, уменьшая максимальную освещённость. Для потолочного освещения вариант равномерного распределения светодиодов в пределах потолочной плоскости обеспечивает более равномерное освещение, чем при расположении такого же количества светодиодов в виде групп матриц.

Результаты моделирования светодиодных источников свидетельствуют о необходимости модернизации простых ортогональных матриц, содержащих однотипные элементы с одинаковым для всех элементов режимом питания, с целью повышения равномерности освещённости и экономичности. Такая модернизация может осуществляться за счёт изменения геометрии матриц, дифференциации режимов питания отдельных светодиодов. Разработанная программа расчёта может дополняться опциями для введения перечисленных выше изменений, а также опциями для анализа спектрального распределения излучения в пространстве.

Ключевые слова: математическое моделирование, RGB светодиод, индикатриса распределения силы света, светодиодная матрица, распределение освещённости.

DOI: 10.21122/2220-9506-2022-13-1-60-67

Адрес для переписки:
Зайцева Е.Г.
Белорусский национальный технический университет,
пр-т Независимости, 65, г. Минск 220013, Беларусь
e-mail: egzaytseva@bntu.by

Address for correspondence:
Zaytseva E.G.
Belarusian National Technical University,
Nezavisimosty Ave., 65, Minsk 220013, Belarus
e-mail: egzaytseva@bntu.by

Для цитирования:
P.S. Bogdan, E.G. Zaytseva, P.O. Baranov, A.I. Stepanenko.
Analysis of Illumination Generated by LED Matrices Distribution.
Приборы и методы измерений.
2022. – Т. 13, № 1. – С. 60–67.
DOI: 10.21122/2220-9506-2022-13-1-60-67

For citation:
P.S. Bogdan, E.G. Zaytseva, P.O. Baranov, A.I. Stepanenko.
Analysis of Illumination Generated by LED Matrices Distribution.
Devices and Methods of Measurements.
2022, vol. 13, no. 1, pp. 60–67.
DOI: 10.21122/2220-9506-2022-13-1-60-67

Introduction

Lighting has a significant effect on the human body. According to [1] light radiation determines many physiological and behavioral reactions ranging from hormonal rhythms and pupil reactions, ending with sleep, alertness, cognitive abilities and mood. In particular, it was found [2] that patients who experienced a stay of at least 48 hours in an intensive care unit without windows had a disturbed idea of the duration of their stay in the department and their orientation in time worsened, as well as the frequency of hallucinations and delusions increased more than 2 times compared to patients in similar departments with translucent windows. To eliminate these phenomena, the authors [2] proposed using a system to simulate the daily cycle of natural light in a medical hospital. Since natural lighting is not always optimal for human life (seasonal changes in the duration of daylight, individual characteristics and preferences of a person), the urgency of creating a combined (natural and artificial lighting) system is obvious, which should quickly adapt to both changes in the natural component and individual characteristics and preferences of a person.

The parameters of the lighting system elements must comply with regulatory documents and comfort conditions. The requirements for lighting and radiation sources are set out in regulatory documents[1–3]. The main normalized parameters are illumination and its uniformity in space. In addition, in the standard[3] of the Association of Manufacturers of LEDs and systems based on them, the criterion for choosing parameters is the comfort of the light environment for different age groups, taking into account the need to change these parameters over time. Hence, the need to develop adaptive lighting systems is obvious, and the change in illumination in space should be determined by the age of a person, as well as his physical and psychological state. Therefore, the lighting system must contain not only the source itself, the power supply circuit, the unit for measuring the parameters of the natural component of lighting, but also devices for monitoring the human condition, appropriate software.

To the greatest extent, the adaptability requirement is satisfied by LED light sources, whose brightness and spectral composition are quite easy to control. Their important advantage is also the low power consumption. At the same time, the use of LEDs as light sources revealed two significant drawbacks: the small angular size of the light beam and the excessive brightness when the source enters the field of view. To get rid of these shortcomings, optical elements (lenses, reflectors [3–8]) and scattering filters [9] are used in the lighting device. A large number of proposed architecture options for LED lighting systems complicates the process of optimal selection of lighting systems, taking into account compliance with the requirements of current standards and the need for dynamic lighting. Therefore, for such optimization, it is necessary to be able to computer simulate the distribution of illumination in the room in the function of the LED radiation indicatrix and the coordinates of its placement in the room.

Currently, several packages of computer calculation of optical system parameters are used: Zemax, Code V, Oslo, DEMOS, SARO, OPAL, etc., the advantages and problems of their application are given in [10]. Some of them are focused on foreign element base, norms and standards, the main purpose of these programs is modeling and analysis of various optical systems. In [11], optimization of secondary lenses for LED lamps is performed using ray tracing using the Monte Carlo method without image processing. A program has been developed using the particle swarm algorithm (PSO) in order to optimize the layout of lamps for the general lighting scheme of premises [12]. The last two methods are closer to solving the problem of optimal illumination, but the algorithms used in them are quite complex and require significant technical resources. The aim of the work was to create a methodology for calculating the illumination created by LED matrices, which does not require the use of specialized software products and is adapted to the possibility of varying the parameters of LEDs and illuminated rooms.

Mathematical modeling of the illumination distribution generated by the LED matrix

As the initial data for calculating the illumination on the plane, the light intensity distribution of the source, the coordinates of the source relative to

---

[1] GOST ISO 8995-2002. Principles of visual ergonomics. Lighting of working systems indoors (in Russian).

[2] GOST R 55710-2013. Lighting of workplaces inside buildings. Norms and measurement methods (in Russian).

[3] STO. 69159079-05-2020. LED lighting devices. Requirements for a comfortable light environment (in Russian).

the plane are used. The result of the calculation is the dependence of the illumination on the plane as a function of its orthogonal x and y coordinates.

Let us first consider the location of the source A relative to the illuminated plane P, when the axis of symmetry of the indicatrix $A0$ is perpendicular to the plane P (Figure 1).

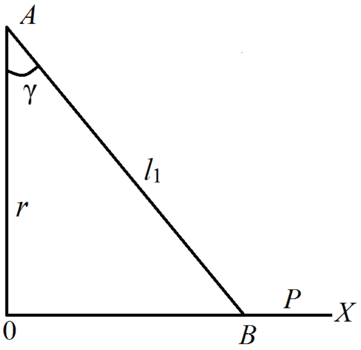

Figure 1 – Scheme for the transition to the dependence of illumination on the spatial coordinate x in the plane P

The ray of the indicatrix in the plane $A0X$, directed to the axis of the indicatrix at an angle γ, intersects the illuminated plane at point B. In accordance with the Methodological Guide[4] for the design of artificial lighting of public and residential buildings, the illumination E_B of point B on the illuminated plane P depends on the angle γ between the perpendicular to the plane P, the direction of the light beam from the source at point A and the distance l_1 between points A and B:

$$E_B = \frac{I(\gamma)}{l_1^2}\cos\gamma. \tag{1}$$

Expression (1) can be used for calculations in the case of a perpendicular arrangement of the axis of the light intensity of the LED relative to the illuminated plane. But when choosing the optimal arrangement of the LEDs in the lighting device, an inclined position of the axis of the indicatrix relative to the illuminated plane is also possible. In Figure 2 the axis of the LED's indicatrix forms angles φ_x and φ_y with a perpendicular to the illuminated plane $x0y$ in the planes $z0x$ and $z0y$, respectively.

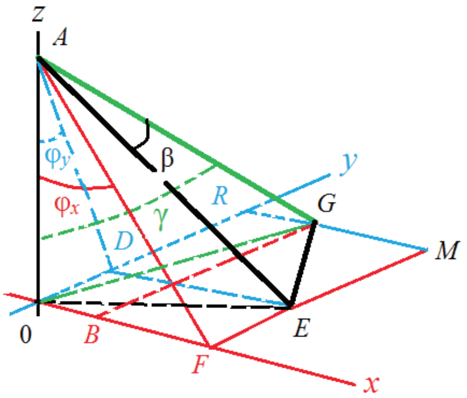

Figure 2 – The direction of light rays at an inclined position of the AE axis of the light intensity indicatrix relative to the illuminated plane $x0y$

In this case, the distribution of illumination on the illuminated plane $x0y$ is a function of the angle β of the inclination of the beam AG to the axis AE of the symmetry of the light intensity indicatrix for the LED, the angle of inclination γ of the beam AG to the perpendicular $A0$ to the illuminated plane $x0y$. The specified dependency has the form:

$$E(\beta,\gamma) = \frac{I(\beta)\cos\gamma}{l_1^2}, \tag{2}$$

where $I(\beta)$ is dependence of the intensity of the angle β of inclination of the beam AG to the axis AE of symmetry of the indicatrix; l_1 is the length of the path of the light beam from the LED to the illuminated surface.

Let's move from the distribution of illumination in the function of the angles β and γ to the distribution in the function of the coordinates x_G and y_G of the points of the illuminated surface and the distance r between the LED at point A and the illuminated plane $x0y$.

From the triangles $A0G$ and EAG it is obvious that:

$$\gamma = \operatorname{arc\,tan}\frac{\sqrt{x_G^2 + y_G^2}}{r}; \tag{3}$$

$$\beta = \arccos\frac{r + x_G\tan\phi_x + y_G\tan\phi_y}{\sqrt{r^2 + (x_G)^2 + (y_G)^2}\sqrt{1 + (\tan\phi_x)^2 + (\tan\phi_y)^2}}; \tag{4}$$

$$l_1 = AG = \sqrt{r^2 + (x_G)^2 + (y_G)^2}. \tag{5}$$

Taking into account the expressions (3, 4, 5), the formula (2) for calculating illumination will take the form:

---

[4] Design of artificial lighting of public and residential buildings. Methodical manual. Ministry of Construction and Housing and Communal Services of the Russian Federation. Federal Center for Standardization, Standardization and Conformity Assessment in Construction. Moscow, 2016, 141 p. Access mode: https://www.faufcc.ru/upload/methodical_materials/mp15.pdf. Date of access: 28.01.2022 (in Russian).

$$E(x,y,\phi_x,\phi_y)=\frac{I\left(\arccos\dfrac{r+x_G\tan\phi_x+y_G\tan\phi_y}{\sqrt{r^2+(x_G)^2+(y_G)^2}\,\sqrt{1+(\tan\phi_x)^2+(\tan\phi_y)^2}}\right)\cos\left(\arctan\dfrac{\sqrt{(x_G{}^2+y_G{}^2}}{r}\right)}{r^2+(x_G)^2+(y_G)^2}. \qquad (6)$$

As a rule, not one source is used for lighting, but a matrix of LEDs. In this case, it is necessary to sum up the illumination values calculated for each LED, taking into account their displacement relative to each other.

Examples of using the developed mathematical model to calculate the distribution of illumination generated by LED matrices

Illumination in the premises is regulated by regulatory documents. For example, in accordance with GOST R 55710[2], workplaces with video terminals on a given surface, as well as those intended for writing, typing, reading, and data processing, should have an illumination of 500 lux with an illumination uniformity of 0.6, and canteens – 200 lux with a uniformity of 0.4.

Using the developed mathematical model, lighting modeling was carried out for the two above options, and the distance between the LED matrix and the illuminated surface in the first case was assumed to be 0.5 m (table lamp), in the second case 2.5 m (ceiling lamp). For the calculation, the indicatrices of the components of the COTCO three-crystal RGB-SMD LED L1-P1-01 TQ with a delta-shaped arrangement of crystals inside the case were used, shown in Figure 3 [13].

The introduction of information about the graphs in Figure 3 in numerical form into the calculations involves the use of two options. First, it is possible to apply approximations of the form:

$$I=d(\cos\beta)^n, \qquad (7)$$

where I is the value of the luminous intensity, cd; β is the angle between the perpendicular to the illuminated surface and the direction of the light beam on the indicatrix, deg; d is the value of the luminous intensity at β equal to 0, n is the exponent.

Selecting the parameter n for the different parts of the indicatrix, it is possible to obtain a sufficiently high accuracy of the approximation, for example, for the blue led when maximum n is equal to 1 for all β, the relative error was 0.07 % (Figure 4).

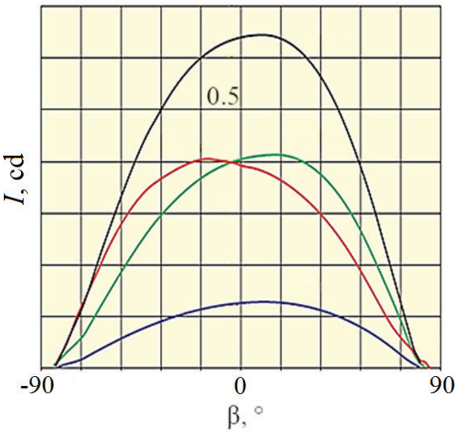

Figure 3 – The indicatrix of the light intensity I as a function of the angle β between the perpendicular to the illuminated surface and the beam direction for the three-crystal RGB-SMD LED LM1-TPP1-01 TTQ for total inclusion in white balance mode (black upper graph), for red, green, blue components (respectively red, green, blue graphs) [13]

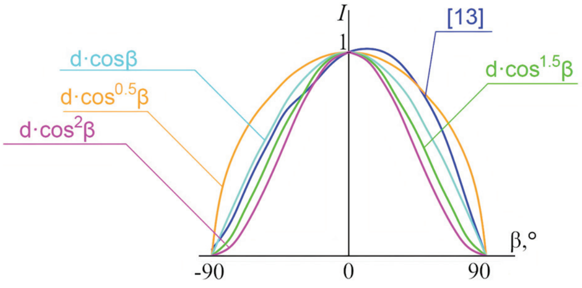

Figure 4 – The indicatrix of the luminous intensity I in relative units as a function of the angle β between the perpendicular to the illuminated surface and the beam direction for the blue component of the RGB-SMD LED LM1-TPP1-01 TTQ [13] and its approximation by formula (7) for different exponents

The second option for introducing the indicatrix in numerical form is to use the method of spline approximation by the pspline and interp functions in Mathcad packages, where the entered numerical values are connected by straight segments. In this case, the deviation of the actual and calculated values is practically reduced to zero, the error between the entered values depends on their number, the approximation formula is not presented in an analytical form. Figure 5 shows a graph of such an approximation and the actual values for the light intensity curve of the blue component of the LED LM1-TPP1-01 TTQ. The second option is more preferable due to less labor intensity.

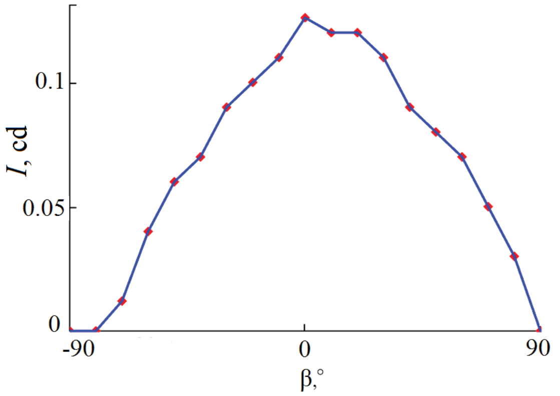

Figure 5 – The light intensity indicatrix *I* as a function of the angle β between the perpendicular to the illuminated surface and the beam direction for the blue component of the RGB-SMD LED LM1-TPP1-01 TTQ [13] (red icons) and its approximation using the Mathcad package (blue line)

The maximum illumination of the plane is a function of the number of LEDs in the matrix. In order to determine the required number of LEDs in the matrix to provide the required illumination for a table lamp and a ceiling lamp, the corresponding dependencies were obtained for both cases. The LEDs were arranged orthogonally in 9 mm steps. Calculations have shown that these dependencies are linear in nature and differ in the angle of inclination of the straight line to the horizontal axis.

Based on the comparison of the illumination values regulated by GOST R 55710[2] for some types of activities of 500 lux (table lamp) and 200 lux (ceiling lamp) with the obtained dependencies, square matrices of 12 × 12 and 40 × 40 LEDs were selected for further calculations. For these matrices, the dependences of illumination on the plane on spatial coordinates are calculated by formula (6). The corresponding graphs of the dependence of the illumination *E* on the *x* coordinate are shown in Figures 6 (red curve) and 7 (red curve).

Analysis of the graphs in Figures 6 (red curve) and 7 (red curve) shows that the illumination varies significantly from the center to the periphery. In the first case (table lamp), in accordance with GOST R 55710[2] on a given surface uniformity of lighting should be 0.6, and the second (ceiling lamp) – 0.4. As a given surface in the first case, we consider the area of visual work, the radius *R* which is in accordance with the Methods of hygienic assessment of indicators artificial light environment in the premises of buildings and structures[5] is calculated as:

$$R = 1.2a, \tag{8}$$

where *a* is the distance from the eyes of the observer (employee) to the work surface, m.

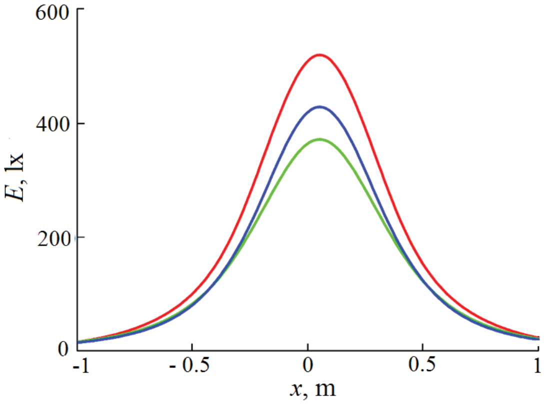

Figure 6 – Graphs of the dependence of the illumination of the *E* plane on the *x* coordinate for the distance between the matrix 12 × 12 and the plane equal to 0.5 m (table lamp): red curve for a flat matrix; blue – for a matrix with a gradual rotation of the LED planes from +45° to -45°; green – for a matrix with a gradual rotation of the LED planes from -45° to +45°

When working with the monitor, the distance to the conditional working surface is about 0.5 m, when writing, reading – about 0.4 m, then the radius of the working area is up to 0.6 m. According to the graph in Figure 6, at the boundaries of the working area, the uniformity is about 0.14, which is significantly less than the regulated value of 0.6. Therefore, it is necessary to modernize this lamp in order to increase the uniformity of illumination. This can be achieved by using more powerful LEDs on the periphery of the lamp, changing the location of the LEDs in the matrix.

To investigate the possibility of increasing the uniformity of illumination due to the rotation of the

---

[5] Methods of hygienic assessment of indicators of artificial light environment in the premises of buildings and structures. Instructions for use. Republican unitary Enterprise “Scientific and practical center of hygiene”. Reg. No. 007-1217. Minsk, 2018, 14 p. Access mode: http://med.by/methods/pdf/007-1217.pdf. Access date: 28.01.2022 (in Russian).

LEDs in the matrix, each LED was rotated relative to the plane of the matrix from one edge to the other by an increasing value with a constant step in the range from -45º to +45º in the directions along the x and y axes, as well as in the range from +45º to -45º.The calculation was performed using the expression (6) for the 12×12 matrix and the distance to the illuminated plane of 0.5 m (table lamp).

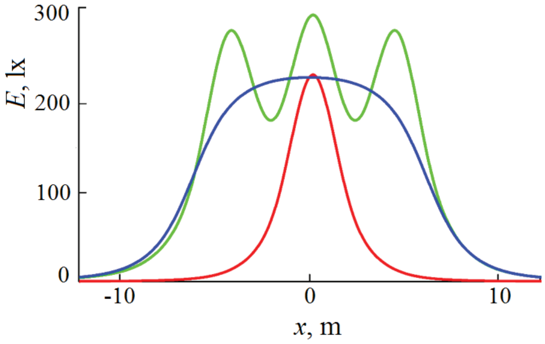

Figure 7 – Graphs of the dependence of the illumination of the E plane on the x coordinate for the distance between the matrices and the 2.5 m plane (ceiling lamp): red curve for the 40×40 matrix; green – for nine 40×40 matrices evenly spaced on the ceiling; blue – for the 120×120 matrix with a uniform step along the ceiling plane

The graphs for both rotation options are shown in Figure 6 (green and blue curves, respectively). The analysis of the graphs in Figure 6 allows us to conclude that when the planes of the LEDs are rotated, the maximum illumination decreases, and when turning from -45º to +45º more than when turning from +45º to -45º. There is no significant increase in the uniformity of illumination within the specified rotation angles. A similar result was obtained for a 40×40 ceiling lamp.

The developed methodology made it possible to analyze the possibility of increasing the uniformity of illumination due to the use of several LED matrices. For a table lamp, the illumination distribution was calculated using three 12×12 matrices located at the vertices of an equilateral triangle with a side of 0.5 m. The graph of the dependence of the illumination E on the x coordinate passing through the vertex of the triangle and the middle of its opposite side is shown in Figure 8 (red curve). The analysis of this graph shows that such a three-matrix option increases the uniformity of illumination, but the required uniformity value is still not achieved. At the same time, the maximum illumination increases and the power consumption increases three times.

The use of a square matrix with a total of 288 LEDs and an “empty square” 6×6 inside (Figure 8, green curve) has the same disadvantages as the previous version.

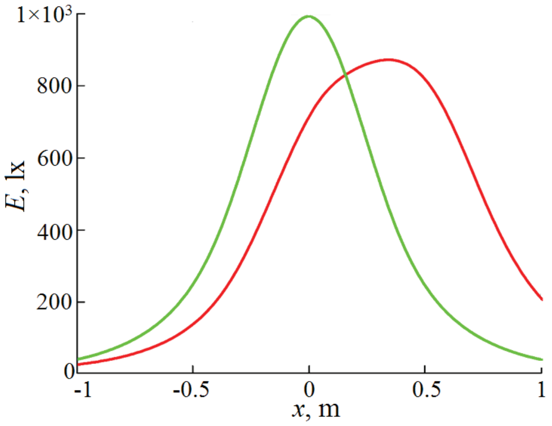

Figure 8 – Graphs of the dependence of the illumination of the E plane on the x coordinate for the distance between the matrices and the plane of 0.5 m (table lamp): red curve for three 12×12 matrices located at the vertices of an equilateral triangle with a side of 0.5 m; green curve for a square matrix of 288 LEDs with an “empty square” 6×6 inside

For a ceiling lamp, the permissible uniformity level of 0.4 according to GOST 55710[2] in accordance with Figure 7 (red curve) is achieved for a room measuring 3.6×3.6 m. To increase the size of the illuminated room with acceptable uniformity, a variant with nine lamps arranged in the form of an orthogonal 3×3 matrix with a step of 4.4 m was used, and each matrix was square, containing 40×40 elements. The corresponding light distribution graph is shown in Figure 7 (green curve).

According to the graph in Figure 7 (green curve), the permissible level of uniformity is achieved for a square room measuring 12.18×12.18 m. At the same time, the distribution of illumination on the plane has a wave-like character. As an alternative, a variant of orthogonal arrangement of all LEDs in a room of 12.18×12.18 m, i. e. for a 120×120 matrix with a uniform pitch, was analyzed (Figure 7, blue curve). A comparison of the green and blue graphs in Figure 7 allows us to conclude about the advantage of the uniform arrangement of all LEDs in relation to the arrangement in the form of separate matrices.

The use of a large number of RGB LEDs requires significant power consumption for their power supply. Therefore, it is promising to use combined matrices consisting of RGB and more powerful white LEDs.

Conclusion

A methodology has been developed for calculating the illumination distribution on the plane when using LED matrices as a lighting source. Illumination is a function of the indicatrix of the light intensity of the LED, the number and location of LEDs in space. The results of modeling LED sources indicate the need to modernize simple orthogonal matrices containing the same type of elements with the same power mode for all elements, in order to increase the uniformity of illumination and efficiency. Such modernization can be carried out by changing the geometry of the matrices, differentiating the power modes of individual LEDs. The developed calculation program can be supplemented with options for introducing the changes listed above, as well as for analyzing the spectral distribution of radiation in space.

References

1. Münch M., Brondsted A.E., Brown S.A., Gjedde A., Kantermann T., Martiny K., Skene J.D., Wirz-Justice A., Mersch D. The Effect of Light on Humans. *Changing perspectives on daylight: Science, technology and culture. Sponsored supplement to Science/AAS*, 2017, pp. 16–23. Access mode: www.researchgate.net/publication/320838876. Access date: 19.01.2022.

2. Barroso A.M. (NL), Saudant R.M. (NL) Lighting system and method: patent RU2584674C2, IPC H05B37/02; applicant KONINKLEIKE PHILIPS ELECTRONICS NV (NL), application 01.05.2012, publ. 20.05. 2016 (in Russian).

3. Shen D. Collimator lenses Edison Opto. *Poluprovodnikovaya svetotekhnika* [Solid-state lighting], 2013, no. 1(21), pp. 20–21 (in Russian).

4. Vertli Y. Lenses with adjustable focus for LEDs. *Poluprovodnikovaya svetotekhnika* [Solid-state lighting], 2013, no. 1(21), pp. 22–23 (in Russian).

5. Trofimov P., Golikov O. Reflectors and hybrid lenses from Ledlink Optics. *Poluprovodnikovaya svetotekhnika* [Solid-state lighting], 2013, no. 1(21), pp. 24–25 (in Russian).

6. Da Silva H. Improvement of LED lamp designs using plastic optical silicones. *Poluprovodnikovaya svetotekhnika* [Solid-state lighting], 2013, no. 1(21), pp. 26–27 (in Russian).

7. Jian V., Schneider K. Improving the illumination of an object when using optics with full internal reflection. *Poluprovodnikovaya svetotekhnika* [Solid-state lighting], 2013, no. 1(21), pp. 28–30 (in Russian).

8. Barbosa J., Calixto W., L. da Cunha Brito. Secondary Lens Optimization for LED Lamps. *Journal of mechanics engineering and automation*, 2014, no. 4, pp. 46–51.

9. Sharakshane A. On the effectiveness of matte light diffusers. *Poluprovodnikovaya svetotekhnika* [Solid-state lighting], 2014, no. 1(27), pp. 8–11 (in Russian).

10. Valiev D.T., Rossomakhina N.E., Tyulkin E.V., Agapov N.A. Development of mathematical software for calculating and evaluating the image quality of an optical system. GraphiCon 2018: proceedings of the 28th International Conference on Computer Graphics and Machines-nom vision. Tomsk, September 24–27, 2018. National research Volume. polytech. un., pp. 418–421 (in Russian).

11. Kudaev S., Schreiber P. Optimizing LED illumination systems. *The International Society for Optical Engineering*. *Spie Newsroom*, 2006.
DOI: 10.1117/2.1200609.0353

12. Mandal P., Dey D., Roy B. Optimization of Luminaire Layout to Achieve a Visually Comfortable and Energy-Efficient Indoor General Lighting Scheme by Particle Swarm Optimization. *The Journal of the Illuminating Engineering Society of North America*, 2019, no. 17(1), pp. 1–16.
DOI: 10.1080/15502724.2018.1533853

13. Nikiforov S. “S-class” of semiconductor lighting engineering. *Komponenty i tekhnologii* [Components and technologies], 2009, no. 6, pp. 88–91 (in Russian).

Assessing of a Radiation Therapy Session's Duration at the Stage of Pre-Radiation Preparation

M.N. Piatkevich, E.V. Titovich

N.N. Alexandrov National Cancer Centre of Belarus,
Lesnoy 223040, Minsk District, Belarus

Received 30.11.2021
Accepted for publication 02.02.2022

Abstract

The treatment planning process includes a review of the radiation treatment plan which leads to a decision on the patient's treatment technique. The scope of this study was to create a mathematical model for calculating of a radiation therapy session duration during the pre-radiation planning stage.

For dosimetric planning of radiation treatment the authors provided a formula and an algorithm for determining of a patient's irradiation session duration. Radiation therapy session parameters such as radiation technique, number of monitor units, characteristics of radiotherapy equipment, number of radiation fields, radiation field parameters (angles of rotation of the radiotherapy coach, collimator, gantry), presence/absence of dose-modulating devices, dose rate, and duration of patient position verification procedures have all been taken into account during the development of software. The developed application explains how to define typical timing characteristics for various items as well as how to select a template from a built-in drop-down menu. If the dosimetric plan does not match for one of the templates, the program provides a space for defining of all parameters manually.

The anticipated deviations of the true indicators from the expected indicators of the duration of the radiation therapy session were assessed. A total of 300 cases have been completely measured, with 100 cases studied for each irradiation technique (IMRT, VMAT, 3D). The maximum detection confidence value for the 3DCRT irradiation technique is 2.3 %, while the deviation for the IMRT and VMAT irradiation techniques is less than 1 %. The magnitude and degree of the deviation of the measured value from the expected one for a variety of characteristics and features have been revealed to depend on the actions of the personnel.

The program developed allows medical physicists to analyze the timing parameters of the specified dosimetric planning methodologies directly on the treatment planning workstation. Evaluation of the duration of a radiation therapy session during the treatment planning stage, selection of various radiation treatment modalities, and consideration of the characteristics of the radiation session in each clinical case are available for analysis and further justified action.

Keywords: treatment session, linear accelerator, radiation therapy, timing.

DOI: 10.21122/2220-9506-2022-13-1-68-73

Адрес для переписки:
Петкевич М.Н.
РНПЦ онкологии и медицинской радиологии
имени Н.Н. Александрова,
агрогородок Лесной 223040, Минский район, Беларусь
e-mail: maxpetkevichn@gmail.com

Address for correspondence:
Piatkevich M.N.
N.N. Alexandrov National Cancer Centre of Belarus,
Lesnoy 223040, Minsk District, Belarus
e-mail: maxpetkevichn@gmail.com

Для цитирования:
M.N. Piatkevich, E.V. Titovich.
Assessing of a Radiation Therapy Session's Duration
at the Stage of Pre-Radiation Preparation.
Приборы и методы измерений.
2022. – Т. 13, № 1. – С. 68–73.
DOI: 10.21122/2220-9506-2022-13-1-68-73

For citation:
M.N. Piatkevich, E.V. Titovich.
Assessing of a Radiation Therapy Session's Duration
at the Stage of Pre-Radiation Preparation.
Devices and Methods of Measurements.
2022, vol. 13, no. 1, pp. 68–73.
DOI: 10.21122/2220-9506-2022-13-1-68-73

Оценка продолжительности сеанса лучевой терапии на этапе предлучевой подготовки

М.Н. Петкевич, Е.В. Титович

РНПЦ онкологии и медицинской радиологии имени Н.Н. Александрова,
агрогородок Лесной 223040, Минский район, Беларусь

Поступила 30.11.2021
Принята к печати 02.02.2022

Анализ плана лучевого лечения является неотъемлемой частью процесса предлучевой подготовки, в результате которого принимается решение о методике лечения пациента. Целью данной работы являлась разработка математической модели определения продолжительности сеанса лучевой терапии на этапе предлучевой подготовки.

Авторами предложены формула и алгоритм расчёта продолжительности сеанса облучения пациента на этапе дозиметрического планирования лучевого лечения. Разработано программное обеспечение расчёта продолжительности сеанса облучения, учитывающее значения всех параметров сеанса лучевой терапии: методику облучения, количество мониторных единиц, характеристики радиотерапевтического оборудования, количество радиационных полей, параметры полей облучения (углы поворота радиотерапевтического стола, коллиматора, штатива аппарата), наличие/отсутствие дозомодулирующих устройств, мощность дозы, продолжительность верификации положения пациента. В программе предусмотрена установка стандартных параметров плана облучения для различных локализаций и методик путём выбора конкретного шаблона из выпадающего списка. В случае, если дозиметрический план не соответствует ни одному из шаблонов, в программе предусмотрен ввод параметров плана вручную.

Произведена оценка отклонений, рассчитываемых разработанной программой значений продолжительности сеанса лучевой терапии от истинных значений. Измерения проведены для 300 случаев: исследованы по 100 случаев для каждой методики облучения (IMRT, VMAT, 3D). Максимальное выявленное отклонение рассчитанного значения от истинного составило 2,3 % для методики облучения 3DCRT, для методик облучения IMRT и VMAT отклонение составило менее 1 %. Выявлено, что с увеличением количества процедур, напрямую связанных с действиями персонала, увеличивается и величина отклонения рассчитанного значения с измеренным.

Разработанное программное обеспечение позволяет оценивать временные параметры выбранных подходов дозиметрического планирования на рабочем месте медицинского физика. Оценка длительности сеанса лучевой терапии на этапе предлучевой подготовки способствует выбору оптимальной методики лучевого лечения с учётом индивидуальных параметров сеанса облучения в каждом конкретном клиническом случае.

Ключевые слова: сеанс облучения, линейный ускоритель, лучевая терапия, временные характеристики.

DOI: 10.21122/2220-9506-2022-13-1-68-73

Адрес для переписки:
Петкевич М.Н.
РНПЦ онкологии и медицинской радиологии
имени Н.Н. Александрова,
агрогородок Лесной 223040, Минский район, Беларусь
e-mail: maxpetkevichn@gmail.com

Address for correspondence:
Piatkevich M.N.
N.N. Alexandrov National Cancer Centre of Belarus,
Lesnoy 223040, Minsk District, Belarus
e-mail: maxpetkevichn@gmail.com

Для цитирования:
M.N. Piatkevich, E.V. Titovich.
Assessing of a Radiation Therapy Session's Duration
at the Stage of Pre-Radiation Preparation.
Приборы и методы измерений.
2022. – Т. 13, № 1. – С. 68–73.
DOI: 10.21122/2220-9506-2022-13-1-68-73

For citation:
M.N. Piatkevich, E.V. Titovich.
Assessing of a Radiation Therapy Session's Duration
at the Stage of Pre-Radiation Preparation.
Devices and Methods of Measurements.
2022, vol. 13, no. 1, pp. 68–73.
DOI: 10.21122/2220-9506-2022-13-1-68-73

Introduction

Modern radiation therapy is not complete without the use of high-performance computing facilities [1, 2]. Thanks to the development of computer technology, modern dosimetric planning systems make it possible to model structures within an anatomical object, radiation targets and dose distributions, and to estimate their dose. Over the past decade, computer planning systems have been repeatedly improved by introducing of new components into their structure which make it possible to use a significant amount of input data at the stage of pre-radiation preparation of a patient in the generation of an irradiation plan [3]. Analysis of the radiation treatment plan is an integral part of the pre-radiation preparation process, on the basis of which a decision is made including of the patient's treatment method [4–7]. It is important to assess the parameters influencing the quality of the dosimetry plan since the safety and effectiveness of the medical care provided to the patient depends on it [8–9]. Nowadays the process of determining of a radiation therapy session duration at the stage of pre-radiation preparation is difficult [10]. The authors did not identify methods and approaches to determine of a radiation therapy session duration at the stage of evaluating of a radiation treatment plan, published in printed publications. It should be noted that the possibility of assessing of a radiation therapy session duration at the stage of pre-radiation preparation will make it possible to choose the optimal radiation therapy technique taking into account the individual parameters of the radiation session in each specific clinical case.

In this regard, the purpose of this work is to develop a mathematical model for determining of a radiation therapy session duration at the stage of pre-radiation preparation.

Mathematical model of irradiation session

In [11] the authors established the time characteristics of the radiation session components, which have a dominant influence on its duration and proposed an algorithm that allows determining the duration of radiation treatment of cancer patients depending on the use of different radiation therapy techniques and tumor localizations. In [12] the authors established the numerical values of dominant components of radiation therapy session for each of the most used in clinical practice of the Department of Radiation Therapy of N.N. Alexandrov National Cancer Centre of Belarus.

Based on the results obtained in [11] and [12], the components of a radiation therapy session that directly influence its duration are: laying the patient and centering in the position prescribed for irradiation, setting the required mechanical parameters of the gas pedal under visual control from the procedure room, setting/removing wedge filters, time spent on the process of preparation for irradiation generation, verification of the patient position, initializing the gas pedal with irradiation parameters, relevant.

Let us introduce the notation of time parameters for each of the procedures, which will be taken into account when determining the total time of the radiation therapy session:

T_{ses} – radiation therapy time;

t_{pl} – laying the patient and centering in the prescribed position for the irradiation;

t_{set} – setting the necessary mechanical parameters of the gas pedal under visual control from the procedure room;

t_{fil} – installation/removal of wedge filters;

t_{turn} – turning on the irradiation;

t_{ver} – patient position verification;

t_{init} – initialization of the gas pedal with irradiation parameters relevant to the second and subsequent treatment fields;

t_{tbl} – rotation of the therapeutic table;

t_{gan} – rotation of the tripod;

t_{coll} – rotation of the collimator;

t_{irr_f} – time of irradiation of one irradiation field;

t_{irr} – time of irradiation of the patient;

t_{fin} – patient out of the treatment room.

To describe a mathematical model of a radiation therapy session, the authors proposed the following formula (1):

$$\begin{aligned}T_{ses} = {} & t_{pl} + t_{set} + t_{fil} + t_{turn} + t_{ver} + t_{init\_1} + \\ & + t_{irr\_f1} + t_{fil\_2} + t_{turn\_2} + t_{init\_2} + \\ & + t_{tbl\_2} + t_{gan\_2} + t_{coll\_2} + t_{irr\_f2} + \dots + \\ & + t_{fil\_n} + t_{turn\_n} + t_{init\_n} + t_{tbl\_n} + \\ & + t_{gan\_n} + t_{coll\_n} + t_{irr\_fn} + t_{fin}.\end{aligned} \tag{1}$$

Using the proposed formula, it is possible to estimate the radiation therapy session time at the stage of dosimetric treatment planning.

Software

To estimate the duration of the irradiation session in accordance with the chosen approach of dosimetric planning at a medical physicist's workplace, a computer program was developed, the mathematical algorithm of which is based on the proposed formula (1). Figure 1 shows the interface of the program for calculating the duration of the irradiation session according to the three-dimensional conformal irradiation technique (3D CRT).

The program algorithm is shown in Figure 2.

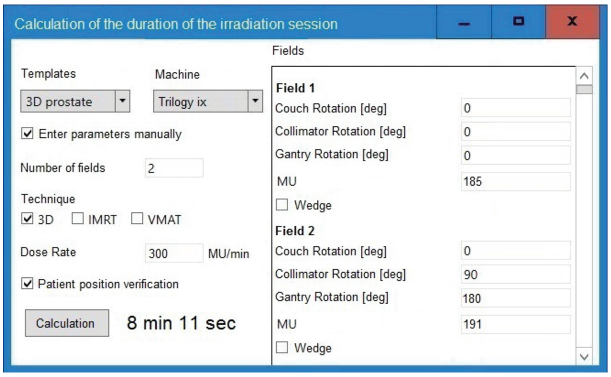

Calculation of the duration of the irradiation session

Templates: 3D prostate
Machine: Trilogy ix
☑ Enter parameters manually
Number of fields: 2
Technique: ☑ 3D ☐ IMRT ☐ VMAT
Dose Rate: 300 MU/min
☑ Patient position verification
Calculation
8 min 11 sec

Fields

Field 1
Couch Rotation [deg]: 0
Collimator Rotation [deg]: 0
Gantry Rotation [deg]: 0
MU: 185
☐ Wedge

Field 2
Couch Rotation [deg]: 0
Collimator Rotation [deg]: 90
Gantry Rotation [deg]: 180
MU: 191
☐ Wedge

Figure 1 – Interface of the computer program for calculating the duration of an illumination session

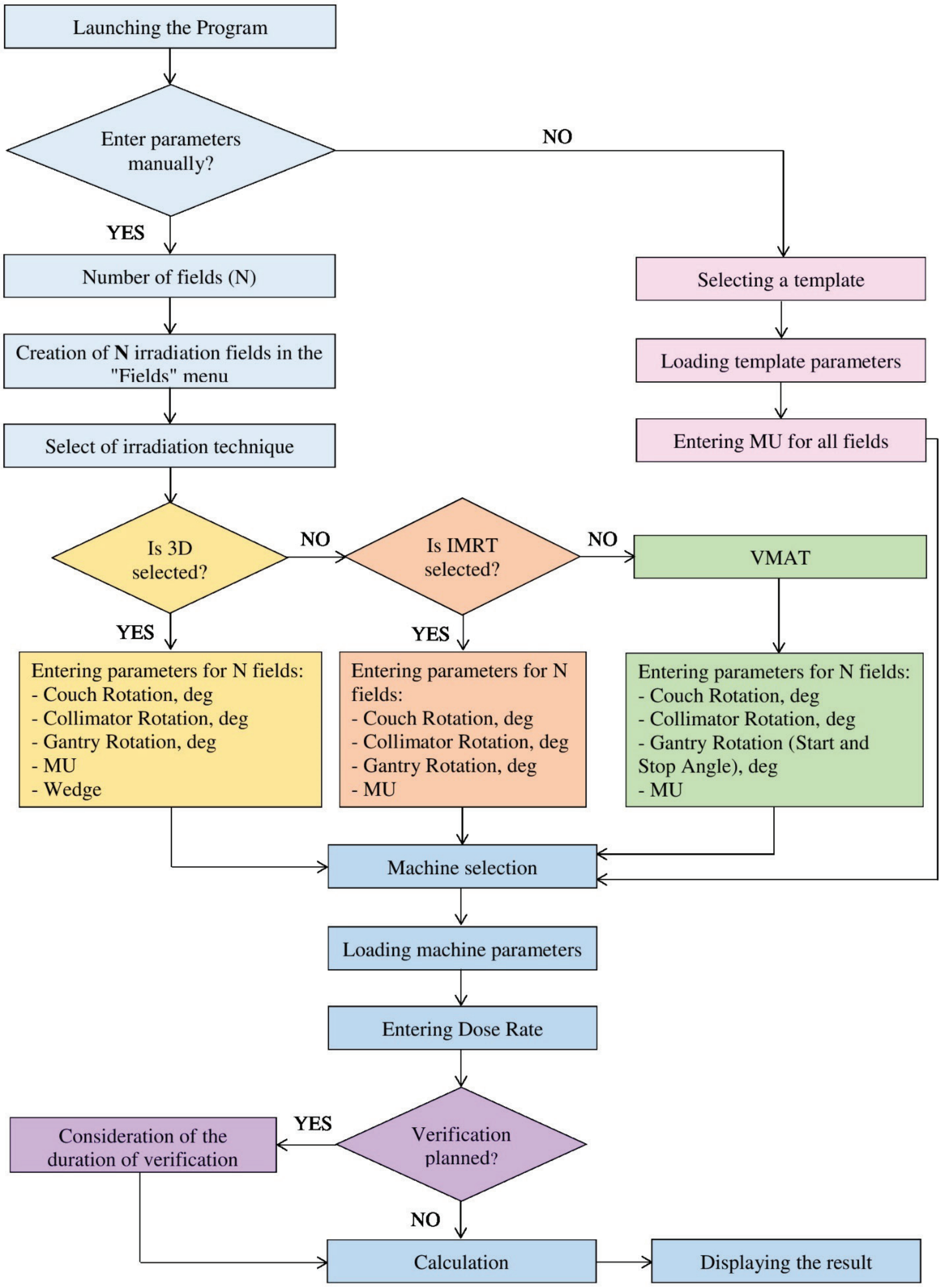

Figure 2 – Program algorithm

The computer program provides for setting standard parameters of the irradiation plan for different localizations and techniques by selecting a specific template from the drop-down list. After selecting a particular template, the parameters of the radiation treatment plan are automatically loaded, and then the number of monitor units for each radiation field must be entered. If the dosimetric plan does not correspond to any of the templates, the program provides the possibility to enter the plan parameters manually. In this case it is necessary to enter the required number of radiation fields in the area "Number of fields" and select the irradiation technique (3D, IMRT or VMAT), then enter the parameters of each field in the corresponding cell: table rotation angle, collimator rotation angle, tripod rotation angle, number of monitor units (MU) and presence of wedge-shaped filter if it is provided by the patient's radiotherapy plan. Then you select the model of the radiation therapy unit in the "Machine" menu, and then the necessary parameters of the selected unit are automatically loaded. Then in the "Dose Rate" area the dose rate is specified. In case of implementing a radiation treatment plan with patient position verification the checkbox "Patient position verification" is set. After setting all parameters of the radiation treatment plan, the duration of the radiation session "Calculate" is calculated, the result of the calculation is displayed in the corresponding cell.

Research results

The authors analyzed the data obtained by applying the developed software to determine the duration of the radiation session. The analysis was carried out by comparing the data obtained using the developed computer program with the true data measured in real time during the radiation therapy session. Measurements were made for 300 cases: 100 cases for each irradiation technique (IMRT, VMAT, 3D) were studied. Figure 3 shows a graph showing the effect of the duration of the radiation session on the deviation of the calculated values from the true values.

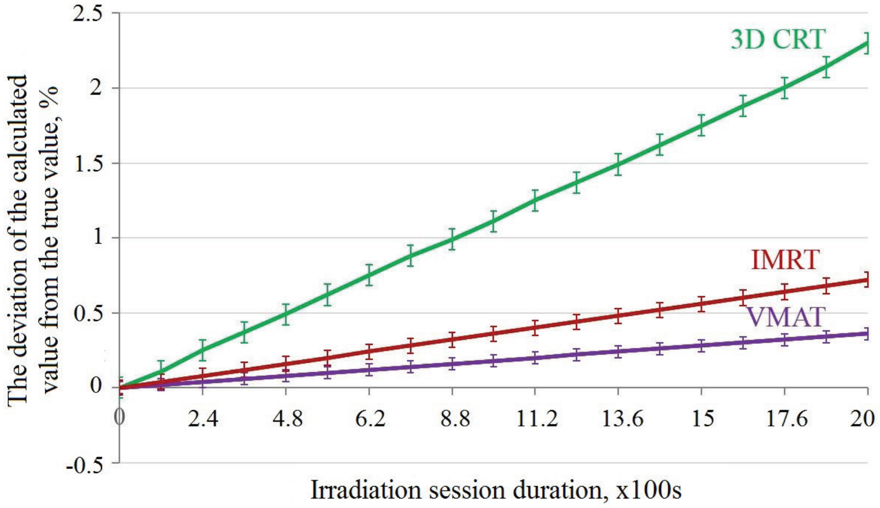

Figure 3 – Influence of irradiation session duration on the deviation of calculated values from true values for 3DCRT, IMRT and VMAT irradiation techniques

The maximum detected deviation of the calculated value from the true value was 2.3 % for the 3DCRT irradiation technique; for the IMRT and VMAT irradiation techniques the deviation was less than 1 %. The average deviation was 1.3 % for the 3DCRT technique and 0.4 % for IMRT and VMAT. It was found that with an increase in the number of procedures directly related to the actions of the personnel, the deviation of the calculated value from the measured one also increases. This is due to the different physical characteristics of the person involved in the implementation of the radiation therapy session.

Conclusion

The authors have proposed a formula for calculating the time of an irradiation session of patients at the stage of dosimetric planning of radiation treatment. Using this formula makes it possible to take into account the time spent on procedures that make up a radiation therapy session, and thus minimize the probability of an error in the planned dose delivery related to the mobility of internal organs and biological processes of the irradiated biological object. Application of the approach focused on reducing the time cost of the radiation therapy session will also increase the throughput of radiotherapy equipment and in some cases reduce its wear and tear.

An algorithm for calculating the duration of a radiotherapy session is proposed. Software is developed which allows to estimate the time parameters of the selected dosimetric planning approaches at the medical physicist's workplace.

Deviations of the calculated values of radiation therapy session duration by means of the developed program from the actual values were evaluated. The maximum deviation of the calculated value from the true value is 2.3 % for 3DCRT technique, for IMRT and VMAT techniques the deviation was less than 1 %. The average deviation for the 3DCRT technique was 1.3 %, and for the IMRT and VMAT techniques was 0.4 %.

References

1. Chernayev A.P., Lykova E.N., Popodko A.I. *Medecynskoe oborudovanie v sovremennoi luchevoi terapii* [Medical equipment in modern radiation therapy]. Moscow, *OOP fizicheskogo fakulteta MGU*, 2019, 101 p.

2. Selecting Megavoltage Treatment Technologies in External Beam Radiotherapy. *International Atomic Energy Agency*, ISSN 2074-7667, 2022, no. 17, 43 p.

3. Khan F.M. The physics of radiation therapy, 4th ed. Philadelphia, Lippincott Williams & Wilkins, 2010, 531 p.

4. Trufanov G.E. *Luchevaay terapia. Tom 2* [Radiation therapy, part 2]. Moscow, GEOTAR-Media, 2010, 192 p.

5. Fotina I.E. *Osnovy luchevoi terapii. Distantsionnaya radioterapiya* [Fundamentals of Radiation Therapy. External beam therapy]. Tomsk, Izdatelstvo Tomskogo politekhnicheskogo universiteta, 2010, 104 p.

6. Tepper Joel E., Foote Robert L., Michalski Jeff M. [Clinical radiation oncology. Fifth edition]. Elsevier Philadelphia, PA, 2021, 1586 p.

7. Ovchinikov V.A., Uglyanitsa K.N., Volkov V.N. *Sovremennye metody luchevogo lecheniya onkologicheskikh bolnykh* [Modern radiation treatment methods for cancer patients]. *Zhurnal GrSMU* [Journal of Grodno State Medical University], 2010, no. 1, pp. 93–97 (in Russian).

8. Xia Ping, Godley Andrew (eds.) Strategies for radiation therapy treatment planning. *Demos Medical Publishing*, 2019, 319 p.

9. Khan F.M., Gibbons J.P. Khan's the physics of radiation therapy, 5th ed. Philadelphia, Wolters Kluwer, 2014, 584 p.

10. Lykova E.N. Uzarova K.A. *Vvedenie v planirovanie luchevoi terapii puchkami tormoznykh fotonov* [Introduction to Beam Radiation Therapy Planning bremsstrahlung photons]. Moscow, *OOP fizicheskogo fakulteta MGU*, 2019, 108 p.

11. Titovich E.V., Patsiapalau P.A., Piatkevich M.N., Kiselev M.G. [The algorithm for determining timing of radiotherapy session components for different methods of oncology patients irradiation at the stage of radiotherapy planning]. *Pribory i metody izmerenii* [Devices and Methods of Measurements], 2017, vol. 8, no. 1, pp. 73–80 (in Russian).
DOI: 10.21122/2220-9506-2017-8-1-73-80

12. Titovich E.V, Piatkevich M.N., Makarava N.I. [Methodology of defining of the radiation therapy components for various methods of patients' treatingusing medical linear accelerators and gamma-therapeutic devices]. *Pribory i metody izmerenii* [Devices and Methods of Measurements], 2020, vol. 11, no. 4, pp. 289–287.
DOI: 10.21122/2220-9506-2020-11-4-289-287

ПРАВИЛА ОФОРМЛЕНИЯ СТАТЕЙ

Статьи, направленные в редакцию журнала, должны удовлетворять требованиям «Инструкции о порядке оформления квалификационной научной работы (диссертации)…», утвержденной Постановлением ВАК РБ от 28.02.2014 г. № 3

1. Материал статьи должен соответствовать профилю журнала и излагаться предельно ясно.

2. Статья представляется на русском или английском языке и публикуется на языке представления.

3. Поступившие в редакцию статьи проходят двойное полуслепое рецензирование. Основные критерии целесообразности опубликования – актуальность тематики, информативность, научная новизна.

4. Статья представляется в распечатанном и в электронном виде в формате текстового редактора Word for Windows, набор – сплошным текстом (без деления на колонки). Объём статьи не должен превышать 14 страниц, включая текст (шрифт Times New Roman, размер 12 п., интервал 1,5), таблицы, графический материал, всю необходимую информацию на английском языке.

5. На первой странице статьи указываются: название статьи, фамилии авторов (фамилия автора, с которым следует вести переписку, отмечается звёздочкой и указывается его адрес электронной почты), названия и почтовые адреса организаций (улица, номер дома, индекс, город, страна), в которых работают авторы, на русском и английском языках. Статья включает: аннотацию (в пределах 200–250 слов); ключевые слова (не более 5); введение, в котором делается краткий обзор сделанного в мире и конкретно формулируется цель работы; основную часть; заключение, в котором в сжатом виде сформулированы основные полученные результаты с указанием их новизны, преимуществ и возможностей применения; список использованных источников. Аннотация, ключевые слова, список использованных источников представляются на русском и английском языках.

6. Аннотация должна быть информативной (содержать «выжимку» из всех разделов статьи – введения с указанием цели работы, методики, основной части и заключения).

7. Графический материал должен быть контрастным и чётким. Необходимо придерживаться единообразия техники исполнения однотипных иллюстраций. Рисунок должен располагаться после абзаца, содержащего ссылку на него. Не допускается размещение рисунков в конце подраздела и статьи. Изобразительный материал вставляется в текст статьи, а также даётся в виде отдельных файлов **(формат tif, jpg, разрешение не менее 300 dpi)**. Текст на рисунках набирается основной гарнитурой; размер кегля соизмерим с размером рисунка (желательно 8 пунктов). Все рисунки нумеруются и сопровождаются подрисуночными подписями. Фрагменты рисунка обозначаются строчными курсивными латинскими буквами – «*a*», «*b*» и т. д. Надписи на рисунках и подписи к рисункам даются на русском и английском языках. Все сокращения и обозначения должны быть расшифрованы в подрисуночной подписи. Рисунки желательно предоставлять в цвете. На рисунках должны быть указаны оси с обозначением приводимых величин и масштабов. На графиках не нужно давать координатную сетку, если это не осциллограмма. Во всех случаях на рисунках должен быть приведён масштаб.

8. У графиков, имеющих числовые значения по осям, рамки должны быть открыты, а засечки направлены внутрь рамки. На рисунках, представляющих собой графики зависимостей, не следует делать размерную сетку, следует дать лишь засечки на осях, причем все засечки должны быть оцифрованы. Если оси на рисунках оцифрованы, то они завершаются на позиции очередной засечки, где засечка не ставится, а вместо числовых значений даются обозначения переменной и единица измерения. Если оси не оцифровываются, то они завершаются стрелками, рядом с которыми даются обозначения переменных без единиц измерения.

9. Полутоновые фотографии приборов или их частей представляются при публикации в тех случаях, когда они несут существенную информацию, которую нельзя выразить иным способом. Фотографии должны быть высококачественными, контрастными, с хорошо различимыми деталями.

10. Иллюстрации (графики, диаграммы, схемы, чертежи), рисованные средствами MS Office, должны быть контрастными и чёткими. Недопустимо нанесение средствами MS Word каких-либо элементов поверх вставленного в файл рукописи рисунка (стрелки, подписи) ввиду большого риска их потери на этапах редактирования и вёрстки. Иллюстрации должны иметь размеры, соответствующие их информативности: 8–8,5 см (на одну колонку), 17–17,5 см (на две колонки) или 23 см (во весь лист). Поэтому желательно изображать отдельные элементы и надписи на рисунке так, чтобы при уменьшении масштаба рисунка до одного из указанных размеров буквы и цифры приобрели высоту 2–2,5 мм, элементы схем 3–5 мм, отдельные точки 1 мм, а линии должны быть при этом разнесены на расстояние не менее 0,5–1 мм.

11. Надписи и обозначения на иллюстрациях следует располагать так, чтобы они не соприкасались ни с какими её частями. На задний план иллюстрации желательно не добавлять серый (цветной) фон или сетки.

12. Таблицы не должны дублировать графики. Каждая таблица имеет заголовок. На все таблицы

и рисунки следует давать ссылки в тексте. Таблицы не должны содержать вертикальные линии, делящие таблицу на столбцы. Название и содержание таблиц представляется на русском и английском языках.

13. Обозначения и сокращения, принятые в статье, расшифровываются непосредственно в тексте.

14. Размерность всех величин, принятых в статье, должна соответствовать Международной системе единиц измерений (СИ).

15. Набор формул должен проводиться в редакторе MathType целиком. Набор формул из составных элементов не допускается, номера формул – по правому краю. Нумеруются лишь формулы, на которые есть ссылки в тексте.

16. Необходимо использовать следующие установки редактора формул. Размеры: полный – 10 пт, подстрочный – 9 пт, под-подстрочный – 7 пт, символ – 14,5 пт, подсимвол – 12,5 пт. Стили: текст, функция, число, кириллица – шрифт «Times New Roman», вектор-матрица – шрифт «Times New Roman», жирный; греческий малый, греческй большой, символ – шрифт «Symbol», прямой; переменная – шрифт «Times New Roman», курсив.

17. Отдельные строчные буквы и специальные символы набираются в тексте гарнитурой Symbol **без использования редактора формул**. При наборе формул и буквенных обозначений необходимо учитывать следующие правила: **русский алфавит не используется**; греческие буквы, математические символы (grad, div, ln, min, max и др.), единицы измерения (Вт, Дж, В, кг и др.), кириллические буквы, сокращения от русских слов ($q_{\text{ср}}$); обозначения химических элементов и соединений (в т. ч. в индексе) набираются **прямо**; латинские буквы – переменные и символы физических величин (в т. ч. в индексе) набираются **курсивом**; векторы – жирным шрифтом (стрелки вверху не ставятся).

18. Начертание обозначений в формулах и в основном тексте должно быть полностью идентично. В расшифровке формул, которая начинается словом «где», символы и их порядок должны соответствовать символам и их порядку следования в формулах.

19. Список использованных источников составляется в порядке упоминания ссылок по тексту, должен содержать полные библиографические данные и приводится в конце статьи. Не рекомендуется давать ссылки на материалы конференций, статьи из электронных журналов без идентификатора **DOI**, учебные пособия, интернет-ресурсы. Ссылки на неопубликованные работы не допускаются. Желательно, чтобы количество ссылок было не менее 10; самоцитирование – не более 20 %.

20. Авторы на отдельной странице предоставляют о себе следующие сведения: фамилия, имя, отчество, ученая степень и звание, место работы и занимаемая должность, адрес электронной связи.

21. Статьи, излагающие результаты исследований, выполненных в учреждениях, должны иметь соответствующее разрешение на опубликование в открытой печати.

22. При необходимости в конце основного текста указываются наименование фонда, оказавшего финансовую поддержку, или уровень и наименование программы, в рамках которой выполнена работа, на русском и английском языках.

23. Авторы несут ответственность за направление в редакцию статей, ранее уже опубликованных или принятых к печати другими изданиями.

24. Статьи, не соответствующие перечисленным требованиям, к рассмотрению не принимаются и возвращаются авторам. Датой поступления считается день получения редакцией первоначального варианта текста.

25. Редакция предоставляет возможность первоочередного опубликования статей лицам, осуществляющим послевузовское обучение (аспирантура, докторантура, соискательство), в год завершения обучения; не взимает плату с авторов за опубликование научных статей; оставляет за собой право производить редакторские правки, не искажающие основное содержание статьи.

AUTHOR GUIDELINES

1. Article materials should correspond to the journal profile and be clearly written.

2. An article should be submitted in Russian or English and will be published in its original language.

3. Articles received by the Editorial Board will be reviewed by 2 specialists. The main criteria of acceptance are theme actuality, information value, and scientific novelty.

4. All materials should be submitted in two hard copies together with electronic file in the Word for Windows format (97/2000/2003). The paper should not exceed 14 pages of the typewritten text (Times New Roman, 12 points, 1.5-space).

5. The article should contain UDC number, Title (printed in capitals), Authors' names (the corresponding author name should be marked with asterisk), full Address of organization(s) in which the author(s) work, Abstract (200–250 words), Keywords (not more than 5 words), Introduction, the Text of the paper with tables, diagrams and figures (if there are any), Conclusion with clearly stated inferences, List of References, List of Symbols and Abbreviations (if it is necessary). Title, Authors' names and affiliation(s), Abstract, Keywords should be presented both in English and Russian languages.

6. The abstract should be informative (contain "squeeze" from all sections of the article – the introduction stating the purpose of the work, methods, main part and conclusion).

7. Figures should be black-and-white, represented in graphical formats tif, attached with Excel or MS Graph and added with captions. All symbols in figures should be descripted.

8. Tables should be placed directly in the article body. Diagrams and tables should not contain the same information. Each table should have the title. All tables, diagrams and figures should be referenced in the text.

9. Symbols and abbreviations which are used in articles should be deciphered directly in the text and also (if necessary) taken out on a separate page.

10. Dimensions of all quantities used in the article should correspond to International System of Units.

11. Formulas should be taped in MathType.

12. List of References is to be placed at the end of the article with full bibliographic information. Order of references should correspond to the order of their occurrence in the text. It is not recommended to refer to conference proceedings, papers from electronic journals without **DOI** number, textbooks, internet resources. References on unpublished works are prohibited. It is recommended to refer to not less than 10 references, self-citations – not more than 20 %.

13. The following information about every co-author should be presented: family name, first name, patronymic (or second) name (if there are any), scientific degree and title, organization and position, full address with the postal code for correspondence, office or mobile phone numbers, fax, e-mail.

14. Articles containing investigation results obtained in organizations should have a corresponding permission for publication.

15. Names of Foundations or Programs financially granted the research may be acknowledged in the end of the text.

16. Authors are responsible for submitting articles previously published or accepted by other publisher.

17. Articles not meeting the requirements of the Editorial Board would not be accepted and may be returned to the authors. The date of receipt is considered to be the day when the Editorial Board receives the author's original paper.

18. Authors conducting postgraduate (graduate studies, doctoral studies) have a priority in publishing their articles out of queue in the year of completion. Authors do not pay for publishing scientific articles. The Editorial Board can shorten and/or change the text if it does not strain the meaning of the article.

Индексы:
74835; 748352